

Three-dimensional modeling of charge transport, injection and recombination in organic light-emitting diodes

Citation for published version (APA):

Holst, van der, J. J. M. (2010). *Three-dimensional modeling of charge transport, injection and recombination in organic light-emitting diodes*. [Phd Thesis 1 (Research TU/e / Graduation TU/e), Applied Physics and Science Education]. Technische Universiteit Eindhoven. <https://doi.org/10.6100/IR692268>

DOI:

[10.6100/IR692268](https://doi.org/10.6100/IR692268)

Document status and date:

Published: 01/01/2010

Document Version:

Publisher's PDF, also known as Version of Record (includes final page, issue and volume numbers)

Please check the document version of this publication:

- A submitted manuscript is the version of the article upon submission and before peer-review. There can be important differences between the submitted version and the official published version of record. People interested in the research are advised to contact the author for the final version of the publication, or visit the DOI to the publisher's website.
- The final author version and the galley proof are versions of the publication after peer review.
- The final published version features the final layout of the paper including the volume, issue and page numbers.

[Link to publication](#)

General rights

Copyright and moral rights for the publications made accessible in the public portal are retained by the authors and/or other copyright owners and it is a condition of accessing publications that users recognise and abide by the legal requirements associated with these rights.

- Users may download and print one copy of any publication from the public portal for the purpose of private study or research.
- You may not further distribute the material or use it for any profit-making activity or commercial gain
- You may freely distribute the URL identifying the publication in the public portal.

If the publication is distributed under the terms of Article 25fa of the Dutch Copyright Act, indicated by the "Taverne" license above, please follow below link for the End User Agreement:

www.tue.nl/taverne

Take down policy

If you believe that this document breaches copyright please contact us at:

openaccess@tue.nl

providing details and we will investigate your claim.

Three-dimensional modeling of charge transport, injection and recombination in organic light-emitting diodes

PROEFSCHRIFT

ter verkrijging van de graad van doctor aan de Technische Universiteit Eindhoven, op gezag van de rector magnificus, prof.dr.ir. C.J. van Duijn, voor een commissie aangewezen door het College voor Promoties in het openbaar te verdedigen op dinsdag 21 december 2010 om 16.00 uur

door

Jeroen Johannes Maria van der Holst

geboren te Hoorn

Dit proefschrift is goedgekeurd door de promotoren:

prof.dr. M.A.J. Michels

en

prof.dr. R. Coehoorn

Copromotor:

dr. P.A. Bobbert

A catalogue record is available from the Eindhoven University of Technology Library

ISBN: 978-90-386-2388-7

Druk: Universiteitsdrukkerij Technische Universiteit Eindhoven

Omslagontwerp: Verspaget & Bruinink

nano  **ned**

This research was supported by Nanoned, a national nanotechnology program coordinated by the Dutch Ministry of Economic Affairs

Flagship: Nano Electronic Materials

Project Number: EAF.6995

Contents

1	Organic electronics, a general introduction	1
1.1	Organic electronics	3
1.2	Organic light-emitting diodes	4
1.3	Conduction in organic materials	6
1.4	Energetic disorder	7
1.5	Hopping transport	8
1.6	Models for charge transport in bulk systems	10
1.7	Percolation and the three-dimensional structure of charge transport	12
1.8	Recombination	13
1.9	From three-dimensional modeling calculations and simulations to a predictive OLED model	14
1.10	Scope of this thesis	16
	References	18
2	Computational methods for device calculations	21
2.1	Master-Equation approach	22
2.2	Solving the steady-state master equation for a homogeneous bulk system	23
2.3	Kinetic Monte-Carlo approach	25
2.4	Kinetic Monte-Carlo scheme for a homogeneous bulk system	26
	References	30
3	Monte-Carlo study of the charge-carrier mobility in disordered semiconducting organic materials	33
3.1	Introduction	34
3.2	Monte-Carlo method	35
3.3	Influence of Coulomb interactions on mobility	36
3.4	Discussion	37
3.5	Summary and conclusions	39
	References	40
4	Modeling and analysis of the three-dimensional current density in sandwich-type single-carrier devices of disordered organic semiconductors	43
4.1	Introduction	45

4.2	Theory and methods	47
4.2.1	Three-dimensional Master-Equation model	47
4.2.2	One-dimensional continuum model	50
4.3	Results	51
4.4	Three-dimensional structure of the current distribution; consequences for different models	55
4.5	Summary and conclusions	63
	References	64
5	Monte-Carlo study of charge transport in organic sandwich-type single- carrier devices: effects of Coulomb interactions	67
5.1	Introduction	69
5.2	Theory and methods	72
5.2.1	Monte-Carlo method	72
5.2.2	One-dimensional continuum drift-diffusion model	76
5.3	Results for current-voltage characteristics	78
5.4	Effects of short-range Coulomb interactions on the three-dimensional current distributions	83
5.5	Summary and conclusions	86
	References	88
6	Electron-hole recombination in disordered organic semiconductors: va- lidity of the Langevin formula	91
6.1	Introduction	92
6.2	Monte-Carlo method	95
6.3	Results	99
6.4	Discussion and conclusions	105
	References	107
7	Relaxation of charge carriers in organic semiconductors	111
7.1	Introduction	112
7.2	Monte-Carlo method	113
7.3	Relaxation of the mobility	115
7.4	Conclusion and outlook	119
	References	120
8	Conclusions and outlook	121
	Summary	125
	Dankwoord	129
	List of publications	131

Chapter 1

Organic electronics, a general introduction

ABSTRACT

Organic light-emitting diodes (OLEDs) are promising high-efficiency lighting sources that are presently being introduced in a wide variety of applications. These devices work as follows. Electrons and holes are injected in a stack of layers of organic molecular or polymeric semiconducting materials, in which they are transported under the influence of an applied bias voltage and their mutual Coulombic interactions either to the collecting electrode or to each other. When electrons and holes meet, they recombine to form a bound electron-hole pair (exciton) which can decay radiatively under the emission of a photon. Due to the amorphous nature of the organic materials used, charge carriers are transported by means of hopping between neighboring molecules or segments of a polymer. The energy levels of the hopping "sites" are often assumed to be randomly distributed according to a Gaussian density of states (DOS). In the last two decades the theoretical understanding of the transport of charge carriers through this disordered energetic landscape of sites has grown substantially. The further development of a predictive model describing all important electronic processes in OLEDs, like, in addition to charge-carrier transport, the injection of charge carriers, the recombination of electrons and holes, the formation and motion of excitons and the luminescent decay of excitons, is of profound importance to enhance the efficiency and lifetime of OLEDs.

In this chapter, certain aspects of OLEDs are introduced. First, an overview of organic electronics in general and specifically OLEDs is given. Afterwards, the effects of disorder on the charge-carrier transport and recombination in organic

semiconductors are discussed. This chapter ends with a presentation of the overview of the contents of this thesis.

1.1 Organic electronics

It is often thought that all organic materials are electrically insulating. However, the first organic material with conductive properties, polyaniline, was already found in the second half of the 19th century.¹⁻³ During the 1950s and 1960s, the study of conduction in polymers intensified and in 1963 for the first time conductivities were found comparable with those in inorganic materials, viz. in the polymer polypyrrole.⁴⁻⁶ In 1974 the first actual organic device, a voltage-controlled switch, was built with the polymer melanin.⁷ Since the 1970s, layers of organic photoconductors were used in xerographic devices, like printers, replacing inorganic selenium and silicon layers.⁸ The area of organic electronics got a huge boost in 1977 by the work of A.J. Heeger, A.G. MacDiarmid, and H. Shirakawa,⁹ who discovered that the conductivity of polyacetylene after doping with iodine increases by seven orders in magnitude. For this and following work, and in general, as in the words of the Nobel committee, *for the discovery and development of electrically conductive polymers*, they obtained the Nobel prize in chemistry in 2000.¹⁰ Soon after their discovery other conductive organic materials were found and the research field of organic electronics matured over the years from a proof-of-principle phase into a major interdisciplinary research area, involving physics, chemistry and other disciplines.

Organic materials have many benefits over inorganic materials:

- It is possible to process polymers from a solution via spin-coating or ink-jet printing, whereas for the processing of inorganic materials expensive processing setups are needed like high-vacuum clean chambers. As a result it becomes very easy to deposit polymers over large areas and on top of different types of substrates, including thin flexible substrates.
- Most conductive organic materials are relatively cheap to synthesize. Often, the substrate on which the organic material is deposited is the cost-limiting factor.
- Organic materials are chemically tunable. For example, to change the color emitted by an OLED, the organic material that causes the photon emission can be chemically modified.

There are numerous electronic applications for organic materials. They are nowadays used in a wide variety of devices like organic light-emitting diodes (OLEDs),¹¹ organic field-effect transistors (OFETs)¹² and organic photovoltaic cells (OPCs).¹³ Examples of devices containing OFETs are electronic paper, smart windows and cheap radio-frequency identification (RFID) tags. Some of these devices are already commercially successful on the market.



Figure 1.1: A prototype OLED TV. Source: Philips.

1.2 Organic light-emitting diodes

In 1950 it was observed by Bernanose *et al.* for the first time that organic materials can show electroluminescence.^{14–17} Specifically, the organic material used was the small-molecule dye acridine orange. The authors attributed the electroluminescence to the direct excitation of the dye molecules. Partridge observed in the 1980s that electroluminescence could also take place in polymers.^{18–21} Tang and van Slyke built the first bi-layer organic diode, consisting of separate electron and hole transporting layers.²² As a result, *radiative recombination*, the process in which electrons and holes meet and annihilate each other under the emission of a photon, took place in the middle of the device. In 1990, Burroughes *et al.* developed the first high-efficiency green-emitting OLED, based on a poly(*p*-phenylene vinylene) derivative.¹¹

A basic OLED consists of a single layer of organic material sandwiched between two electrodes. Electrons are injected at the electron-injecting electrode (cathode) and collected at the electron-collecting electrode (anode). A hole can be conceived of as a lacuna, missing an electron, and is therefore positively charged. In general, holes are injected at the anode and collected at the cathode. Both electrons and holes generally have to overcome an energetic barrier when they are injected. This energetic barrier, which we call *injection*

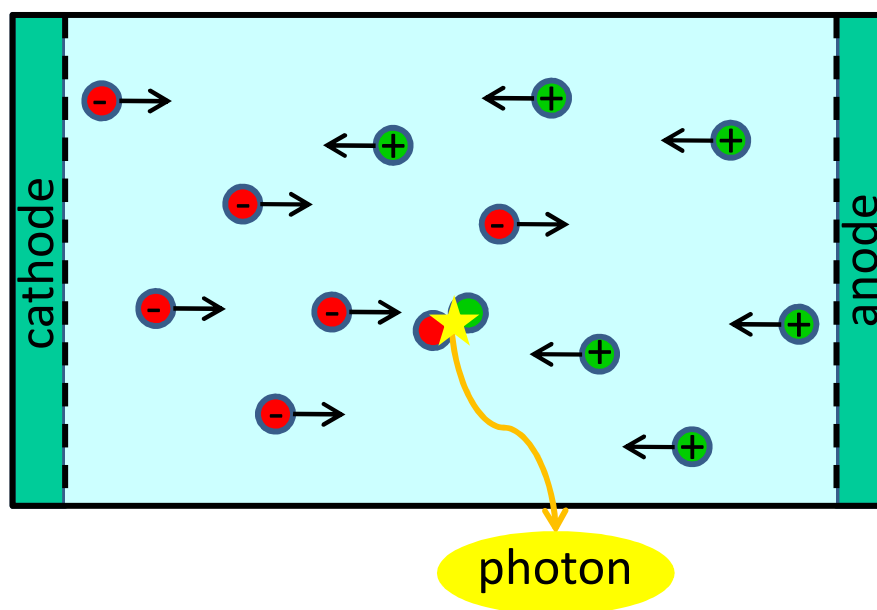


Figure 1.2: Working principle of a single-layer OLED. Electrons (denoted by red circles with a minus sign) are injected at the cathode. Holes (denoted by green circles with a plus sign) are injected at the anode. Both electrons and holes move to the opposite electrodes. Whenever an electron and a hole meet, they recombine and a photon can be emitted.

barrier, is the result of a misalignment between the Fermi level of the electrode and the energy level at which electrons or holes are injected into the organic material. Under the influence of the driving potential applied over the device, the electrons are transported to the anode and the holes to the cathode. When the electrons and holes meet each other, recombination takes place and light is emitted. Often, a transparent material, for example indium tin oxide (ITO), is chosen for one of the electrodes, such that the light can leave the device.

Nowadays, OLEDs consist of multiple layers of organic compounds, each with its own function. There are layers functioning as electron/hole transporting layers, electron/hole blocking layers, electron/hole injection layers, and emission layers. With these layers the transport of charges and the precise location of the recombination processes can be regulated. By adding specific dye molecules to the emission layers the frequency of the emitted light can be optimized to the value that is needed. By combining several emission layers with dye molecules it is even possible to manufacture an OLED that can emit white light.

OLEDs have the potential to become commercially successful, but improvement of their efficiency and stability is still needed. Compared to inorganic LEDs, OLEDs still have a shorter *lifetime*. The operational lifetime of a device is often defined as the total time that a device can be used before the intensity of the emitted light has dropped by 50%. The state-

of-the-art white OLEDs nowadays have a lifetime of around 10,000 hours, which is around 8 years if operated at 3 hours per day. OLEDs also still have a lower *luminous efficacy* as compared to state-of-the-art inorganic devices. State-of-the-art white OLEDs have been made in laboratories that have a luminous efficacy of 100 lm/W, a value that is six times as large as incandescent lighting devices. On the other hand, state-of-the-art inorganic LEDs exist that have a (laboratory) luminous efficacy of around 200 lm/W. Increasing the efficiency of OLEDs is important for two reasons. Obviously, less electrical power is used. However, when the device needs less electrical power, it is also less electrically stressed, which in turn is beneficial for the lifetime of the device.

1.3 Conduction in organic materials

We usually distinguish two groups of organic materials, polymers and small-molecule materials. Polymers are chain-like molecules with a long carbon backbone. This carbon backbone can be either linear or branched. Apart from hydrogen atoms, different (functional) side groups can be attached to each individual carbon atom of this backbone. Small-molecule materials are materials consisting of molecules with a much lower molecular weight than polymers. Examples are small oligomers, like pentacene, which are bound by van der Waals bonds, and organometallic complexes, which are ionically bonded. These molecules have the tendency to stack in a more ordered fashion than polymers.

Most conductive organic materials are conjugated. In general, this means that alternating single and double carbon bonds are present. In non-conjugated materials, like polyethylene, all four electrons in the outer shell of the carbon atoms occupy hybridized sp^3 -orbitals, leading to a strong σ -bonding between the carbon atoms. In conjugated materials, only three electrons in the outer shell of the carbon atoms occupy hybridized sp^2 -orbitals in the plane of the backbone and contribute to the single σ -bonding of the carbon atoms. The fourth electron is located in a p_z -orbital pointing out of the plane of the backbone. The p_z -orbitals of neighboring carbon atoms overlap with each other and form a π -bond, which is weaker than the σ -bonds. The combination of a σ - and π -bond leads to a double carbon bond. The electrons belonging to π -orbitals formed by the overlapping p_z -orbitals are delocalized over the whole conjugated part of the molecule. The formation of a system of π -bonds via the overlap of p_z -orbitals is called π -conjugation. Molecules with an alternating series of primarily single and double carbon bonds in the carbon backbone are not the only molecules in which conjugation occurs. π -conjugation can also occur with interruption of the carbon backbone by a single nitrogen or sulfur atom.

The total set of occupied molecular π -orbitals can be compared to the states in the valence band of inorganic materials, while the set of unoccupied molecular π orbitals, or π^* -orbitals, can be compared to states in the conduction band of inorganic materials. The occupied molecular orbital with the highest energy is called the Highest Occupied Molecular Orbital (HOMO), whereas the unoccupied molecular orbital with the lowest energy is called the

Lowest Unoccupied Molecular Orbital (LUMO). The band gap between the HOMO and LUMO energy is typically a few eV large, which explains the semiconducting nature of the organic material.

On a microscopic scale a thin film of a conjugated organic material often looks amorphous. The material can be disordered due to the irregular packing of the molecules. Polymers have twists, kinks, and defects. Moreover, the functional side groups that are attached to the carbon backbone can vibrate and rotate over time. All these effects lead to the split-up of the π -conjugated system of overlapping p_z -orbitals into separate electronic states localized at specific *sites*, extending over a few molecular units. Transport of charges takes place via a hopping process in between those sites. This process will be explained in the following two sections.

1.4 Energetic disorder

We call the HOMO and LUMO energies *electron* and *hole site energies*, respectively. Different sites in conjugated organic materials have different electron and hole site energies depending on the inter- and intra-molecular interactions. This implies an *energetic disorder*. The randomness in the positions of the sites leads to a so-called *positional disorder*. The distribution of site energies is called a *density of states* (DOS). Often, the DOS, $g(E)$, in organic materials is assumed to be Gaussian:

$$g(E) = \frac{N_t}{\sqrt{2\pi}\sigma} \exp\left[-\frac{E^2}{2\sigma^2}\right], \quad (1.1)$$

with E the site energy, σ the standard deviation of the DOS, and N_t the density of sites. In the case of small molecule materials the assumption of a Gaussian distribution can be justified with the Central Limit Theorem, which states that the addition of many random numbers leads to a Gaussian distribution. For polymers, the experimentally obtained distribution in general does not have to be Gaussian. For example, Blom *et al.* successfully modeled the hole mobility in a poly(*p*-phenylenevinylene) (PPV) device by assuming an exponential DOS and the electron mobility in the same material by assuming a Gaussian DOS plus a smaller extra exponential DOS.²³ The precise form of the DOS is still a major point of uncertainty in the modeling of the mobility. In this thesis we always assume the DOS to be Gaussian. Typically, the standard deviation σ , which we call *disorder strength*, is 50 – 150 meV. In the rest of the thesis we will look at regular lattices of sites with a *lattice constant* a . In that case the density of sites is $N_t = a^{-3}$ and there is no positional disorder.

In this thesis we consider the site energies to be either spatially *uncorrelated* or *correlated*. In the case of uncorrelated disorder, we distribute the site energies at each site randomly

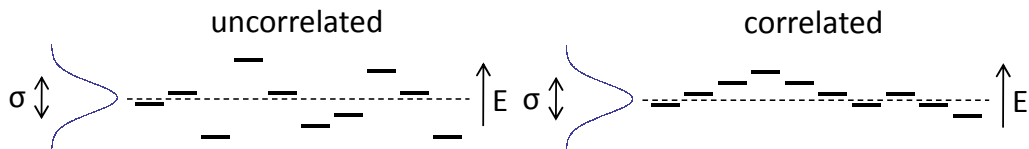


Figure 1.3: Schematic representations of disordered site energies (E) in the case of different kinds of correlations. The site energies are distributed according to a Gaussian DOS with a width σ . The representation at the left corresponds to spatially uncorrelated disorder and that at the right to spatially correlated disorder.

according to Eq. (1.1). In the case of correlated disorder, we take the site energies $E_{\mathbf{i}}$, with site $\mathbf{i} = \{i_x, i_y, i_z\}$ a three-dimensional vector, to be equal to the electrostatic energy resulting from random dipoles of equal magnitude d but random orientation at all other sites $\mathbf{j} \neq \mathbf{i}$. The resulting density of states is Gaussian, with a width σ proportional to d .^{24–26} The dimensionless correlation function $C(r)$ between the site energies is defined by

$$C(r = |\mathbf{R}_{\mathbf{ij}}|) \equiv \frac{\langle E_{\mathbf{i}} E_{\mathbf{j}} \rangle}{\sigma^2}, \quad (1.2)$$

in which $\langle \dots \rangle$ denotes an ensemble average over different random configurations of the dipole orientations. Numerical studies show that the correlation function is at an inter-site distance $r = a$ equal to $C(r = a) \approx 0.7$, at $r = 2a$ equal to $C(r = 2a) \approx 0.35$, and for larger inter-site distances equal to $C(r = |\mathbf{R}_{\mathbf{ij}}|) \approx 0.74a/|\mathbf{R}_{\mathbf{ij}}|$.²⁷

We note that thermally induced torsions of polymer chains²⁸ have also been proposed as the origin of spatial correlations between site energies in polymers. However, in this thesis we will limit ourselves to the above widely used dipole model as the origin of correlations.

1.5 Hopping transport

As discussed in the previous section, due to the structural disorder of the organic material charge carriers are located on localized sites. Therefore, transport of charges does not occur via band conduction, but takes place by the hopping of charge carriers from one site to another. The rate of hopping of a charge carrier between two sites depends on the overlap of the electronic wave functions of these two sites, which allows tunneling from one site to another. Whenever a charge carrier hops to a site with a higher (lower) site energy than the site that it came from, the difference in energy is accommodated for by the absorption (emission) of a phonon. The mechanism of phonon-assisted tunneling or "hopping" has been proposed by Mott and Conwell to explain DC conduction properties of inorganic semiconductors.^{29–31} Nowadays this mechanism is also used to describe the conductivity in a wide variety of organic materials. In this thesis we make use of the hopping formalism

of Miller and Abrahams.³² The rate of hopping of a charge carrier from site $\mathbf{i} = \{i_x, i_y, i_z\}$ to site $\mathbf{j} = \{j_x, j_y, j_z\}$, $W_{\mathbf{ij}}$, is then given by

$$\begin{aligned} W_{\mathbf{ij}} &= \nu_0 \exp \left[-2\alpha |\mathbf{R}_{\mathbf{ij}}| - \frac{E_{\mathbf{j}} - E_{\mathbf{i}} - eFR_{\mathbf{ij},x}}{k_{\text{B}}T} \right], & E_{\mathbf{j}} &\geq E_{\mathbf{i}} + eFR_{\mathbf{ij},x}, \\ W_{\mathbf{ij}} &= \nu_0 \exp [-2\alpha |\mathbf{R}_{\mathbf{ij}}|], & E_{\mathbf{j}} &< E_{\mathbf{i}} + eFR_{\mathbf{ij},x}, \end{aligned} \quad (1.3)$$

with ν_0 the attempt-to-jump frequency, α the inverse of the wave function decay length, $|\mathbf{R}_{\mathbf{ij}}| \equiv a|\mathbf{i} - \mathbf{j}|$ the distance between site \mathbf{i} and \mathbf{j} , k_{B} the Boltzmann constant, T the temperature, and $eFR_{\mathbf{ij},x} \equiv eFa(j_x - i_x)$ a contribution due to an applied field that is directed along the x -axis. The factor $\exp[-2\alpha |\mathbf{R}_{\mathbf{ij}}|]$ is the tunneling probability between sites with equal energy. The factor $\exp\left[-\frac{E_{\mathbf{j}} - E_{\mathbf{i}} - eFR_{\mathbf{ij},x}}{k_{\text{B}}T}\right]$ is a Boltzmann penalty for a charge hopping upwards in energy. This penalty is absent when a charge hops downwards in energy. The prefactor ν_0 is an attempt frequency that is of the order of a phonon frequency.

From Eq. (1.3) it becomes clear that the hopping transport depends on several factors. The energetic disorder and electric field play an important role. Charge carriers preferably hop to sites with a lower site energy. By increasing the temperature the Boltzmann penalty for hops upwards in energy becomes less strong. Furthermore, there is a trade-off between hops over a long distance to energetically favorable sites and hops over a short distance to energetically less favorable sites, leading to the phenomenon of variable-range hopping.³⁰

We suppose that a site can only be occupied by one charge carrier due to the high Coulomb penalty for the occupation of a site by two charges. When charge carriers are given enough time, they will generally move to those sites with the lowest energies. Once this has happened, we say that the system is in *equilibrium* (in the absence of a net current) or in *steady-state* (when a net current flows through the system). In equilibrium, the density of occupied states (DOOS), $n(E)$, is given by

$$n(E) = g(E) \frac{1}{1 + \exp(E - E_{\text{F}})/k_{\text{B}}T}, \quad (1.4)$$

with E_{F} the Fermi energy. The lower-energy tail of the DOS is now filled by the charge carriers. When the density of charge carriers in the device is low, charge carriers are hopping from a relatively low Fermi level to neighboring sites with site-energies which are on average much higher than the Fermi level. However, when the density of charge carriers in the device is high, the difference between the Fermi level and the site-energies of the neighboring sites will be on average small, due to the state-filling effects. At a fixed potential gradient, this leads to a higher current in the device.

It should be noted that the Miller-Abrahams hopping formalism is not the only hopping

formalism that can be found in the literature. When a charge carrier is placed in a solid, the atoms surrounding this charge carrier will be displaced and its energy will be effectively lowered. As a result, the charge carrier can be thought of as being positioned in a potential well caused by its own presence. The combination of the charge carrier and the polarization due to the displacement of the atoms is called a polaron. When these polaronic effects are important, one should use the Marcus hopping formalism.³³⁻³⁵ The rate of hopping of a charge carrier from site $\mathbf{i} = \{i_x, i_y, i_z\}$ to site $\mathbf{j} = \{j_x, j_y, j_z\}$ is then given by

$$W_{\text{Marcus},\mathbf{i}\mathbf{j}} = \nu_0 \sqrt{\frac{\pi}{4E_a k_B T}} \exp \left[-2\alpha |\mathbf{R}_{\mathbf{i}\mathbf{j}}| - \frac{E_a}{k_B T} - \frac{\Delta E_{\mathbf{i}\mathbf{j}}}{2k_B T} - \frac{(\Delta E_{\mathbf{i}\mathbf{j}})^2}{16E_a k_B T} \right] \quad (1.5)$$

with $\Delta E_{\mathbf{i}\mathbf{j}} = E_{\mathbf{j}} - E_{\mathbf{i}} - eF R_{\mathbf{i}\mathbf{j},x}$ the site-energy difference between sites \mathbf{j} and \mathbf{i} and E_a the polaron activation energy. If $\sigma \ll E_a$, the quadratic energy term in the exponent can be neglected. This approximation is justified in most disordered organic materials.³⁶

1.6 Models for charge transport in bulk systems

When an electric field is applied in an organic material, charge carriers will start to drift along this field. Due to the energetic disorder the speed at which the charge carriers move in the direction along the electric field is far from uniform. At a given moment in time, some charges will hop to sites that have a considerably lower energy than the surrounding sites, and will remain trapped for a relatively long time. Other charges hop along a path of energetically favorable sites and will therefore move relatively quickly. We are therefore interested in the average speed of the charge carriers, $\langle v \rangle$, which we also call *drift velocity*. By dividing the drift velocity by the applied electric field, F , we obtain the carrier mobility, μ ,

$$\mu = \frac{\langle v(F) \rangle}{F}. \quad (1.6)$$

The mobility can be calculated by various three-dimensional simulation approaches, like Master-Equation calculations and Monte-Carlo simulations. These simulation approaches will be explained in detail in the next chapter.

Monte-Carlo (MC) simulations of the hopping transport of a single carrier in a regular lattice of sites with site energies distributed according to an uncorrelated Gaussian DOS were performed by Bässler *et al.*^{37,38} These simulations showed a non-Arrhenius temperature dependence of the mobility

$$\mu(F = 0) = \mu_0 \exp \left[- \left(\frac{2}{3} \hat{\sigma} \right)^2 \right], \quad (1.7)$$

with μ_0 a constant mobility prefactor that is equal to the carrier mobility when no energetic disorder is present, and $\hat{\sigma} = \sigma/(k_B T)$ the dimensionless disorder strength. For the dependence on the electric field a Poole-Frenkel behavior was found:

$$\mu_{\text{GDM}} = \mu(F = 0) \exp \left[C(\hat{\sigma}^2 - 2.25)\sqrt{F} \right] \quad (1.8)$$

with C a prefactor of order unity. We will call this mobility function the Gaussian Disorder Model (GDM). We note that the effects of positional disorder were also investigated by Bässler *et al.* The result Eq. (1.8) is valid for the case of small positional disorder. We also note that the electric-field dependence Eq. (1.8) was found to be valid in a rather limited range of electric fields.

Experimental data obtained from time-of-flight measurements show a Poole-Frenkel behavior on a much broader field range than the GDM. Gartstein and Conwell pointed out that a spatially correlated potential for the charge carriers can better explain the experimental data.³⁹ This led to the Correlated Disorder Model (CDM), a model that agrees with the experimentally observed Poole-Frenkel behavior for a larger range of electric field strengths than the GDM:

$$\mu_{\text{CDM}} = \mu_0 \exp \left[- \left(\frac{3}{5} \hat{\sigma} \right)^2 + 0.78(\hat{\sigma}^{3/2} - 2)\sqrt{\frac{eaF}{\sigma}} \right]. \quad (1.9)$$

The calculations for the GDM and CDM were performed in the limit of small charge carrier densities. As we have argued in Section 1.5, transport properties are changed considerably by the state-filling effect when the charge carrier density is increased. For organic field-effect transistors (OFETs), in which the charge carrier density is much higher than in OLEDs, it was already known that the mobility has a strong dependence on the charge carrier density.⁴⁰ A strong dependence of the mobility on the carrier density was also found in disordered inorganic semiconductors.⁴¹ For the case of a Gaussian DOS with $\sigma \geq 2k_B T$ and very low carrier densities, the density of occupied states (DOOS) is approximately Gaussian, with the average of the DOOS equal to $-\sigma^2/(k_B T)$. In this regime, the carriers are effectively independent from each other and hence the mobility is independent of the carrier density. For very high carrier densities, the addition of extra charges leads to the filling of the DOS to higher energies. As explained in the previous section, this results in hops over a smaller energy difference. The transition from one regime to the other, occurs at the cross-over concentration $c_{\text{cross-over}} = (1/2) \times \exp[-\hat{\sigma}^2/2]$.⁴² Schmechel argued that the resulting enhancement of the mobility in a Gaussian DOS could explain the mobility

in disordered doped injection layers used in OLEDs, in which the carrier concentrations are very high.⁴³

Recently, Pasveer *et al.*⁴⁴ have shown that the effects of state-filling on the mobility can be described very well with an extension of the GDM, taking the density dependence into account, which led to the Extended Gaussian Disorder Model (EGDM). By numerically solving a master equation for the site occupational probabilities, the temperature, field, and hole-density, n_h , dependence of the mobility were studied. This study gave a good quantitative explanation for the concentration dependence of the hole mobility that was found experimentally by Tanase *et al.*⁴⁵ for hole-only devices based on a semiconducting polymer poly(*p*-phenylenevinylene) (PPV) derivative. The density dependence of the mobility was found to be much more important than the electric-field dependence in this experimental study. A similar extension of the CDM was made, leading to the Extended Correlated Disorder Model (ECDM).⁴⁶ Also in the ECDM, the mobility is dependent on the temperature, the charge carrier density, and the electric field strength.

1.7 Percolation and the three-dimensional structure of charge transport

Percolation is the probabilistic model describing the probability that percolating pathways are formed. What is meant by a percolating pathway depends on the system that is studied. The concept of percolation was first proposed in 1957 by Broadbent and Hammersley.⁴⁷ Percolation has been used to describe the temperature dependence of the DC conductivity in organic materials.^{48–50} Percolation arguments lead to the conclusion that the conductivity predominantly depends on the hopping between a single pair of sites. This pair of sites is called the *critical bond*. We now give a short description of how to determine this critical bond and how it influences the conductivity.

We assume for simplicity a regular lattice with the site energies distributed according to a Gaussian DOS. Provided that there is only a small electric field and that the thermal energy is small compared to the disorder strength, the conductance between two sites is given by⁵⁰

$$G_{ij} = G_0 \exp[-s_{ij}], \quad (1.10)$$

with G_0 a conductance prefactor and s_{ij} given by

$$s_{ij} = 2\alpha|\mathbf{R}_{ij}| + \frac{|E_i - E_F| + |E_j - E_F| + |E_i - E_j|}{2k_B T}. \quad (1.11)$$

The conductivity is determined by the critical bond with the critical conductance G_c ,

defined by the condition that removal of all $G_{ij} < G_c$ still gives a path through the entire lattice. This path is called a *percolating pathway*. The critical conductance is given by $G_c = G_0 \exp[-s_c]$. The value of s_c is called the (bond) *percolation threshold*. The bonds with bond conductance $G_{ij} > G_c$ contribute to the current while bonds with bond conductance $G_{ij} < G_c$ are bypassed by the current. The mobility is then given by

$$\mu \approx \frac{\sigma_c}{en} \approx \frac{G_c a}{en} \quad (1.12)$$

with $\sigma_c = G_c a$ the critical conductivity. The second equality only holds in the case of nearest-neighbor hopping. Generalization to finite electric fields and non-homogeneous situations (e.g. with spatially varying densities and fields) changes Eqs. (1.10) and (1.11) but concepts like critical bonds and percolating pathways still hold.

We conclude that conduction through disordered organic occurs by charges that move preferentially over three-dimensional percolating pathways across critical bonds. The current is strongly concentrated around these pathways, which results in the occurrence of so-called *current filaments*. The resulting strongly inhomogeneous character of the charge transport raises the question whether in the modeling of a realistic device the three-dimensional nature of the charge transport can be mapped onto a one-dimensional description with a small set of parameters. For charge transport in a homogeneous bulk system with uncorrelated or correlated Gaussian disorder the EGDM and ECDM give a good description of the mobility as a function of the temperature, electric field, and charge carrier density, with a relatively small set of parameters. However, it is not a priori clear that this is also the case for realistic devices in which the density and electric field may show significant gradients, especially near the electrodes.

1.8 Recombination

Electrons and holes in an OLED move to each other under the influence of an external electric field and their mutual attractive Coulombic interactions. When the distance between an electron and a hole is smaller than the capture radius, r_c , a Coulombically bonded pair will be formed. The capture radius is the distance at which the Coulomb interaction energy becomes equal to the thermal energy $k_B T$ and is given by $r_c = e^2 / (4\pi\epsilon_r\epsilon_0 k_B T)$, where ϵ_r is the relative dielectric constant of the organic material. Once the electron and hole have formed such a bonded pair it is very probable that they will recombine. When both the electron and hole are on the same site, an on-site exciton is formed. This on-site exciton can decay to the ground state, which leads to the recombination of the electron and the hole and to the emission of a photon, if the recombination is radiative.

Already in 1903, Langevin gave an expression for the total number of recombination events per second and per volume unit in an ionic gas system.⁵¹ We call this quantity *recombi-*

recombination rate, R . Since then the expression for the recombination rate has been successfully applied for numerous systems, including devices. The expression is given by

$$R_{\text{Lan}} = \frac{e(\mu_e + \mu_h)}{\epsilon_r \epsilon_0} n_e n_h \equiv \gamma_{\text{Lan}} n_e n_h, \quad (1.13)$$

with μ_e and μ_h the electron and hole mobility, respectively, n_e and n_h the electron and hole density, respectively, and γ_{Lan} the Langevin bimolecular recombination rate factor.

One of the underlying assumptions in the derivation of this expression is that the mean free path of the charge carriers λ is much smaller than the thermal capture radius. In previous sections we already saw that the transport of charges takes place by hopping between sites. The mean free path is thus of the order of the inter-site distance $a \approx 1\text{-}2$ nm. At room temperature and with a relative dielectric constant $\epsilon_r \approx 3$, a value typical for organic semiconductors, the thermal capture radius is $r_c \approx 18.5$ nm. Hence, the assumption $\lambda \ll r_c$ is valid.

Another assumption made in deriving Eq. (1.13) is that charge-carrier transport occurs homogeneously throughout the semiconductor. As we have seen in the previous section, the charge transport in disordered organic media is inhomogeneous, with percolating pathways along which most of the charges are transported. This raises the question whether Eq. (1.13) is still valid under such conditions.

Another issue that plays a role in this context is the possible correlation between the on-site energies of holes and electrons. In the case of correlation between on-site electron and hole energies electrons and holes may prefer to be located at the same sites. As a result, the current filaments of the electrons and holes overlap. In the case of anti-correlation between on-site electron and hole energies, sites with an energy favorable for electrons are unfavorable for holes and vice versa. In that case, the current filaments of the electrons avoid the current filaments of the holes. One would intuitively expect a larger recombination rate in the case of correlated energies than in the case of anti-correlated energies. Correlation between electron and hole energies can occur when the energetic disorder is caused by fluctuations in the local polarizability of the semiconductor or by differences in the length of conjugated segments. Anti-correlation between electron and hole energies can occur when the disorder is caused by fluctuations in the local electrostatic potential.

1.9 From three-dimensional modeling calculations and simulations to a predictive OLED model

The development of a complete and predictive *ab initio* OLED model consists of many different steps.

1. First, the microscopic nature of the organic material should be studied. Information about, for example, the packing of the molecules, the disorder (energetic and positional), the correlation between HOMO and LUMO levels, the energetic correlation, and the lattice of sites can be obtained by means of Molecular Dynamics simulations. By means of Density Functional Theory the transfer integrals, and from those the hopping rates between sites, can be calculated.
2. Second, the information obtained from the first step can be used as an input for the calculations of the three-dimensional current distribution in the presence of a uniform field and carrier concentration. This current distribution can be obtained by means of Master-Equation calculations or Monte-Carlo simulations. This distribution is inhomogeneous, because of the percolating nature of the charge-carrier transport. The resulting mobility reflects the complete microstructure of the material and the inhomogeneous current distribution.
3. Third, to be applicable in industry and other research groups, the mobility obtained in this way should be cast in a mobility function with as few model parameters as possible, which can then be used in *one-dimensional* drift-diffusion calculations. This can be done by means of theoretical percolation arguments, an approach which was for example used in the development of the EGDM.⁴⁴ As we will see in the following steps, the translation from results obtained with three-dimensional computer simulations to parameterizations that can be used in one-dimensional calculations is a common theme in this theses.
4. The fourth step is the calculation of the current in a single-carrier single-layer device. Electrodes are introduced and the interaction of charges with those electrodes by means of image-charges. The effect of space-charge is taken into account. Results for the current obtained from one-dimensional drift-diffusion calculations with a parameterized mobility function can be compared with three-dimensional simulations.
5. The fifth step is the calculation of the electronic processes in a single-layer double-carrier OLED. The drift-diffusion equation is solved for electrons and holes. Recombination of electrons and holes is taken into account by means of a position-dependent recombination rate. The results for the current and the recombination profile obtained from the one-dimensional modeling can again be compared with three-dimensional simulations. In this way models for the recombination rate can be tested.
6. The sixth step consists of generalizing the fifth step to a situation with multiple organic layers, with appropriate boundary conditions for the carrier densities and the electric field at the organic-organic interfaces. In a comparison with three-dimensional simulations models for the organic-organic boundary conditions can be tested.

7. In a seventh step exciton transport should be studied. Excitons are allowed to diffuse, to decay radiatively or non-radiatively.
8. The eighth and final step is the calculation of the light-outcoupling by solving the Maxwell equations.

By following all these steps a predictive one-dimensional OLED model is obtained, which gives the current and the output of light as a function of the applied voltage.

In this thesis we will study the mobility including Coulomb interactions between the charges in the presence of a uniform field and carrier concentration (second step). We will also study the current in single-carrier single-layer devices (fourth step). Furthermore, we study the radiative recombination of electrons and holes in a homogeneous bulk system in order to construct a position-dependent recombination rate (part of fifth step).

We make a simplification by skipping over the first step. Because there is at present practically no information available about the microstructure of OLED materials, we assume the sites to be ordered in a regular lattice. We do not expect that this simplification has a strong influence on charge transport properties. We expect that this simplification does have an influence on charge injection from electrodes and on the current across organic-organic interfaces, where charge densities occur that can vary by a large amount on the scale of a lattice constant. In such cases, we expect that the precise microstructure becomes important.

1.10 Scope of this thesis

In this thesis the three-dimensional character of charge transport and recombination in OLEDs is studied by means of two different simulation approaches: the Master-Equation (ME) approach and the Monte-Carlo (MC) approach. In the ME approach, the steady-state situation of a device is calculated by iteratively solving the master equation, which is an equation for the time-averaged occupational probabilities of the sites. In the MC approach, the hopping of the actual charges is simulated. Both approaches will be described in **Chapter 2**.

The EGDM and ECDM are based on results from ME calculations assuming a Gaussian DOS. As the master equation is an equation for the time-averaged occupational probabilities, the effects of Coulomb interactions cannot be taken into account in a consistent manner. In **Chapter 3** mobilities corresponding to the EGDM and ECDM as calculated by MC simulations are presented, in which Coulomb interactions can be taken into account. For low carrier densities the mobilities as obtained from MC calculations with and without taking into account Coulomb interactions agree quite well. The same is true in the case of high carrier densities and high electric fields. For high carrier densities and low electric

field, taking into account Coulomb interactions leads to a lower mobility. In this regime charges can be thought of as being trapped in the potential well formed by the Coulomb potential of the surrounding charges.

A modeling study of a single-carrier single-layer device is presented in **Chapter 4**. The calculations are based on the ME approach assuming an uncorrelated Gaussian DOS. The effects of space charge, the interaction of charges with the electrodes in the form of an image charge potential, and an injection barrier are taken into account. For low injection barriers, the current is almost independent of the injection barrier. In this regime, the injection is predominantly limited by the space charge in the devices, therefore we call this regime space-charge-limited. When the injection barrier increases the device enters the injection-limited regime in which the injection is predominantly limited by the injection barrier itself. The simulation model treats the space-charge-limited-current regime, the injection-limited-current regime and the transition between those two regimes. The results are compared with a one-dimensional continuum drift-diffusion model based on the EGDM. In this drift-diffusion model the effective lowering of the injection barrier by the image potential is taken into account. Furthermore, it is shown that the three-dimensional current density can be highly filamentary for voltages, device thicknesses, and disorder strengths that are realistic for organic light-emitting diodes. It is shown that for devices with a high injection barrier and a high disorder strength the current filaments become one-dimensional. In this regime a good agreement is obtained with a model assuming injection and transport over one-dimensional pathways.

In the modeling study described in Chapter 4 Coulomb interactions are taken into account in a layer-averaged way, by solving a one-dimensional Poisson equation with the appropriate boundary conditions, while the interaction of a charge with its image charge is taken into account explicitly. This approach cannot be fully consistent, since the interactions with image charges are also included via the boundary conditions in the one-dimensional Poisson equation for the space charge, albeit in a layer-averaged way. This leads to a double-counting problem that cannot be solved within the ME approach. This double-counting problem can be avoided in the MC approach. In **Chapter 5** a MC modeling study of single-carrier single-layer devices is presented in which the Coulombic interactions are taken into account in an explicit way, including the Coulomb interactions of charges with the image charges of other charges. Both a correlated as well as an uncorrelated Gaussian DOS is considered. It is shown that in the case of uncorrelated disorder and for injection barriers higher than 0.3 eV, the current-voltage characteristics from the MC simulations can be nicely described by a one-dimensional drift-diffusion model. However, for injection barriers lower than 0.3 eV, the current is significantly decreased when Coulomb interactions are taken into account explicitly.

The recombination rate is traditionally described by the Langevin formula, with the sum of the electron and hole mobilities as a proportionality factor. The underlying assumption for this formula is that charge transport occurs homogeneously. As is shown in Chapters 3 and 4 the current in disordered organic media is far from homogeneous. In **Chapter 6**

it is shown that the Langevin formula is still valid in disordered organic media, provided that a change of the charge carrier mobilities due to the presence of the charge carriers of the opposite type is taken into account. For a finite electric field, deviations from the Langevin formula are found, but these deviations are small in the field regime relevant for OLED modeling.

As a step beyond steady-state three-dimensional modeling, we also had a look at the relaxational properties of charge transport in disordered organic media. The results are shown in **Chapter 7**. When a charge is injected in the organic medium, the current is immediately after the injection event somewhat higher than the steady-state current. It takes time before the charge is relaxed in the Gaussian DOS. Results of both the relaxation of the current as well as the energy of the visited sites are shown.

In **Chapter 8** conclusions and an outlook are presented.

References

- [1] Letheby, H. *J. Chem. Soc.* **1862**, 15, 161.
- [2] Goppelsroeder, F. *Die Internationale Electrotechnische Ausstellung 1891*, 18, 978.
- [3] Goppelsroeder, F. *Die Internationale Electrotechnische Ausstellung 1891*, 18, 1047.
- [4] McNeill, R.; Siudak, R.; Wardlaw, J.; Weiss, D. *Aust. J. Chem.* **1963**, 16, 1056.
- [5] Bolto, B.; Weiss, D. *Aust. J. Chem.* **1963**, 16, 1076.
- [6] Bolto, B.; McNeill, R.; Weiss, D. *Aust. J. Chem.* **1963**, 16, 1090.
- [7] McGinness, J.; Corry, P.; Proctor, P. *Science* **1974**, 183, 853.
- [8] Pai, D.; Springett, B. *Rev. Mod. Phys.* **1993**, 65, 163.
- [9] Shirakawa, H.; Louis, E.; MacDiarmid, A.; Chiang, C.; Heeger, A. *J. Chem. Soc. Chem Comm.* **1977**, 16, 578.
- [10] http://nobelprize.org/nobel_prizes/chemistry/laureates/2000/press.htmllax
- [11] Burroughes, J.; Bradley, D.; Brown, A.; Marks, R.; Mackay, K.; Friend, R.; Burns, P.; Holmes, A. *Nature* **1990**, 347, 539.
- [12] Drury, C.; Mutsaers, C.; Hart, C.; Matters, M.; de Leeuw, D. *Appl. Phys. Lett.* **1998**, 73, 108.

-
- [13] Brabec, C.; Dyakonov, V.; Parisi, J.; Sariciftci, N. *Organic Photovoltaics: Concepts and Realization*; Springer-Verlag: Berlin, 2003.
- [14] Bernanose, A.; Comte, M.; Vouaux, P. *J. Chim. Phys.* **1953**, *50*, 64.
- [15] Bernanose, A.; Vouaux, P. *J. Chim. Phys.* **1953**, *50*, 261.
- [16] Bernanose, A. *J. Chim. Phys.* **1955**, *52*, 396.
- [17] Bernanose, A.; Vouaux, P. *J. Chim. Phys.* **1955**, *52*, 509.
- [18] Partridge, R. *Polymer* **1983**, *24*, 733.
- [19] Partridge, R. *Polymer* **1983**, *24*, 739.
- [20] Partridge, R. *Polymer* **1983**, *24*, 748.
- [21] Partridge, R. *Polymer* **1983**, *24*, 755.
- [22] Tang, C.; VanSlyke, S. *Appl. Phys. Lett.* **1987**, *51*, 913.
- [23] Mandoc, M.; de Boer, B.; Paasch, G.; Blom, P. *Phys. Rev. B* **2007**, *75*, 193202.
- [24] Novikov, S.; Vannikov, A. *JETP* **1994**, *79*, 482.
- [25] Young, R. *Philos. Mag. B* **1995**, *72*, 435.
- [26] Novikov, S.; Dunlap, D.; Kenkre, V.; Parris, P.; Vannikov, A. *Phys. Rev. Lett.* **1998**, *81*, 4472.
- [27] Novikov, S.; Vannikov, A. *J. Phys. Chem.* **1995**, *99*, 14573.
- [28] Yu, Z.; Smith, D.; Saxena, A.; Martin, R.; Bishop, A. *Phys. Rev. Lett.* **2000**, *84*, 721.
- [29] Mott, N. *J. Non-Cryst. Solids* **1968**, *1*, 1.
- [30] Mott, N. *Phil. Mag.* **1969**, *19*, 835.
- [31] Conwell, E. *Phys. Rev.* **1956**, *103*, 51.
- [32] Miller, A.; Abrahams, E. *Phys. Rev.* **1960**, *120*, 745.
- [33] Marcus, R. *J. Chem. Phys.* **1956**, *24*, 966.
- [34] Marcus, R. *Rev. Mod. Phys.* **1993**, *65*, 599.
- [35] Fishchuck, I.; Kadashchuk, A.; Bäessler, H.; Nešpůrek, S. *Phys. Rev. B* **2003**, *67*, 224303.

- [36] Kreouzis, T.; Poplavskyy, D.; Tuladhar, S. M.; Campoy-Quiles, M.; Nelson, J.; Campbell, A. J.; Bradley, D. D. C. *Phys. Rev. B* **2006**, *73*, 235201.
- [37] Pautmeier, L.; Richert, R.; Bäessler, H. *Synth. Met.* **1990**, *37*, 271.
- [38] Bäessler, H. *Phys. Stat. Sol. (b)* **1993**, *175*, 15.
- [39] Gartstein, Y.; Conwell, E. *Chem. Phys. Lett.* **1995**, *245*, 351.
- [40] Vissenberg, M.; Matters, M. *Phys. Rev. B* **1998**, *57*, 12964.
- [41] Monroe, D. *Phys. Rev. Lett.* **1985**, *54*, 146.
- [42] Coehoorn, R.; Pasveer, W.; Bobbert, P.; Michels, M. *Phys. Rev. B* **2005**, *72*, 155206.
- [43] Schmechel, R. *Phys. Rev. B* **2002**, *66*, 235206.
- [44] Pasveer, W.; Cottaar, J.; Tanase, C.; Coehoorn, R.; Bobbert, P.; Blom, P.; de Leeuw, D.; Michels, M. *Phys. Rev. Lett.* **2005**, *94*, 206601.
- [45] Tanase, C.; Blom, P.; de Leeuw, D. *Phys. Rev. B* **2004**, *70*, 193202.
- [46] Bouhassoune, M.; van Mensfoort, S.; Bobbert, P.; Coehoorn, R. *Org. Electron.* **2009**, *10*, 437.
- [47] Broadbent, S.; Hammersley, J. *Proc. Cambridge Philos. Soc.* **1957**, *53*, 629.
- [48] Ambegaokar, V.; Halperin, B.; Langer, J. *Phys. Rev. B* **1971**, *4*, 2612.
- [49] Pollak, M. *J. Non-Cryst. Solids* **1972**, *11*, 1.
- [50] Shklovskii, B.; Efros, A. *Electronic Properties of Doped Semiconductors*; Springer-Verlag: Berlin, 1985.
- [51] Langevin, M. *Ann. Chim. Phys* **1903**, *7*, 433.

Chapter 2

Computational methods for device calculations

ABSTRACT

For the three-dimensional device modeling, we make use of two different modeling approaches: the Master-Equation approach and the Monte-Carlo approach. The master equation describes the steady-state occupational probabilities of sites in terms of the Pauli master equation. This equation is solvable by means of an iterative scheme, after which relevant quantities like the mobility and current are obtained. The Master-Equation model has two disadvantages. The model only describes occupational probabilities and therefore it is not possible to treat Coulomb interactions in a consistent manner. Moreover, correlations in occupational probabilities are neglected. These two disadvantages can be overcome by using a Monte-Carlo model, in which the motion of the actual charges are simulated.

In this chapter, both simulation methods are presented for the case of charge-carrier transport in a single-carrier homogeneous bulk system made of an organic semiconducting material.

2.1 Master-Equation approach

The master equation is a differential equation describing the time evolution for the occupational probability of a site.¹ The occupational probability of a site is defined as the probability that a site is occupied by a charge. The master equation is given by:

$$\frac{dp_i}{dt} = - \sum_{j \neq i} [W_{ij} p_i (1 - p_j) - W_{ji} p_j (1 - p_i)], \quad (2.1)$$

with p_i the occupational probability of site \mathbf{i} and W_{ij} the rate for the transition from site \mathbf{i} to site \mathbf{j} . The factors $1 - p_j$ account, in a mean field approximation, for the fact that a site can only be occupied by one charge, due to the high Coulomb penalty for the presence of two charges on one site. The sum is over all sites \mathbf{j} "neighboring" with site \mathbf{i} . A site \mathbf{j} is "neighboring" site \mathbf{i} when the distance between the two sites is smaller than the maximum hopping distance. When the lattice is simple cubic, the maximum hopping distance is a (*nearest-neighbor hopping*, which means hopping to the nearest 6 neighbors), $\sqrt{2}a$ (*next-nearest-neighbor hopping*, which means hopping to the nearest 18 neighbors) or $\sqrt{3}a$ (*2nd-next-nearest-neighbor hopping*, which means hopping to the nearest 26 neighbors). In this thesis we always assume a maximum hopping distance of $\sqrt{3}a$, which is sufficient for the cases we will consider.

We are interested in the steady-state situation of the system. In this situation, $dp_i/dt = 0$ for every site \mathbf{i} . Then

$$0 = \sum_{j \neq i} [W_{ij} p_i (1 - p_j) - W_{ji} p_j (1 - p_i)]. \quad (2.2)$$

The particle current J_{ij} between two neighboring sites \mathbf{i} and \mathbf{j} is given by

$$J_{ij} = W_{ij} p_i (1 - p_j). \quad (2.3)$$

When the system of equations given by Eq. 2.2 is solved, we obtain the total current density, J , by summing the particle current over all pairs of sites \mathbf{ij} in the direction of the electric field. Assuming that the electric field is directed in the x -direction, the current density is then given by

$$J = \frac{e}{a^3 N} \sum_{\mathbf{ij}} W_{ij} p_i (1 - p_j) R_{ij,x} \quad (2.4)$$

with N the total number of sites in the simulation box and $R_{ij,x} \equiv a(j_x - i_x)$ the hopping distance in the x -direction.

2.2 Solving the steady-state master equation for a homogeneous bulk system 23

The mobility is given by:

$$\mu = \frac{J}{enF} = \frac{1}{a^3nFN} \sum_{\{i,j\}} W_{ij} p_i (1 - p_j) R_{ij,x} \quad (2.5)$$

with n the charge carrier density and F the electric field strength.

2.2 Solving the steady-state master equation for a homogeneous bulk system

In this subsection we present an algorithm for solving the steady-state master equation (Eq. 2.2) for a homogeneous single-carrier bulk system with an applied field F . The one-dimensional steady-state master equation can be solved analytically in an exact way, as has been shown by Derrida.² For the situation of two and three dimensions this equation has to be solved numerically.

In our calculations we make use of a regular periodic three-dimensional simple-cubic lattice of sites. We assume that the lattice constant is equal to a and that the lattice is periodic with periodicity L_x, L_y , and L_z in the x -, y -, and z -direction, respectively. The sites \mathbf{i} are then positioned on $\{x, y, z\} = a\{i_x, i_y, i_z\}$ with $i_x \in 0, L_x - 1, i_y \in 0, L_y - 1$, and $i_z \in 0, L_z - 1$. Due to the periodicity property, a site $\mathbf{i}_{\text{non-periodic}} = n_x L_x + i_x, n_y L_y + i_y, n_z L_z + i_z$ with arbitrary integers n_x, n_y , and n_z is then the same site as $\mathbf{i}_{\text{periodic}} = i_x, i_y, i_z$. By making use of a periodic lattice, one does not have to care about the boundary of this lattice.

The approach that we follow is the one developed by Yu *et al.*^{3,4} By algebraically solving Eq. 2.2 for p_i we get

$$p_i = \frac{\sum_{j \neq i} W_{ji} p_j}{\sum_{j \neq i} [W_{ij}(1 - p_j) + W_{ji} p_j]}. \quad (2.6)$$

In the following iteration scheme, we define $p_i^{(n)}$ to be the solution for p_i of Eq. 2.6 in the n -th iteration. The initial value for the p_i 's is given by $p_i^{(0)}$. Using Eq. 2.6 we make use of the following iteration scheme:

1. Define for every site a random contribution, $E_{\text{rand},i}$, to the site-energy E_i drawn from a normalized Gaussian DOS with a standard deviation σ . The random site-energy contributions are the HOMO and LUMO levels of the material in the case of electron and hole transport, respectively.

2. Start with initial values for the $p_{\mathbf{i}}^{(0)}$. A reasonably good choice for the initial value is given by assuming the $p_{\mathbf{i}}^{(0)}$ to be distributed according to a Fermi-Dirac distribution:

$$p_{\mathbf{i}}^{(0)} = \frac{1}{\exp\left(\frac{E_{\mathbf{i}} - E_{\text{F}}}{k_{\text{B}}T}\right) + 1}, \quad (2.7)$$

where the Fermi level E_{F} can be calculated by the condition that the charge-carrier density is constant and equal to n . This condition is given by

$$\sum_{\mathbf{i}} p_{\mathbf{i}} = Nn, \quad (2.8)$$

An additional constraint is posed by the fact that the $p_{\mathbf{i}}$'s are occupation probabilities, i.e., $0 \leq p_{\mathbf{i}} \leq 1$.

3. At every iteration step, we sequentially solve Eq. 2.6 for every site \mathbf{i} to obtain new $p_{\mathbf{i}}$'s. This step is done via implicit calculation. Specifically, this means that at the n -th iteration step we use $p_{\mathbf{j}}^{(n)}$ in Eq. 2.6 whenever already calculated; otherwise we use $p_{\mathbf{j}}^{(n-1)}$ from the previous iteration step. In this way we avoid convergence problems encountered when the "new" $p_{\mathbf{i}}^{(n)}$ are calculated by Eq 2.6 via explicit iteration, meaning that only the "old" $p_{\mathbf{i}}^{(n-1)}$'s are used.^{3,4}
4. When Eq. 2.6 is solved sequentially for all sites, we could scale all $p_{\mathbf{i}}$'s by the same proportionality factor in order to satisfy condition Eq. 2.8. A problem with this approach is that the condition $0 \leq p_{\mathbf{i}} \leq 1$ is not automatically satisfied.

Another way to scale all $p_{\mathbf{i}}$'s is to first obtain a site-resolved energy $\bar{E}_{\mathbf{i}}$ from the following equation:

$$p_{\mathbf{i}}^{\text{old}} = \frac{1}{\exp\left(\frac{\bar{E}_{\mathbf{i}}}{k_{\text{B}}T}\right) + 1}. \quad (2.9)$$

By adding a constant shift $\Delta\bar{E}$ to the energies $\bar{E}_{\mathbf{i}}$, we obtain the new occupational probabilities $p_{\mathbf{i}}^{\text{new}}$:

$$p_{\mathbf{i}}^{\text{new}} = \frac{1}{\exp\left(\frac{\bar{E}_{\mathbf{i}} + \Delta\bar{E}}{k_{\text{B}}T}\right) + 1}, \quad (2.10)$$

where the shift $\Delta\bar{E}$ is determined by condition Eq. 2.8. In this way, we obtain occupational probabilities for which both conditions Eq. 2.8 and $0 \leq p_{\mathbf{i}} \leq 1$ are satisfied.

5. After a predefined number of iteration steps, the mobility μ (Eq. 2.5) is calculated. When this mobility has converged to a predefined level of accuracy, the iteration stops; otherwise we go back to step 3.
6. All steps are repeated for a number of disorder configurations. The final mobility is the average of the mobilities obtained for each disorder configuration.

The Master-Equation approach has some disadvantages. The master equation is obtained by a mean-field approximation, meaning that correlations between occupational probabilities are neglected. By taking into account correlations between the occupational probabilities of pairs of neighboring sites it was shown by Cottaar *et al.* that the effect of such correlations on the mobility is very small, with a maximum difference of 2-3 %.⁵ The effect of correlations between the occupational probabilities of clusters of more than two neighboring sites on the mobility has not yet been evaluated. However, we will show in Chapter 3 and 5 that the effect of taking into account all correlations between the occupational probabilities on the mobility is minor.

A second disadvantage is that Coulomb interactions cannot be taken into account in a consistent manner in the Master-Equation approach, because in this approach we are working with time-averaged occupational probabilities, and not with the actual occupational probabilities.

These two disadvantages can be overcome by performing Monte-Carlo simulations instead of Master-Equation calculations. In the next section we will elaborate on the Monte-Carlo approach.

2.3 Kinetic Monte-Carlo approach

In this section we will describe a Monte-Carlo (MC) approach to calculate the mobility in a homogeneous single-carrier bulk system with an applied field F and with Coulomb interactions between charges. Monte-Carlo algorithms are a broad class of computer algorithms, in which a set of events is sampled in a random fashion. This set of events is in general not static, but changes dynamically after every sampling step. For our simulations we make use of the so-called kinetic Monte-Carlo (kMC) method, which is also known as dynamical Monte-Carlo method. The kMC method was first used in 1966 by Young *et al.*,⁶ but is more known by the work of Bortz *et al.*⁷ in 1975, who simulated the Ising model. Since then it has been used for a wide variety of problems in physics and chemistry.

The advantage of MC simulations over Master-Equation calculations is that the dynamics of the charges themselves is calculated, instead of the occupational probabilities of the sites. As a result, it is possible to simulate in a consistent manner Coulomb interactions between charges, by adding the Coulomb interaction energy U_i due to the Coulomb potential of

all charges around site \mathbf{i} to the energy of site \mathbf{i} . Hence, the site-energy consists of two contributions, a random contribution $E_{\text{rand},\mathbf{i}}$, which is distributed according to a Gaussian DOS, and the Coulomb interaction energy $U_{\mathbf{i}}$.

There are several different methods available to take Coulomb interactions into account. First of all, there is the possibility to take the interaction between all pairs of charges into account explicitly, but this is computationally very expensive. Approaches like the Ewald or Lekner summation approach make use of the periodicity of the lattice to take the infinite number of periodic copies of charges into account via a computationally efficient summation.⁸⁻¹¹ However, these approaches are still quite expensive. In our simulations we therefore use the following finite-range variant of the Coulomb potential V_c :

$$V_c(|R_{\mathbf{ij}}|) = \begin{cases} \frac{e}{4\pi\epsilon_r\epsilon_0} \left(\frac{1}{|R_{\mathbf{ij}}|} - \frac{1}{R_c} \right), & 0 < |R_{\mathbf{ij}}| \leq R_c, \\ 0, & |R_{\mathbf{ij}}| > R_c, \end{cases} \quad (2.11)$$

with R_c a cut-off radius. The interaction energy $U_{\mathbf{i}}$ is then given by

$$U_{\mathbf{i}} = \sum_{\mathbf{j} \neq \mathbf{i}} e_{\mathbf{j}} V_c(R_{\mathbf{ij}}), \quad (2.12)$$

with $e_{\mathbf{j}} = e$ when a charge is present on site \mathbf{j} and $e_{\mathbf{j}} = 0$ when the site is empty.

With this expression, only the Coulomb interactions between pairs of charges that are less than a distance R_c from each other are taken into account. By taking $R_c = \infty$ we obtain full exactness. By running the same simulation for different values of R_c we obtain the dependence of the mobility or current on R_c . From this we can make a choice for a value of R_c that gives a good compromise between accuracy and computational speed.

The term $-1/R_c$ is added in Eq. 2.11 to make the Coulomb potential smooth and to prevent the existence of an energy barrier for charges hopping from sites outside of a sphere of radius R_c around a site with a charge to sites inside of this sphere.

2.4 Kinetic Monte-Carlo scheme for a homogeneous bulk system

In this subsection we describe the kinetic Monte-Carlo method.

We make use of the following scheme:

1. Initialization of site-energies. Define for every site \mathbf{i} a random contribution, $E_{\text{rand},\mathbf{i}}$, to the site-energy $E_{\mathbf{i}}$, drawn from a normalized Gaussian DOS with a standard deviation

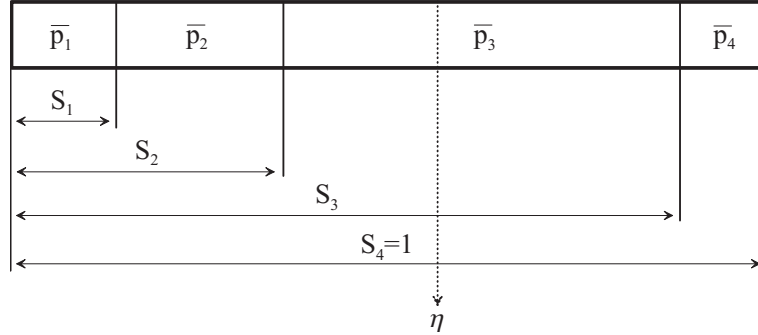


Figure 2.1: Placement of a charge in the system. The interval $(0, 1)$ is subdivided into intervals with lengths equal to the probabilities \bar{p}_k . The partial sums S_k are calculated. A random number $\eta \in (0, 1)$ is drawn. The chosen site is the one with index k for which $S_{k-1} \leq \eta \leq S_k$.

σ . The random site-energy contributions are the HOMO and LUMO levels of the material in the case of electron and hole transport, respectively.

2. Initialization of site occupational probabilities. For every site we define an occupational probability, p_i , that the site is occupied by a charge. The probability is given by the Fermi-Dirac distribution:

$$p_i = \frac{1}{\exp\left(\frac{E_{\text{rand},i} - E_F}{k_B T}\right) + 1} \quad (2.13)$$

The probability, \bar{p}_i , that out of the set of all sites, site i is chosen is then given by

$$\bar{p}_i = \frac{p_i}{\sum_j p_j} \quad (2.14)$$

3. Initial placement of charges. We place charges at sites with a probability given by Eq. 2.14. To choose the sites, we make use of the following algorithm. First, we define for every site an index $k \in \{1, \dots, k_{\text{max}}\}$, with k_{max} the total number of sites. We then define for every index $k \in \{1, \dots, k_{\text{max}}\}$ a partial sum S_k given by

$$S_k = \sum_{m=1}^k \bar{p}_m. \quad (2.15)$$

Note that for every $k \in \{1, \dots, k_{\text{max}}\}$ the length of the interval $[S_{k-1}, S_k]$ is equal to the probability \bar{p}_k . The length of the sum of all intervals is equal to 1, hence $S_{k_{\text{max}}} = 1$.

We draw a random real number η from the interval $[0, 1]$. Then we find the index k such that $S_{k-1} \leq \eta \leq S_k$. This gives us the site on which a charge will be placed; see

Fig. 2.1. We place a charge on that site. We set the probability that this site will be occupied again to 0, i.e. $\bar{p}_k = 0$. Because the probability \bar{p}_k has changed, all partial sums given by Eq. 2.17 have to be recalculated. We repeat the placement of charges until all charges are placed on the lattice.

4. Calculation of Coulomb interactions. We calculate the interaction energy, due to surrounding charges, for every occupied site and its neighboring sites by using Eq. 2.12.
5. Choice of hopping event. We first calculate all hopping rates $W_{\mathbf{i}\mathbf{j}}$ for hops from an occupied site to an unoccupied site according to Eq. 1.3. To prevent the hopping of a charge from an occupied site to an occupied site, we set the rate for such a hopping event equal to 0. The probability, $\bar{W}_{\mathbf{i}\mathbf{j}}$, that out of the set of all hopping rates, the rate for hopping from site \mathbf{i} to site \mathbf{j} is chosen, is given by

$$\bar{W}_{\mathbf{i}\mathbf{j}} = \frac{W_{\mathbf{i}\mathbf{j}}}{\sum_{\{\mathbf{k},\mathbf{m}\}} W_{\mathbf{k}\mathbf{m}}}, \quad (2.16)$$

where we sum over all pairs of neighboring sites.

We randomly choose a hopping event with a probability equal to Eq. 2.16. The way in which a random hopping event is chosen is analogous to the way in which the initial locations of the charges are chosen.

We define for every possible hopping event an integer index $h \in \{1, \dots, h_{\max}\}$ with h_{\max} the total number of hopping events. Then we define for every index $h \in \{1, \dots, h_{\max}\}$ a partial sum H_h given by

$$H_h = \sum_{m=1}^h \bar{W}_m. \quad (2.17)$$

For every $h \in \{1, \dots, h_{\max}\}$, the length of the interval (H_{h-1}, H_h) is equal to the probability \bar{W}_h . Moreover, $H_{h_{\max}} = 1$.

We draw a random real number η from the interval $[0, 1]$. We then find the index h such that $H_{h-1} \leq \eta \leq H_h$. This gives us the hopping event that will occur. The hopping event occurs by moving the charge from the site from which it hops to the site to which it hops.

6. Calculation of simulation time. After every hopping event, we add the waiting time t that has passed until the event took place to the total simulation time. This time is obtained by drawing a random number from the following exponential waiting-time distribution:

$$\begin{aligned} \tau(t) &= W_{\text{tot}} \exp[-W_{\text{tot}}t], & t \geq 0, \\ \tau(t) &= 0, & t < 0, \end{aligned} \quad (2.18)$$

with W_{tot} the sum of all hopping rates W_{ij} :

$$W_{\text{tot}} = \sum_{\{\mathbf{k}, \mathbf{m}\}} W_{\mathbf{k}, \mathbf{m}}. \quad (2.19)$$

The justification for using the distribution given by Eq. 2.18 is given in the appendix of this chapter.

We also keep track of the total number of hops, x^+ , along the electric field and the total number of hops, x^- , against the electric field.

We now return to step 4.

7. Equilibration. Every time that a predefined number of hops has occurred, we calculate the current, I , via the following expression:

$$I = \frac{e(x^+ - x^-)}{t_{\text{sim}} L_x}. \quad (2.20)$$

We keep track of the time-evolution of the current I . After the charges are placed into the system, it will take some time before the current has reached its steady-state value, because the charges have not relaxed yet. When the current stabilizes, the equilibration is stopped. We set the simulation time t_{sim} , the total hopping distance parallel along the electric field, f , and against the electric field, b , equal to 0 and we return to step 4.

In this way, effects due to the relaxation of charges or other initialization effects are not taken into account in the calculation of the steady-state current I .

8. Calculation of the equilibrium current. Every time that a predefined number of hops has occurred, we calculate the current, I , with Eq. 2.20.

If the number of hops is too small, the sampling for the current is inadequate. If the number of hops is too large, we are wasting computational time. Whenever a converged current I has been obtained, the simulation stops. Otherwise we return to the loop consisting of steps 4-6.

9. Calculation of the mobility. The mobility μ is obtained from

$$\mu = \frac{I}{enFL_y L_z a^2}, \quad (2.21)$$

where the electric field is pointing in the x -direction.

10. All steps are repeated for a number of disorder configurations. The final current or mobility is the average of the currents or mobilities obtained for all disorder configurations.

This scheme will be used for the calculation of the mobility for a homogeneous system in Chapter 3. An analogous scheme will be used in the Monte-Carlo simulations of a complete single-layer single-carrier device in Chapter 5.

Appendix - Derivation of the exponential waiting-time distribution Eq. 2.18

The hopping of a single charge is a Poisson process, i.e., the probability to make a hop in a time interval of a certain length is constant and independent of the history of the system. The probability that a hop occurs in the time interval $[t_a, t_a + \Delta t]$, with Δt an infinitesimally small time change, is then given by $P = r\Delta t + O((\Delta t)^2)$, where r is the hopping rate. Here, t_a is an initial time. The probability that a hop does not occur in this time interval is then given by $Q = 1 - P = 1 - r\Delta t + O((\Delta t)^2)$. Let us now take an integer k and denote $t = k\Delta t$. The probability that a hop does not occur in the time interval $[t_a, t_a + k\Delta t]$ is $Q = (1 - r\Delta t + O((\Delta t)^2))^k = (1 - rt/k + O((\Delta t)^2))^k$. For large k we get $\lim_{k \rightarrow \infty} Q = \exp(-rt)$. The probability that a hop will occur in the time interval $[t_a, t_a + k\Delta t]$ with k large is then given by $P = 1 - \exp(-rt)$. This is a cumulative distribution function. By taking the derivative we get the probability distribution function for the waiting time until a hop will occur. This probability function is then given by $f(t) = r \exp(-rt)$.

The above result is valid for the case of one hop of a single charge. Denote now by $R = \sum_i r_i$ the sum of all hopping rates r_i of all charges. The probability that no hop will take place in the time interval $[t_a, t_a + \Delta t]$ is given by $Q = \prod_i (1 - r_i \Delta t + O((\Delta t)^2)) \approx (1 - \sum_i r_i \Delta t) = (1 - Rt)$. The probability that a hop will occur in the time interval $[t_a, t_a + k\Delta t]$ with k large is then given by $P = 1 - R \exp(-Rt)$. By taking the derivative we obtain Eq. 2.18.

References

- [1] Böttger, H.; Bryksin, V. *Hopping Conduction in Solids*; Akademie-Verlag: Berlin, 1985.
- [2] Derrida, B. *J. Stat. Phys.* **1983**, *31*, 433.
- [3] Yu, Z.; Smith, D.; Saxena, A.; Martin, R.; Bishop, A. *Phys. Rev. B* **2001**, *63*, 085202.
- [4] Yu, Z.; Smith, D.; Saxena, A.; Martin, R.; Bishop, A. *Phys. Rev. Lett.* **2000**, *84*, 721.
- [5] Cottaar, J.; Bobbert, P. *Phys. Rev. B* **2006**, *74*, 115204.
- [6] Young, W.; Elcock, E. *Proc. Phys. Soc.* **1966**, *89*, 735.

- [7] Bortz, A.; Kalos, M.; Lebowitz, J. *J. Comput. Phys.* **1975**, *17*, 10.
- [8] Ewald, P. *Ann. Phys.* **1921**, *369*, 253.
- [9] Frenkel, D.; Smit, B. *Understanding Molecular Simulation*; Academic Press: London, 1996.
- [10] Lekner, J. *Phys. A* **1989**, *157*, 826.
- [11] Lekner, J. *Phys. A* **1991**, *176*, 485.

Chapter 3

Monte-Carlo study of the charge-carrier mobility in disordered semiconducting organic materials

ABSTRACT

We present the results of a Monte-Carlo study of the charge-carrier mobility in disordered organic semiconductors. The density of states is assumed to be Gaussian. The Coulomb interactions between charges are taken into account explicitly. We find that for low charge-carrier densities it is not necessary to take Coulomb interactions into account. However, for high carrier densities Coulomb interactions lead to an effectively lower mobility for low electric fields. For high electric fields the trapping effect disappears and the mobility with Coulomb interactions agrees reasonably well with the mobility without Coulomb interactions.

3.1 Introduction

The disorder in organic semiconductors used in OLEDs is often modeled by assuming that the on-site energies are random variables, taken from a Gaussian density of states (DOS). Monte-Carlo (MC) simulations of the hopping transport of single carriers (the low carrier-density Boltzmann limit) in a Gaussian DOS were performed by Bäessler *et al.*,^{1,2} showing a non-Arrhenius temperature dependence $\mu \propto \exp[-(2/3\hat{\sigma})^2]$ of the charge-carrier mobility μ , with $\hat{\sigma} \equiv \sigma/k_{\text{B}}T$ the disorder parameter, T the temperature, k_{B} the Boltzmann constant, and σ the width of the Gaussian DOS. This is usually referred to as the Gaussian Disorder Model (GDM). For the dependence on the electric field, F , a Poole-Frenkel $\mu \propto \exp[\gamma\sqrt{F}]$ behavior was found, in a limited field range, where the factor γ depends on temperature. Gartstein and Conwell pointed out that a spatially correlated potential for the charge carriers is needed to better explain experimental data. These data suggest the existence of Poole-Frenkel behavior in a rather wide region of field strengths.³ Their work led to the introduction of the Correlated Disorder Model (CDM). Several possible causes for this correlation were given, such as the presence of electric dipoles^{4,5} or (in the case of polymers) thermally induced torsions of the polymer chains.⁶

For a long time, it has been known that the mobility in disordered inorganic⁷ and organic⁸ materials is not only a function of the temperature and electric field, but also of the carrier density. This dependence has to be accounted for at densities for which state-filling effects are important. The independent-carrier assumption, made in the MC simulations by Bäessler *et al.*,^{1,2} is then invalid and the mobility increases with increasing carrier density, as the occupation of the deepest states by a certain fraction of the carriers reduces the effect of these states as trapping centers. For the case of a Gaussian DOS, this effect occurs for concentrations (ratio of the carrier density to the site density) larger than $c_{\text{cross-over}} = (1/2) \times \exp[-\hat{\sigma}^2/2]$.⁹ Schmechel argued that the resulting enhancement of the mobility in a Gaussian DOS could explain the mobility in disordered doped injection layers used in OLEDs, in which the carrier concentrations are very high.¹⁰ Using the results of a computational study of the T , F and n_h (hole density) dependence of the hopping mobility in a Gaussian DOS, Pasveer *et al.*¹¹ showed that the effect can provide a good quantitative explanation for the concentration dependence of the hole-mobility and the occurrence of a cross-over density; both which were discovered experimentally by Tanase *et al.*¹² for hole-only devices based on the undoped semiconducting polymer poly(*p*-phenylenevinylene) (PPV). The experimental temperature-dependent current density *versus* voltage ($J(V)$) curves of sandwich-type hole-only devices could be explained without invoking a correlation between the site energies.¹¹ At room temperature, the density dependence of the mobility was found to be much more important than the electric-field dependence. The version of the GDM presented in Ref. 11, which takes into account both the dependence of the mobility on the carrier density and the electric field, will be called the Extended Gaussian Disorder Model (EGDM).

Coehoorn *et al.*⁹ showed that the carrier-density and temperature dependence of the mobil-

ity obtained from the numerically exact Master-Equation approach in Ref. 11 is consistent with the results obtained from various existing semi-analytical models for transport in disordered materials,^{8,13,14} and that in other models^{15,16} a simple but important correction (to more properly take into account the percolative nature of the transport) is sufficient. The similarity of these models was explained by their common notion of critical hops on a percolating path that determine the size of the current. A mean-medium approximation which neglects this notion^{17,18} was shown to yield an incorrect temperature dependence of the mobility.⁹

In the EGDM, the effect of Coulomb interactions was neglected, because those interactions could not be taken into account in a consistent manner in the Master-Equation approach, since this approach involves the time-averaged and not the actual occupational probabilities of the sites. For a bulk organic semiconductor, these effects have recently been investigated using MC simulations by Zhou *et al.*¹⁹ Very important effects were found at a rather large electric field and high carrier densities ($> 10^{-2}$ carriers per site), where Coulomb interactions were found to decrease the mobility at low disorder strengths but to increase the mobility at high disorder strengths.

Another reason to prefer Monte-Carlo (MC) simulations over Master-Equation calculations is that correlations between occupational probabilities of sites are not taken into account in the Master-Equation approach. Cottaar *et al.*²⁰ showed that the effect of correlations between the occupational probabilities of pairs of neighboring sites on the current is very small. However, the effects of correlations beyond nearest-neighbor correlations were not studied.

In this chapter we investigate the effects of Coulomb interactions on the charge-carrier mobility in organic semiconducting materials. We show that taking into account Coulomb interactions in general does not lead to a significant change in the charge-carrier mobility, except for low field strengths and high carrier densities ($n > 10^{-2}a^{-3}$). In this regime, the mobility is significantly decreased by the Coulomb interactions.

This chapter is built up as follows. In Section 3.2 the simulation details are discussed. In Section 3.3 we present the results of the MC simulations. In Section 3.4 we discuss the difference between the mobility when Coulomb interactions are taken into account and when these interactions are not taken into account. Section 3.5 contains a summary and conclusions.

3.2 Monte-Carlo method

In this section we describe the simulation details for calculating the mobility in a disordered organic semiconductor. The material is modeled as a simple cubic lattice of $L_x \times L_y \times L_z$ sites, with L_x, L_y , and L_z the size of the lattice in the x -, y - and z -direction. Periodic

boundary conditions are taken. The inter-site distance is given by a . The electric field is directed in the x -direction. We assume that transport of charge carriers takes place by hopping of charges from one site to another, as a result of a tunneling process that is thermally assisted due to the coupling to a system of acoustical phonons. The hopping rate from site \mathbf{i} to \mathbf{j} is then of the Miller-Abrahams form:²¹

$$\begin{aligned} W_{\mathbf{ij}} &= \nu_0 \exp \left[-2\alpha |\mathbf{R}_{\mathbf{ij}}| - \frac{E_{\mathbf{j}} - E_{\mathbf{i}} - eFR_{\mathbf{ij},x}}{k_{\text{B}}T} \right], & E_{\mathbf{j}} &\geq E_{\mathbf{i}} + eFR_{\mathbf{ij},x}, & (3.1) \\ W_{\mathbf{ij}} &= \nu_0 \exp [-2\alpha |\mathbf{R}_{\mathbf{ij}}|] & , & E_{\mathbf{j}} < E_{\mathbf{i}} + eFR_{\mathbf{ij},x}, \end{aligned}$$

with ν_0 is an intrinsic rate, $|\mathbf{R}_{\mathbf{ij}}| \equiv a|\mathbf{i} - \mathbf{j}|$ the distance between sites \mathbf{i} and \mathbf{j} , α the inverse localization length of the localized wave functions, $E_{\mathbf{i}}$ the on-site energy of site \mathbf{i} , e the unit charge, and $eFR_{\mathbf{ij},x} \equiv eFa(j_x - i_x)$ a contribution due to an applied field. The on-site energy $E_{\mathbf{i}}$ is the sum of the random on-site energy contribution $E_{\text{rand},\mathbf{i}}$ and the Coulomb interaction energy $e\Phi_{\mathbf{i}}$ due to the surrounding charges.

We only consider the situation of uncorrelated Gaussian disorder. The energies $E_{\text{rand},\mathbf{i}}$ are then randomly drawn from a Gaussian density of states (DOS):

$$g(E) = \frac{1}{\sqrt{2\pi}\sigma a^3} \exp \left[-\frac{E^2}{2\sigma^2} \right], \quad (3.2)$$

with σ the width of this DOS.

The algorithm that is used to calculate the mobility is described in Chapter 2.2. We took averages over time and over different disorder configurations until the relative accuracy of the resulting mobilities is around 10%

3.3 Influence of Coulomb interactions on mobility

In **Fig. 3.1** we display the room-temperature mobility μ as a function of the electric field F , as obtained from the MC simulations described in the previous section. Closed symbols denote results of MC simulations in which the Coulomb interactions are taken into account. Open symbols denote results of MC simulations in which the Coulomb interactions are not taken into account. The results are given for three different disorder strengths, σ , equal to 2 (**Fig. 3.1(a)**), 4 (**Fig. 3.1(b)**), and $6k_{\text{B}}T$ (**Fig. 3.1(c)**). The mobility has been calculated for three different charge-carrier densities, $n = 10^{-3}$, 10^{-2} , and $10^{-1} a^{-3}$. The relative dielectric constant ϵ_r is taken equal to 4, like in Ref. 19. We have chosen the lattice constant equal to $a = 1.0$ nm (no value for the lattice constant was given in Ref. 19). The box size is $100 \times 100 \times 100$ sites, which corresponds with $100 \times 100 \times 100$ nm³. The mobilities are expressed in units of $\mu_0 = (a^2\nu_0e)/(\sigma)$, like in Ref. 11. Like in Ref. 11

we take the wave-function decay length, α^{-1} , equal to $a/10$. The values for the Coulomb cut-off radius were $R_c = 12, 8,$ and 5 , for $n = 10^{-3}, 10^{-2},$ and $10^{-1} a^{-3}$, respectively.

For low electric field strengths ($F < \sigma/(ea)$ for $\sigma = 2k_B T$ and $F < 0.5\sigma/(ea)$ for $\sigma = 4$ and $6k_B T$), the results from the MC simulations with Coulomb interactions are lower than the results from simulations without Coulomb interactions. The difference between the results for the case with Coulomb interactions and for the case without Coulomb interactions attains its maximum in the zero-field limit. The difference is a factor of about 1.8 for a carrier density of $n = 10^{-1} a^{-3}$ and disorder strength $\sigma = 6k_B T$ and increases to a factor of about 2.5 for the same density and $\sigma = 2k_B T$. The difference is a factor of about 1.4 for $n = 10^{-2} a^{-3}$ and a factor of about 1.2 for $n = 10^{-3} a^{-3}$ for all disorder strengths. For higher electric field strengths than mentioned above, the results from simulations with Coulomb interactions agree in general quite well with the results from simulations without Coulomb interactions.

3.4 Discussion

To tentatively explain the decrease in the mobility for high carrier densities when Coulomb interactions are taken into account, we note that these interactions will lead to a mutual repulsion of the charges. As a result, charges are trapped in a Coulomb potential well formed by other surrounding charges. As the average distance between the charges becomes smaller with higher carrier density, the Coulomb potential well becomes steeper. To hop from the minimum of a potential well to a neighboring site, on average a higher energy penalty is involved than in a situation without Coulomb interactions. This in turn leads to a decrease in the mobility.

With increasing electric field, more and more hops in the direction of the field will be downwards in energy. When a hop is downwards in energy, the hopping rate, as described by Eq. 3.1, does not depend on the involved Coulomb energies. Hence, the effect of the existence of a Coulomb potential well becomes less important with increasing field. In the case of very high electric field strengths, when practically all hops are downwards in energy, the effect of a Coulomb potential well vanishes. In this case, the inclusion of Coulomb interactions does not lead to a significant change in the mobility.

One could be tempted to attribute the effect of the reduction of the mobility with inclusions of Coulomb interactions to the enhancement of the effective disorder due to the random Coulomb field. The effective disorder σ_{eff} would be obtained by calculating the standard deviation of all on-site energies, consisting of a random on-site contribution and the Coulomb interaction energy of all charges. Instead of taking the random on-site energies from a Gaussian distribution with a width equal to σ and taking the Coulomb interactions explicitly into account, one could then take these energies from a Gaussian distribution with a width equal to the effective disorder strength σ_{eff} and omit the Coulomb

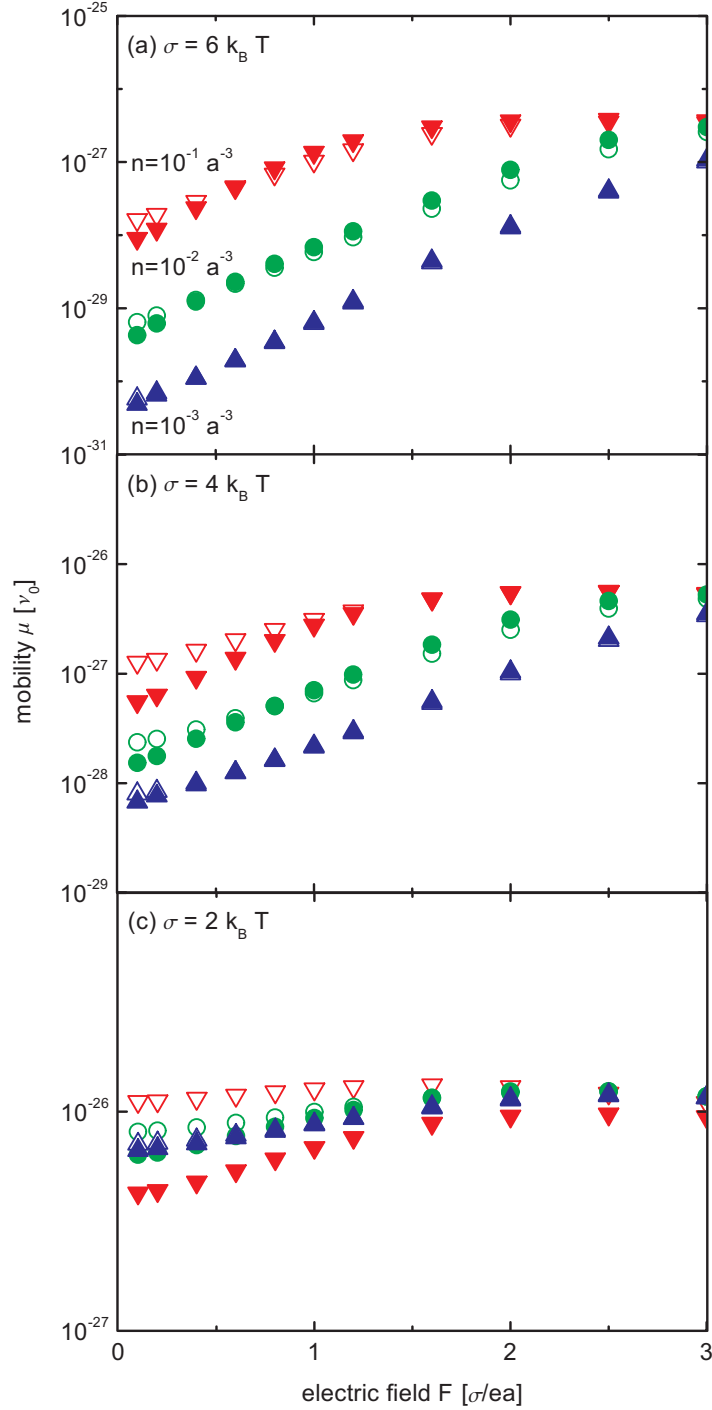


Figure 3.1: Dependence of the room-temperature mobility (μ) on the applied electric field (F) for an uncorrelated Gaussian density of states. The lattice constant is $a = 1.0$ nm. The displayed results are for disorder strengths of $\sigma = 6k_B T$ (a), $\sigma = 4k_B T$ (b), and $\sigma = 2k_B T$ (c). Results are shown for different indicated carrier densities n : $10^{-1}a^{-3}$ (downwards pointing triangles), $10^{-2}a^{-3}$ (circles), and $10^{-3}a^{-3}$ (upwards pointing triangles). The mobility is expressed in units of $\mu_0 = a^2\nu_0e/\sigma$. Closed symbols: results obtained from Monte-Carlo simulations including short-range Coulomb interactions. Open symbols: results obtained from Monte-Carlo simulations without Coulomb interactions.

interactions. This could possibly be done along the lines set out by Arkhipov *et al.*,²² who calculated the increase of the effective disorder strength due to Coulomb interactions with dopant ions.

However, it turns out that an effective disorder strength defined in this way would diverge when R_c goes to infinity. This can be shown by the following analytical argument. Assume a disorder-free system ($\sigma = 0$) and a random distribution of the charges over the system, with a carrier density equal to n . The mean $\langle V \rangle$ and the standard deviation $\sqrt{\langle V^2 \rangle - \langle V \rangle^2}$ of the Coulomb interaction energy are then given by:

$$\langle V \rangle = \int \int \int dr d\theta d\phi n \sin(\theta) \frac{e^2}{4\pi\epsilon_r\epsilon_0} \left[\frac{r^2}{r} - \frac{r^2}{R_c} \right] \quad (3.3)$$

$$= \frac{e^2}{4\pi\epsilon_r\epsilon_0} \frac{2}{3} \pi n R_c^2, \quad (3.4)$$

$$\langle V^2 \rangle - \langle V \rangle^2 = \int \int \int dr d\theta d\phi n \sin(\theta) r^2 \frac{e^2}{4\pi\epsilon_r\epsilon_0} \left(\frac{1}{r} - \frac{1}{R_c} \right)^2 - \langle V \rangle^2 \quad (3.5)$$

$$= \frac{e^2}{3\pi\epsilon_r\epsilon_0} \pi n R_c \left(1 - \frac{1}{3} \pi n R_c^3 \right), \quad (3.6)$$

$$\sqrt{\langle V^2 \rangle - \langle V \rangle^2} = \sqrt{\frac{e^2}{3\pi\epsilon_r\epsilon_0} \pi n R_c \left(1 - \frac{1}{3} \pi n R_c^3 \right)} \quad (3.7)$$

Therefore, for not too high carrier densities, the standard deviation of the Coulomb interaction energy is proportional to $\sqrt{R_c}$ and thus diverges for $\sqrt{R_c} \rightarrow \infty$. As a consequence, an effective disorder strength obtained by adding to the random energy of the sites the random Coulomb energies due to all charges is ill-defined and can therefore not be used to model the reduction of the mobility.

3.5 Summary and conclusions

We performed Monte-Carlo simulations on the charge-carrier transport in a bulk organic semiconductor. The site energies are distributed according to a Gaussian density of states. Coulomb interactions are taken into account. The dependence of the mobility on the charge carrier density and the electric field strength were studied.

The calculations show, contrary to earlier calculations performed by Zhou *et al.*,¹⁹ that taking the Coulomb interactions into account does not change the mobility significantly in the case of high electric field strengths. In this regime the EGDM is thus still applicable, even in the presence of Coulomb interactions.

In the regime of low electric field strengths and high carrier densities ($n > 10^{-2} \text{ a}^{-3}$), a

significant decrease in the mobility is obtained when Coulomb interactions are taken into account. This decrease is stronger for higher carrier densities. We tentatively explain this by the trapping of charges in the Coulomb potential well formed by the surrounding charges. In the hopping of a charge from the minimum of a potential well to a neighboring site, this potential well leads to an extra energy penalty. This results in a lower mobility. This trapping effect decreases for higher electric field strengths.

We conclude that Coulomb interactions only have a strong effect on the mobility in the case of small electric field strengths and high carrier densities. In this regime the mobility is decreased significantly by the Coulomb interactions.

References

- [1] Pautmeier, L.; Richert, R.; Bäessler, H. *Synth. Met.* **1990**, *37*, 271.
- [2] Bäessler, H. *Phys. Stat. Sol. (b)* **1993**, *175*, 15.
- [3] Gartstein, Y.; Conwell, E. *Chem. Phys. Lett.* **1995**, *245*, 351.
- [4] Dunlap, D.; Parris, P.; Kenkre, V. *Phys. Rev. Lett.* **1996**, *77*, 542.
- [5] Novikov, S.; Dunlap, D.; Kenkre, V.; Parris, P.; Vannikov, A. *Phys. Rev. Lett.* **1998**, *81*, 4472.
- [6] Yu, Z.; Smith, D.; Saxena, A.; Martin, R.; Bishop, A. *Phys. Rev. Lett.* **2000**, *84*, 721.
- [7] Monroe, D. *Phys. Rev. Lett.* **1985**, *54*, 146.
- [8] Vissenberg, M.; Matters, M. *Phys. Rev. B* **1998**, *57*, 12964.
- [9] Coehoorn, R.; Pasveer, W.; Bobbert, P.; Michels, M. *Phys. Rev. B* **2005**, *72*, 155206.
- [10] Schmechel, R. *Phys. Rev. B* **2002**, *66*, 235206.
- [11] Pasveer, W.; Cottaar, J.; Tanase, C.; Coehoorn, R.; Bobbert, P.; Blom, P.; de Leeuw, D.; Michels, M. *Phys. Rev. Lett.* **2005**, *94*, 206601.
- [12] Tanase, C.; Meijer, E.; Blom, P.; de Leeuw, D. *Phys. Rev. Lett.* **2003**, *91*, 216601.
- [13] Movaghar, B.; Schirmacher, W. *J. Phys. C* **1981**, *14*, 859.
- [14] Rubel, O.; Baranovskii, S.; Thomas, P.; Yamasaki, S. *Phys. Rev. B* **2004**, *69*, 014206.
- [15] Arkhipov, V.; Heremans, P.; Emelianova, E.; Adriaenssens, G.; Bäessler, H. *J. Phys.: Condens. Matter* **2002**, *14*, 9899.

- [16] Martens, H.; Hulea, I.; Romijn, I.; Brom, H.; Pasveer, W.; Michels, M. *Phys. Rev. B* **2003**, *67*, 121203(R).
- [17] Roichman, Y.; Tessler, N. *Synth. Met.* **2003**, *135*, 443.
- [18] Roichman, Y.; Preezant, Y.; Tessler, N. *Phys. Stat. Sol. (a)* **2004**, *201*, 1246.
- [19] Zhou, J.; Zhou, Y.; Zhao, J.; Wu, C.; Ding, X.; Hou, X. *Phys. Rev. B* **2007**, *75*, 153201.
- [20] Cottaar, J.; Bobbert, P. *Phys. Rev. B* **2006**, *74*, 115204.
- [21] Miller, A.; Abrahams, E. *Phys. Rev.* **1960**, *120*, 745.
- [22] Arkhipov, V.; Heremans, P.; Emelianova, E.; Bäessler, H. *Phys. Rev. B* **2005**, *71*, 045214.

Chapter 4

Modeling and analysis of the three-dimensional current density in sandwich-type single-carrier devices of disordered organic semiconductors

ABSTRACT

We present the results of a modeling study of the three-dimensional current density in single-carrier sandwich-type devices of disordered organic semiconductors. The calculations are based on a Master-Equation approach, assuming a Gaussian distribution of site energies without spatial correlations. The effects of space charge, image charge potential, injection barrier, and the full dependence of the mobility on the charge carrier density, electric field, and temperature are taken into account. The model provides a comprehensive treatment of the space-charge-limited current (SCLC) as well as the injection-limited current (ILC) regimes. Reasonable agreement is found between the three-dimensional Master-Equation calculation results and a one-dimensional continuum drift-diffusion model. This one-dimensional drift-diffusion model uses the EGDM mobility functions. The injection-barrier lowering due to the image potential is taken into account. However, the current distribution can be highly filamentary for voltages, layer thicknesses, and disorder strengths that are realistic for organic light-emitting diodes. As a result, the current density as obtained from the Master-Equation calculations can be significantly larger than that obtained from a one-dimensional continuum drift-diffusion device model, specifically in the case of strong disorder, high voltages and high injection barriers. For devices with large injection barriers and strong disorder, in the ILC transport

regime, good agreement is obtained with the average current density predicted from a model assuming injection and transport via one-dimensional filaments.¹

¹The contents of this chapter are based on work that has been published: J.J.M. van der Holst, M.A. Uijtewaal, B. Ramachandhran, R. Coehoorn, P.A. Bobbert, G.A. de Wijs, R.A. de Groot, *Physical Review B: Condensed Matter* **2009**, 79, 085203

4.1 Introduction

Organic semiconductors are presently used in a wide variety of devices, such as organic light-emitting diodes (OLEDs),¹ organic field-effect transistors,² and organic photovoltaic cells.³ In these materials, which are often amorphous or near-amorphous, an important role is played by disorder: it contributes to the localization of electronic states, and strongly influences the hopping rates of the charge carriers between the localized states. Our understanding of devices based on disordered organic semiconductors within which hopping conduction takes place is far less developed than our understanding of transport in devices based on crystalline inorganic semiconductors.

In this chapter, we investigate the effects of disorder on the transport through complete single-carrier single-layer devices. It is already well-known that the percolative nature of the transport in a disordered organic semiconductor leads to a strongly filamentary structure of the current along the percolation paths.⁴⁻⁸ This raises the question to what extent one-dimensional (1D) continuum drift-diffusion device models, within which the current density is assumed to be laterally uniform, provide accurate predictions of the $J(V)$ curves. It is important to answer this question because such 1D models are numerically much more efficient than complete three-dimensional device models, and are the obvious choice in modeling the complex multilayer structures that will be used in commercial OLEDs. We address this question by making a detailed comparison between the current densities obtained from a full three-dimensional (3D) Master-Equation model for the hopping transport in single-layer single-carrier sandwich-type devices and the current densities obtained from a 1D continuum drift-diffusion device model. The 1D model that we will use is based on the Extended Gaussian Disorder Model (EGDM). It is an extension of an approach introduced in Ref. 9 to include the effective injection-barrier lowering due to the image-potential effect. Earlier work on PPV-based polymers revealed no necessity to take correlated disorder into account,¹⁰ such as is done in the work of Tutiš *et al.*⁴ These authors used a Master-Equation model for calculating the current density in the case of correlated disorder for the situation that the current is limited by injection, taking the image potential into account but neglecting space-charge effects.

We show that the 1D continuum model provides for various cases of interest quite accurate predictions of the voltage dependence of the current density. However, we also find a distinct offset of the current for relatively large disorder ($\hat{\sigma} = 6$) and a small layer thickness (22 nm). The filamentarity of the current density is then quite pronounced. We present visualizations of the three-dimensional current density and discuss the effects of the filamentary nature of the current density in the case of strong disorder on the current density in the space-charge-limited current (SCLC) and injection-limited current (ILC) transport regimes. Our 3D model will allow us to analyze the appropriateness of various previously proposed models for charge-carrier injection in OLEDs. We will now give an overview of existing models of injection and transport in single-carrier single-layer devices.

Within the simplest approach to the problem of carrier injection and subsequent transport in organic semiconductor devices it is assumed that the charge carriers in the organic semiconductor at the contact are in thermal equilibrium with the electrons in the metal electrode. The presence of an injection barrier, Δ , then reduces the density of carriers at the contact with the metal, n_c , to a value given by $n_c = N_t/(1 + \exp[\Delta/k_B T])$, with N_t the total density of molecular sites. Here, Δ is defined as the (positive) energy difference between the Fermi energy in the metal and the energy of the HOMO or LUMO states in the semiconductor. The current density is obtained by self-consistently solving the drift-diffusion equation, taking the space-charge in the device into account and using n_c as a fixed boundary condition. For the case of a constant mobility and diffusion coefficient, this boundary value problem can be solved analytically.¹¹ In a symmetric device (equal left and right contacts) the current density is then injection-limited if $n_c \approx n_0 \equiv \epsilon k_B T/(e^2 L^2)$, or smaller, with ϵ the dielectric constant, e the elementary charge, and L the device thickness. For $L = 100$ nm, $N_t = 10^{27}$ m⁻³, and a relative dielectric constant $\epsilon_r = 3$ (a typical device), the injection-limited transport regime therefore sets in (at room temperature) around $\Delta \approx 0.4$ eV. For larger injection barriers, the space charge in the device can be neglected, and the carrier density is uniform and equal to n_c . The injection-limited current density is then given by $J_{\text{ILC}} = en_c \mu V/L$.

For two reasons the problem of carrier injection in organic semiconductors is more complicated than assumed in the model discussed above. First, the model neglects the image-charge interaction between an individual charge and its image charge in the electrode. In the SCLC regime, the image-charge effect is to a certain extent taken into account by self-consistently solving the Poisson equation for the *layer-averaged* charge density. In that regime, the resulting error is small. However, in the ILC regime the *actual* injected charge at a specific site associated with one carrier is one electronic charge at that site, which is much larger than the layer-averaged charge at sites in the same layer. The effect of the image potential on the current density in the ILC regime has been studied by Emtage and O'Dwyer,¹² and more recently by Scott and Malliaras¹³ and by Masenelli *et al.*¹⁴ Effectively, it leads to a lowering of the effective injection barrier with increasing voltage.

Second, all models discussed so far neglect the effects of energetic disorder. Its relevance to the injection process in OLED-type devices was first noted by Gartstein and Conwell, who studied the combined effects of the image potential and the Gaussian disorder in the ILC regime, using a MC simulation.¹⁵ These authors showed that disorder can give rise to a strongly enhanced field dependence of the injection-limited current density. Arkhipov *et al.* developed a semi-analytical 1D approach to this problem.¹⁶ For relatively high temperatures and small disorder good agreement was found with the results of MC calculations.¹⁷ As a result of the injection in tail states, the ILC in a material with a Gaussian DOS was predicted to be larger than the ILC in an ordered material, for a given value of Δ , and its decrease with decreasing temperature was predicted to be smaller. The latter effect was confirmed by van Woudenberg *et al.* from an experimental study of the ILC in PPV-based devices.¹⁸ Burin and Ratner (BR) studied this problem by assuming that for sufficiently

high field strengths and in the ILC regime the injection and transport occurs through 1D straight paths, effectively lowering the injection barrier.¹⁹ Recently, support for the latter model has been obtained from a measurement using electric-force microscopy of the potential drop near the injecting contacts in a lateral two-terminal metal/organic/metal device.²⁰ As noted already by the authors,¹⁷ it is expected that the Arkhipov model underestimates the stochastic nature of the carrier motion in the vicinity of the barrier, when at high fields only a few rare easy pathways dominate the current density. On the other hand, the BR model will overrate this effect, in particular for relatively small fields when more easy non-linear trajectories are neglected. These weaknesses of the Arkhipov and BR models are confirmed by the 3D modeling results presented in this chapter.

This chapter is built up as follows. Sections 4.2.1 and 4.2.2 discuss the 3D Master-Equation method and the 1D continuum model, respectively, used for calculating the current density in single-carrier devices. In Section 4.3 we present the results of the 3D Master-Equation and 1D continuum modeling of the voltage dependence of the current density. In Section 4.4 we investigate the 3D structure of the current distribution and discuss the consequences of this structure for the validity of different models: our 1D continuum model, the BR model, and the Arkhipov model. Section 4.5 contains a summary and conclusions.

4.2 Theory and methods

4.2.1 Three-dimensional Master-Equation model

In this section the 3D Master-Equation method is described for calculating the current density in single-carrier devices, consisting of a single organic layer that is sandwiched in between two metallic electrode layers. The device is modeled as a three-dimensional cubic $L_x \times L_y \times L_z$ lattice with an inter-site distance a . Lattice sites will be denoted by $\mathbf{i} \equiv \{i_x, i_y, i_z\}$. The applied field is directed along the x -axis, and the planes formed by the sites at $i_x = 1$ and $i_x = L_x$ are viewed as the metallic injecting and collecting electrode planes, respectively. The sites at all other planes will be called “organic sites”. Along the lateral (y and z) directions periodic boundary conditions are applied. Every site represents a localized state and the carrier occupation probability on a site \mathbf{i} will be denoted by $p_{\mathbf{i}}$.

We assume that conduction in the organic semiconductor takes place by hopping of charge carriers from one localized site to another, as a result of a tunneling process that is thermally assisted due to the coupling to a system of acoustical phonons. This leads to a hopping rate from site \mathbf{i} to \mathbf{j} of the Miller-Abrahams form²¹

$$W_{\mathbf{ij}} = \nu_0 \exp \left[-2\alpha |R_{\mathbf{ij}}| - \frac{E_{\mathbf{j}} - E_{\mathbf{i}}}{k_{\text{B}}T} \right] \quad \text{for } E_{\mathbf{j}} \geq E_{\mathbf{i}}, \quad (4.1a)$$

$$W_{\mathbf{ij}} = \nu_0 \exp [-2\alpha |R_{\mathbf{ij}}|] \quad \text{for } E_{\mathbf{j}} < E_{\mathbf{i}}, \quad (4.1b)$$

where ν_0 is an intrinsic rate, $|R_{ij}| \equiv a|\mathbf{i} - \mathbf{j}|$ is the distance between sites \mathbf{i} and \mathbf{j} , α is the inverse localization length of the localized wave functions, and E_i is the energy of the state at site \mathbf{i} . For simplicity, we assume that the hopping rates from the electrode sites to the organic sites and *vice versa* are given by the same expression (Eq. (4.1)) as the rates for the mutual hopping between organic sites. It is to be expected that the specific rate taken for the hopping between the electrode sites and the sites in the first and last organic layer has almost no influence on the final current-voltage characteristics of the device, as long as this hopping rate is large enough to establish equilibrium between these sites.

Only symmetric devices are considered in this chapter, i.e. devices with equal injection barriers, Δ , at the injecting and collecting electrodes, but our methods can just as well be applied to asymmetric devices. The injection barrier is defined as the distance in energy between the Fermi level in the electrode and the top of the Gaussian DOS. The energy of each organic site is therefore equal to the sum of a random on-site contribution, drawn from a Gaussian DOS with a width equal to σ , and an offset due to the injection barrier,

$$g(E) = \frac{1}{\sqrt{2\pi}\sigma a^3} \exp\left[-\frac{(E - \Delta)^2}{2\sigma^2}\right], \quad (4.2)$$

plus the electrostatic energy contributions $e\Phi_i$ and $e\Phi_{\text{im},i}$ due to the applied field and the space charge, and due to the image-charge effect, respectively. The Fermi energy in the collecting electrode is taken as the zero-energy reference value, so that the electrostatic potentials at the two electrode planes are given by $e\Phi(i_x = 1) = eV$ and $e\Phi(i_x = L_x) = 0$, where V is the applied driving voltage (bias). The contribution to the electrostatic potential due to the space charge is calculated using the Poisson equation from the laterally averaged charge-carrier density in each layer i_x . As a consequence of this approximation, $e\Phi_i$ depends only on the layer index i_x . Also the image-charge contribution depends only on the distance of the site to each of the electrodes. It is given by

$$e\Phi_{\text{im}}(i_x) = -\frac{e^2}{16\pi\epsilon_0\epsilon_r a} \left(\frac{1}{L_x - i_x} + \frac{1}{i_x - 1} \right) \quad (4.3)$$

at the organic sites. Here e is the unit charge, ϵ_0 the vacuum permeability, and ϵ_r the relative dielectric constant of the organic material. There is no image-charge contribution at the electrode sites. Eq. (4.3) is the first-order term in an expansion in which repetitive images are taken into account.²² For the device thicknesses considered, no significant change of the results was obtained when taking higher-order images into account.

The occupational probabilities p_i for the organic sites are obtained by solving the Pauli master equation

$$\begin{aligned} \frac{\partial p_i}{\partial t} &= - \sum_{\mathbf{j} \neq \mathbf{i}, j_x \neq 1, L_x} [W_{ij}p_i(1 - p_j) - W_{ji}p_j(1 - p_i)] \\ &\quad - \sum_{\mathbf{j} \neq \mathbf{i}, j_x = 1, L_x} [W_{ij}p_i - W_{ji}(1 - p_i)] \\ &= 0 \quad , \end{aligned} \quad (4.4)$$

where the first sum is related to hopping between organic sites and the last term to hopping from and to the electrodes. The factors $1 - p_i$ in this first sum account, in a mean-field approximation, for the fact that only one carrier can occupy a site, due to the high Coulomb penalty for the presence of two or more carriers. The second sum describes the hopping from sites of the outermost organic layers to the electrode sites (first term between square brackets) and the hopping from electrode sites to the outermost organic layers (second term), where we assume that there are always charges on the electrode sites ready to hop to the organic sites and that the electrode sites can always accept a charge from the organic sites. We take into account hopping over a maximum distance of $\sqrt{3}a$, which is sufficient for the values of a and α that we will consider (see Section 4.3).

In order to solve the Pauli master equation for the occupational probabilities p_i , we use an iterative procedure similar to the one described in Refs. 8 and 10. From these occupational probabilities we can calculate the current through the device. At each organic site \mathbf{i} , we define a local particle current $J_{p,\mathbf{i}}$ in the direction of the collecting electrode:

$$J_{p,\mathbf{i}} = \sum \{W_{\mathbf{ij}}p_i(1 - p_j) - W_{\mathbf{ji}}p_j(1 - p_i)\}, \quad (4.5)$$

where the summation is over all sites \mathbf{j} for which $j_x > i_x$. The total electrical current density is then given by

$$J = \frac{1}{L_y L_z} \sum \frac{eJ_{p,\mathbf{i}}}{a^2}, \quad (4.6)$$

where the summation is over all $L_y \times L_z$ sites within any plane parallel to the electrodes within the device.

As the electrostatic potential is determined by the charge distribution, whereas the charge distribution can only be calculated if the potential is known, both should be determined self-consistently. To obtain the self-consistent solution we use the following iteration procedure:

1. Start with a potential Φ that linearly decreases from injecting to collecting electrode.
2. Solve the master equation, Eq. (4.4).
3. Update the electrostatic potential, which has changed due to the change of the space charge.
4. Recalculate all the hopping rates $W_{\mathbf{ij}}$, using Eq. (4.1).

If the total charge and the current in the device have converged the procedure stops, otherwise the procedure starts again at the second step.

4.2.2 One-dimensional continuum model

We will compare the $J(V)$ curves obtained from the 3D Master-Equation model discussed in the previous subsection to the $J(V)$ curves obtained from a 1D continuum drift-diffusion model. The current density in this model is given by

$$J = n(x)e\mu(x)F(x) - eD(x)\frac{dn(x)}{dx}, \quad (4.7)$$

where $n(x)$ and $F(x)$ are the local charge-carrier density and electric field, respectively, which are related by the Poisson equation, $dF/dx = (e/\epsilon)n(x)$. The dependence of the local mobility, $\mu(x) = \mu(T, n(x), F(x))$, on the temperature, the charge-carrier density, and the electric field is taken from the parametrization given for the EGDM in Ref. 10. The local diffusion coefficient, $D(x)$, is obtained from the local mobility by using the generalized Einstein equation.²³ We note that the expressions given in Ref. 10 for the mobility within the EGDM were obtained from essentially the same 3D Master-Equation model as discussed above, but then for a system with a uniform carrier density and electric field, and including also periodic boundary conditions along the x -direction. Therefore, any difference between both approaches will be exclusively due to a failure of taking the actual non-uniform 3D current density into account in the 1D model.

For efficiently solving the 1D drift-diffusion-Poisson problem within the EGDM, we have used an extended version of the numerical method described recently by Van Mensfoort and Coehoorn.⁹ Within the standard form of that method, described in Ref. 9, the carrier densities at the electrode planes are assumed to be constant (voltage independent), and given by the condition of local thermal equilibrium between the metal and the organic layer. The density of carriers at the contact with the metal, n_c , is then given by

$$n_c = \int_{-\infty}^{\infty} \frac{g(E)}{1 + \exp\left[\frac{E}{k_B T}\right]} dE, \quad (4.8)$$

with the DOS $g(E)$ given by Eq. (4.2). When the injection barrier is sufficiently small, the large carrier density in the organic layer near the injecting electrode will give rise to a local drift contribution of the particle current towards the injecting electrode. Under these conditions, the electrostatic field near the interfaces is the result of a net electrostatic interaction that is the overall sum of the individual contributions from the charges and image charges of many electrons. The standard 1D model treats this in a fair way, *viz.* by solving the 1D Poisson equation assuming a laterally homogeneous charge density. On the other hand, when the injection barrier is sufficiently large, so that the local drift contribution to the particle current is directed away from the injecting electrode, the predominant contribution to the electrostatic field near the electrode is due to the image charge of the injected carrier itself. In order to be able to account for such cases, we have extended the 1D model presented in Ref. 9 by making use of an image-charge-corrected barrier height

of the form first suggested by Emtage and O'Dwyer,¹²

$$\Delta' = \Delta - e\sqrt{\frac{eF_c}{4\pi\epsilon_0\epsilon_r}}, \quad (4.9)$$

with F_c the (positive) electric field at the contact plane. F_c and Δ' are determined self-consistently using an iterative procedure. When $F_c < 0$, the full injection barrier Δ is used. We show in Section 4.3 that this method of taking the image-charge potential into account in 1D calculations of $J(V)$ curves leads to a surprisingly good agreement with the results of the 3D Master-Equation model, provided that the transport is well in the ILC regime.

4.3 Results

In **Fig. 4.1** we display the room-temperature current density as a function of applied voltage, as obtained from the 3D and 1D calculations described in the previous section. The results are given for different injection barriers, Δ , equal to 0, 0.33, 0.67, and 1 eV. The lattice constant has been taken equal to $a = 1.6$ nm, a value found in Ref. 10 from modeling the transport in a hole-only device based on the PPV derivative OC₁C₁₀-PPV (poly[2-methoxy-5-(3',7'-dimethyloctyloxy)-*p*-phenylene vinylene]). The four plots show the results for two values of the dimensionless disorder parameter, $\hat{\sigma} = 3$ and 6, corresponding to $\sigma = 75$ meV and $\sigma = 150$ meV at room temperature, respectively, and for two layer thicknesses L , indicated in the figures as “22 nm” and “102 nm”. The actual thicknesses are 13 layers (22.4 nm) and 63 layers (102.4 nm), respectively. The attempt-to-jump frequency, ν_0 , is chosen such that at vanishing injection barrier, the current density as obtained from the 3D model is equal to 1 A/m² at $V = 10$ V for the 102 nm devices. This value of ν_0 , and the corresponding values of the mobility at zero field in the low-density Boltzmann limit used within the 1D-model calculations, are given in the figure caption and will be used throughout the rest of the chapter. Like in Ref. 10, we take the wavefunction decay length, α^{-1} , equal to $a/10$. The lateral grid size is 50×50 sites. The relative accuracy of the results is approximately 10 %, which was concluded by carrying out calculations for different lateral grid sizes and disorder realizations.

A remarkably good agreement is obtained between the 3D Master-Equation results (symbols) and the 1D continuum-model results (lines), except for the thin ($L = 22$ nm) device with strong disorder ($\sigma = 150$ meV) at voltages exceeding 1 V (**Fig. 4.1d**). For the lowest injection barriers, $\Delta = 0$ and 0.33 eV, the devices are in the space-charged-limited current (SCLC) regime and the current is almost independent of the size of the injection barrier. At small voltages, the current-voltage curves are linear (Ohmic), as expected when the transport is predominantly due to charge-carrier diffusion.⁹ The slope of the current-voltage curve (on a double-log scale) increases with increasing voltage, eventually to a value that exceeds the value of two that would be obtained for the case of a constant mobility in the

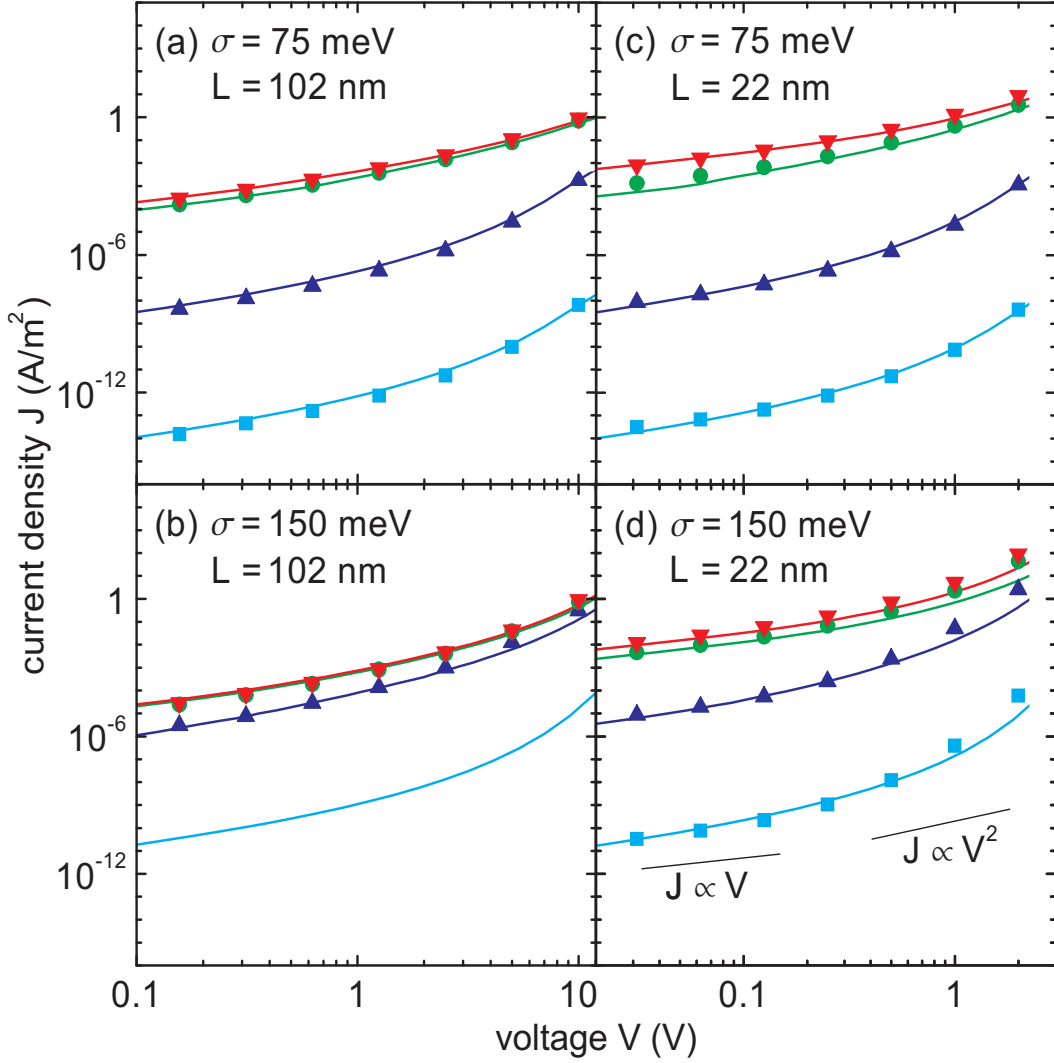


Figure 4.1: Dependence of the current density (J) on the driving voltage (V) for devices with thicknesses of $L = 102$ nm and $L = 22$ nm, and disorder strengths of $\sigma = 75$ meV and $\sigma = 150$ meV, as indicated in (a)-(d). The results are for room temperature and lattice constant $a = 1.6$ nm. The values used for the attempt-to-jump frequency, ν_0 , are $3.5 \times 10^{13} \text{ s}^{-1}$ for devices with $\sigma = 75$ meV and $1.4 \times 10^{16} \text{ s}^{-1}$ for devices with $\sigma = 150$ meV. These values correspond to a mobility pre-factor μ_0 (as defined in Ref. 10) equal to $4.8 \times 10^{-14} \text{ m}^2/\text{Vs}$ and $1.1 \times 10^{-16} \text{ m}^2/\text{Vs}$, respectively. Symbols: results obtained from the 3D Master-Equation approach for different injection barriers Δ : 0 eV (downwards pointing triangles), 0.33 eV (circles), 0.67 eV (upwards pointing triangles), and 1 eV (squares). In (b) no converged Master-Equation results for $\Delta = 1$ eV could be obtained. Solid lines: results obtained from the 1D continuum drift-diffusion model as explained in the main text.

presence of a drift contribution only (Mott-Gurney relationship). This can be viewed as a result of the carrier-density dependence and the electric-field dependence of the mobility.^{9,10} When the injection barrier increases the injection-limited current (ILC) regime is entered and the voltage dependence becomes much more pronounced. For high injection barriers the current in the 22 nm and 102 nm devices is almost the same for equal injection barriers, if the voltage is scaled with the device thickness. For the case $\sigma = 75$ meV this happens for injection barriers $\Delta = 0.67$ and 1 eV. For the case $\sigma = 150$ meV, space-charge effects are still dominant at an injection barrier of $\Delta = 0.67$ eV, the reason being that a higher value of σ leads to a higher carrier density at the interface than for $\sigma = 75$ meV (the tail states of the Gaussian DOS are filled to a larger extent), and hence to stronger limitation of the current by space-charge effects. We remark that because of convergence problems we were not able to obtain Master-Equation results for $\Delta = 1$ eV for the 102 nm device.

We analyze the situation in more detail with the help of **Fig. 4.2**, which shows a comparison of the calculated injection-barrier dependent current density in the 22 nm devices at a bias of 2 V and room temperature as obtained from the 3D Master-Equation approach and as obtained from various other approaches, for $\sigma = 75$ meV (**Fig. 4.2(a)**) and $\sigma = 150$ meV (**Fig. 4.2(b)**). We first focus on the results in the SCLC regime. For very small values of Δ , the 1D calculations were carried out without taking the image-charge effect into account since the field is then directed towards the injecting electrode ($F_c < 0$ as explained in Section 4.2.2). Calculations including the image-charge effect were only carried out for $\Delta > 0.20$ eV and $\Delta > 0.35$ eV for $\sigma = 75$ and $\sigma = 150$ meV, respectively, as indicated by the arrows in **Fig. 4.2**. For these cases the inclusion of the image potential leads to an effective barrier *decrease* (Eq. (4.9)). Actually, for smaller values of Δ the inclusion of the image potential would lead to a small effective barrier *increase*, due to charge trapping in the potential well near the interface, deepened by the image potential. As a result, the actual current density would be smaller than as predicted from the 1D-model used here. One may estimate the effect by extrapolating the 1D current-density curve as obtained with the image potential to $\Delta = 0$ eV. The extrapolated current density is a factor ~ 1.5 and ~ 4.5 smaller than the 1D current density given in **Fig. 4.2** for the cases $\sigma = 75$ and $\sigma = 150$ meV, respectively. For $\sigma = 75$ meV the agreement between the 3D Master-Equation and 1D continuum-model results is very good, with an underestimation of the current density by the 1D continuum model in the SCLC regime by only a factor of about two. However, for $\sigma = 150$ meV the 1D continuum model underestimates the current density in the SCLC regime by a factor of about four. We note that the extrapolated current densities mentioned above, including the image potential, yield a stronger underestimation of the current densities in the SCLC regime. We may thus conclude that the omission of the image potential in the 1D continuum model accidentally corrects part of an intrinsic underestimation of the current density by the 1D model. In the next section, we will investigate the origin of this underestimation.

With increasing injection barrier we see in **Fig. 4.2** a transition from the SCLC to the

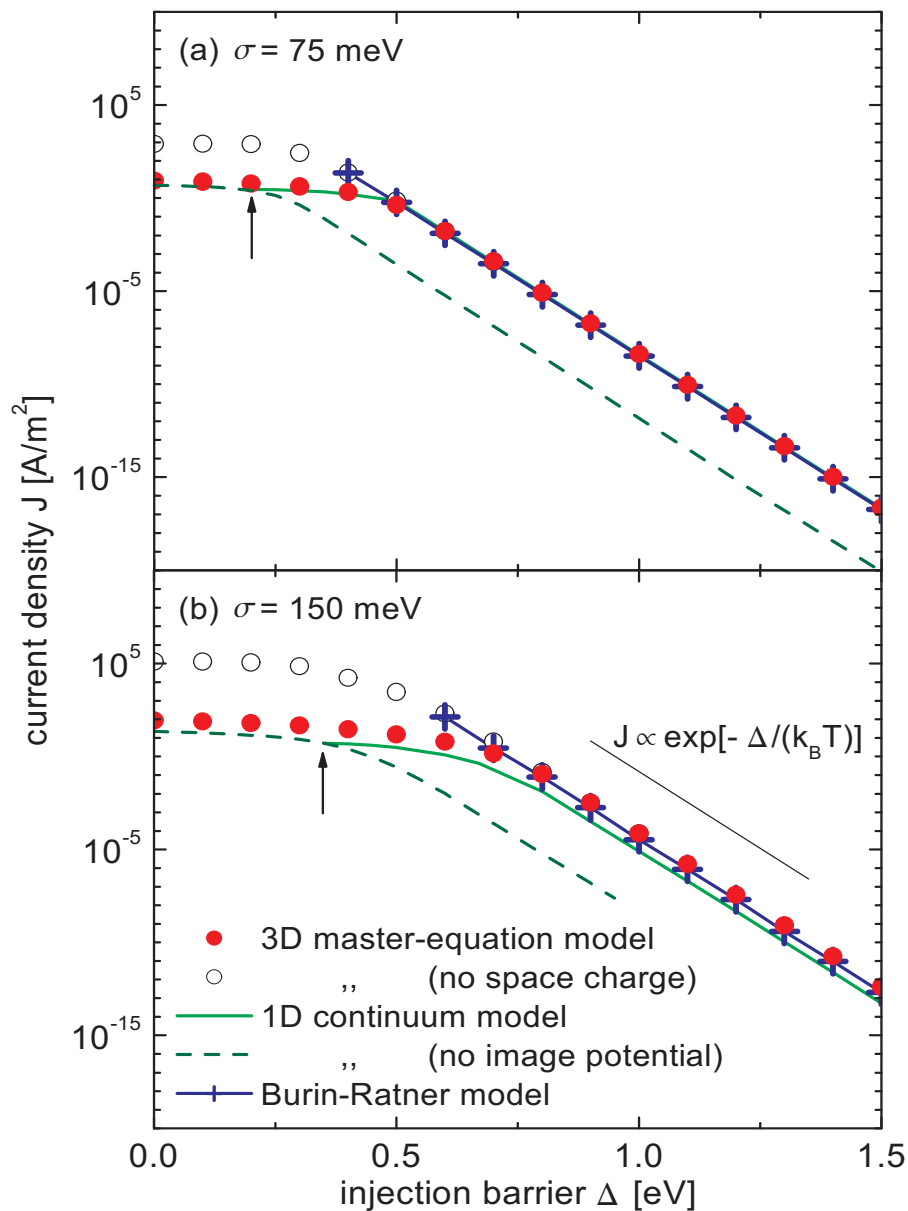


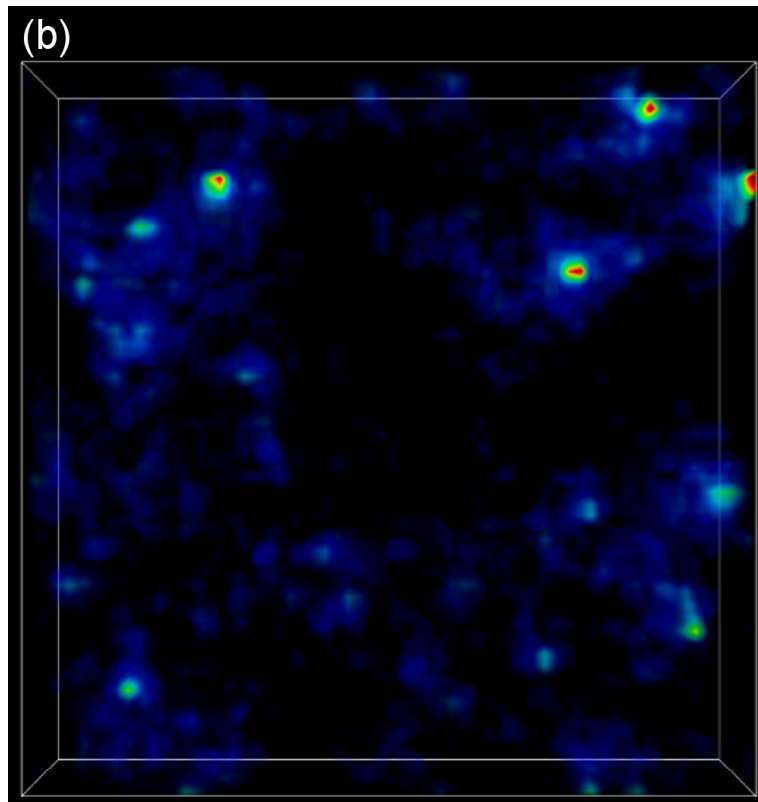
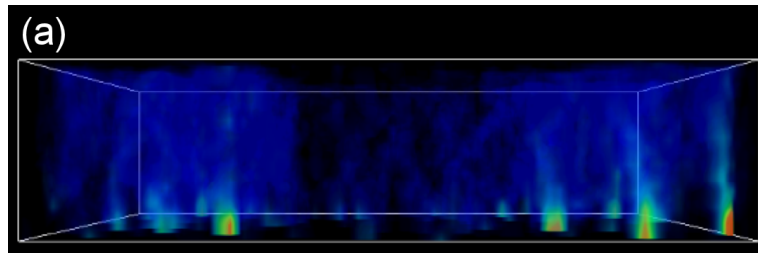
Figure 4.2: Dependence of the current density (J) on the injection barrier (Δ), for different models. The displayed results are for devices with disorder strengths of $\sigma = 75$ meV (a) and $\sigma = 150$ meV (b), device thickness $L = 22$ nm, room temperature, and lattice constant $a = 1.6$ nm. The other parameters are the same as in Fig. 4.1. The arrows indicate the points where the electric field at the injecting electrode switches sign within the 1D continuum model.

ILC regime, with finally an Arrhenius behavior, $J \propto \exp[-\Delta/k_B T]$ of the current density. In the ILC regime the inclusion of the image potential is of crucial importance, which can be seen from the continuation of the 1D continuum-model calculations without image potential (dashed lines), which predict a far too low current. For $\sigma = 75$ meV the agreement between the 3D Master-Equation and the 1D continuum-model results in the ILC regime is excellent. For $\sigma = 150$ meV the 1D continuum model underestimates the current density in the ILC regime by a factor of about 8. The origin of the underestimation of the current density by the 1D model in the SCLC and ILC regime is investigated in the next section.

4.4 Three-dimensional structure of the current distribution; consequences for different models

In order to obtain a better insight in the effects that cause the discrepancies between the 3D Master-Equation and the 1D continuum-model results, we have studied the three-dimensional structure of the current distribution. **Fig. 4.3** shows the room-temperature current-density distribution for the 22 nm device at a bias of $V = 2$ V, an injection barrier $\Delta = 1$ eV, for $\sigma = 75$ (**Fig. 4.3(a,b)**) and $\sigma = 150$ meV (**Fig. 4.3(c,d)**). **Fig. 4.3(a)** and **Fig. 4.3(c)** show the current distribution as viewed from the side, whereas **Fig. 4.3(b)** and **Fig. 4.3(d)** show views from the injecting to the collecting electrode. The local current density has been calculated by summing for each site in a box of $13 \times 50 \times 50$ sites the net currents to the 9 sites in the adjacent layer to which we allow hopping and attributing this sum to this site, according to Eq. (4.5). We have used the same disorder realization for $\sigma = 75$ meV and $\sigma = 150$ meV, apart from an obvious factor of two. The figures reveal that the current density is strongly filamentary for $\sigma = 150$ meV and already weakly filamentary for $\sigma = 75$ meV. Such filamentary structures in the current distribution have been reported before⁴⁻⁸ and are caused by percolation effects, which increase with increasing disorder. We have also investigated the current distributions for zero injection barrier and found a less pronounced but still clear filamentary structure, showing that this structure is enhanced by the injection barrier, but that its existence does not require a finite injection barrier.

Clearly, the filamentary structure of the current distribution means that almost all the current flows through a relatively small number of sites. Since the 1D continuum model is based on the EGDM, in which the *bulk* effects of the filamentary structure of the current have been properly taken into account,¹⁰ it can be expected that the 1D continuum model works properly for thick devices. Indeed, **Fig. 4.1(a,b)** shows that for the device with $L = 102$ nm device the agreement between the 3D Master-Equation and 1D continuum-model results is very good. As long as the typical length scale of the spatial structure of the current distribution is small compared to the device thickness, one can speak about a "local" mobility that can successfully be used in 1D continuum models. However, for devices with a thickness of the order of or smaller than this typical length scale the concept



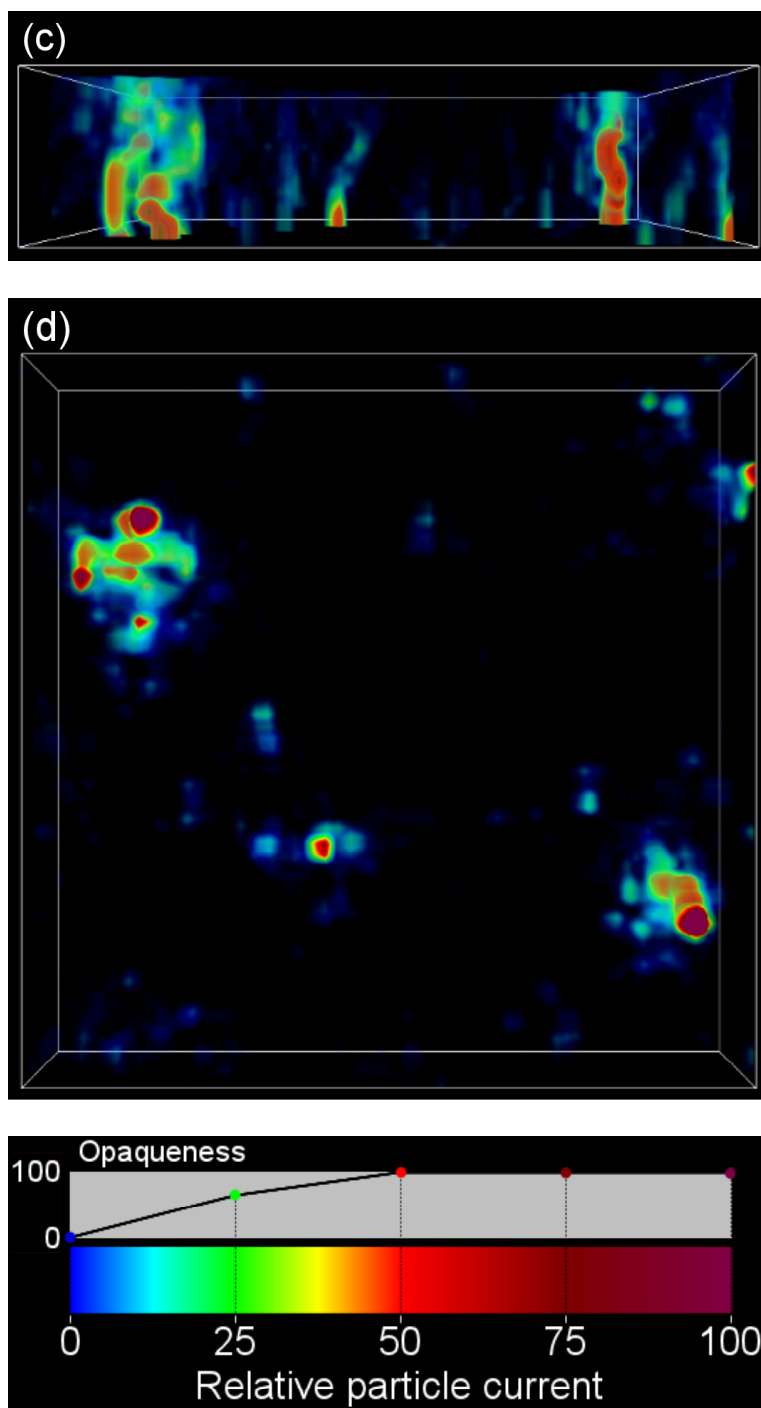


Figure 4.3: Three-dimensional representation of the relative local current density, given by $J_{\text{rel},i} = J_i/J_{\text{av}}$, with J_i the absolute local current density given by Eq. (4.5) and J_{av} the average local current density in the device. The displayed results are for devices with disorder strengths of $\sigma = 75$ meV ((a) and (b)) and $\sigma = 150$ meV ((c) and (d)), device thickness $L = 22$ nm, driving voltage $V = 2$ V, injection barrier $\Delta = 1$ eV, room temperature, and lattice constant $a = 1.6$ nm. In (a) and (c) the device is viewed from the side with the injecting electrode at the bottom, whereas (b) and (d) give views from the injecting to the collecting electrode. The local current density is coded with a color and transparency, with the coding scheme indicated at the bottom. The lateral grid size used is 50×50 sites. The boundaries of the device are depicted by a white bounding box.

of a local mobility breaks down.⁶ The presence of current filaments from the injecting to the collecting electrode then leads to a *higher* net current than obtained with a 1D continuum model, the effect becoming larger for larger electric field. This is the reason for the discrepancies found in **Fig. 4.1(d)** and **Fig. 4.2(b)** found for $L = 22$ nm and $\sigma = 150$ meV between the 3D Master-Equation and 1D continuum-model results, both in the SCLC and ILC regime. Indeed, one can see from **Fig. 4.3** that the typical length scale of the structures in the current distribution is roughly of the order of 10 nm. Since the filamentary structure is less pronounced for smaller disorder the agreement between the 3D Master-Equation and 1D results in **Fig. 4.1(c)** and **Fig. 4.2(a)** found for $\sigma = 75$ meV is much better.

In the remainder of this section, we discuss to what extent the filamentary nature of the current density in the ILC regime is properly taken into account in the Burin-Ratner model¹⁹ and the Arkhipov model.¹⁶ The above point of view about the underestimation of the current by the 1D continuum model is supported by an analysis of the current density using the Burin-Ratner (BR) model.¹⁹ Within that model, it is assumed that the total current is a simple sum of independent contributions from linear (one-dimensional) filaments that start at all injecting sites. These contributions can be obtained by solving a 1D master equation for a chain of sites with random Gaussian disorder. We have used the exact solution for the contribution to the current density from a filament at the point (i_y, i_z) , given by Eq. (5) in Ref. 19:

$$J(i_y, i_z) = \frac{\exp\left(-\frac{e\Delta}{k_B T}\right)}{\exp\left(-\frac{e\Delta}{k_B T}\right) + 2 \sum_{i_x=2}^{L_x-1} \exp\left(\frac{E(i_x) - e a i_x F + e \Phi_{\text{im}}(i_x)}{k_B T}\right)} J_0, \quad (4.10)$$

with the energies $E(i_x)$ taken randomly from a Gaussian DOS with width σ , and with $\Phi(i_x)$ the image potential at site i_x , given by Eq. (4.3). In contrast to the original expression in Ref. 19 this expression takes into account the finite thickness of the device. The current density is expressed relative to J_0 , defined as

$$J_0 \equiv \frac{e\nu_0}{a^2} \exp[-2\alpha a], \quad (4.11)$$

which is the current density that would be obtained from a master-equation calculation for a system with all sites fully occupied ($p_i = 1$), in the large-field limit, neglecting the $(1 - p_i)$ factors that prohibit double occupation (cf. Eq. (4.4)). The total current density is then obtained by averaging the contributions from a sufficiently large number of points (i_y, i_z) . These contributions are obtained by applying Eq. (4.10) repeatedly for a large ensemble of random sets of energies $E(i_x)$, and are thus assumed to be uncorrelated. The assumption of 1D filaments, made within the BR model, is consistent with the observation in **Fig. 4.3** of straight filaments close to the injecting electrode. We note that Eq. (4.10) is derived by assuming instead of the Miller-Abraham hopping rate Eq. (4.1b) a hopping rate

$$W_{ij} = \frac{\nu_0}{1 + \exp\left[\frac{E_j - E_i}{k_B T}\right]}. \quad (4.12)$$

We checked that the differences between the two hopping rates only lead to minor differences in the final results.

The current density as predicted from the BR model is indicated in **Fig. 4.2** (line with plusses). For $\Delta > 0.8$ eV, the model provides a quite good approximation to the results of the full 3D Master-Equation results for large disorder ($\sigma = 150$ meV), so that it may be concluded that the discrepancy with the 1D continuum-model results for large injection barriers is indeed the consequence of a neglect of transport via rare very easy pathways. **Fig. 4.2** also shows that the BR model predicts a too high current density for injection barriers smaller than ≈ 0.5 eV and ≈ 0.7 eV for $\sigma = 75$ and $\sigma = 150$ meV, respectively. This may be attributed to the fact that the BR model neglects the effects of space charge, as may be concluded from the results of the 3D Master-Equation calculations with the space-charge potential switched off (**Fig. 4.2**, open circles), which follow the BR results to lower values of Δ .

Another consequence of the filamentary nature of the current density is the occurrence of a statistical variation of the total current through a given surface area. As an example, **Fig. 4.4** shows the distributions of the current density through 80×80 nm² devices (i.e. 50×50 sites) of the type studied in **Fig. 4.3**, for $\Delta = 1$ eV, and with $\sigma = 75$ (**Fig. 4.4(a)**) and $\sigma = 150$ meV (**Fig. 4.4(b)**), obtained from 3D Master-Equation calculations (light-gray bars) and from the BR model (black bars). The distributions were obtained using the BR model for 800 and 1600 devices in the case of a disorder strength $\sigma = 75$ and $\sigma = 150$ meV, respectively, with different random Gaussian disorder realizations. For $\sigma = 75$ meV, the statistical variations are moderate. The width of the distributions is limited to approximately 40% of the average current density and the largest observed current density in the ensemble considered is approximately 4 times the average value. The BR distribution is clearly shifted to smaller current densities as compared to the Master-Equation distribution. We attribute this to the limitation to one dimension of hops in the BR model, which leads to lower currents than when 3D hopping is allowed. For $\sigma = 150$ meV, the statistical variations are very large. The width of the distributions is comparable to the peak current density and the largest observed current density in the ensemble considered is now ~ 90 times the average value (outside the range displayed in the figure). The strongly asymmetric distributions give rise to an average current density that is equal to more than twice the peak current densities (note the log-scale for the x -axis). The relative shift of the BR distribution to smaller current densities is significantly larger than for $\sigma = 75$ meV. The fact that the BR model underestimates the current density because of its neglect of side-jumps is just visible in (**Fig. 4.2(b)**).

Whereas the BR model yields already at the relatively high fields considered in **Fig. 4.2** (10^8 V/m) current densities that are lower than the 3D Master-Equation results, it may be expected that the model breaks down even more clearly at small fields. Trajectories containing side-jumps are then expected to yield even more important contributions to the current density. This is confirmed by the results given in **Fig. 4.5**. For devices with $\sigma = 75$ meV, the figure displays the electric-field dependence of the injection-limited current

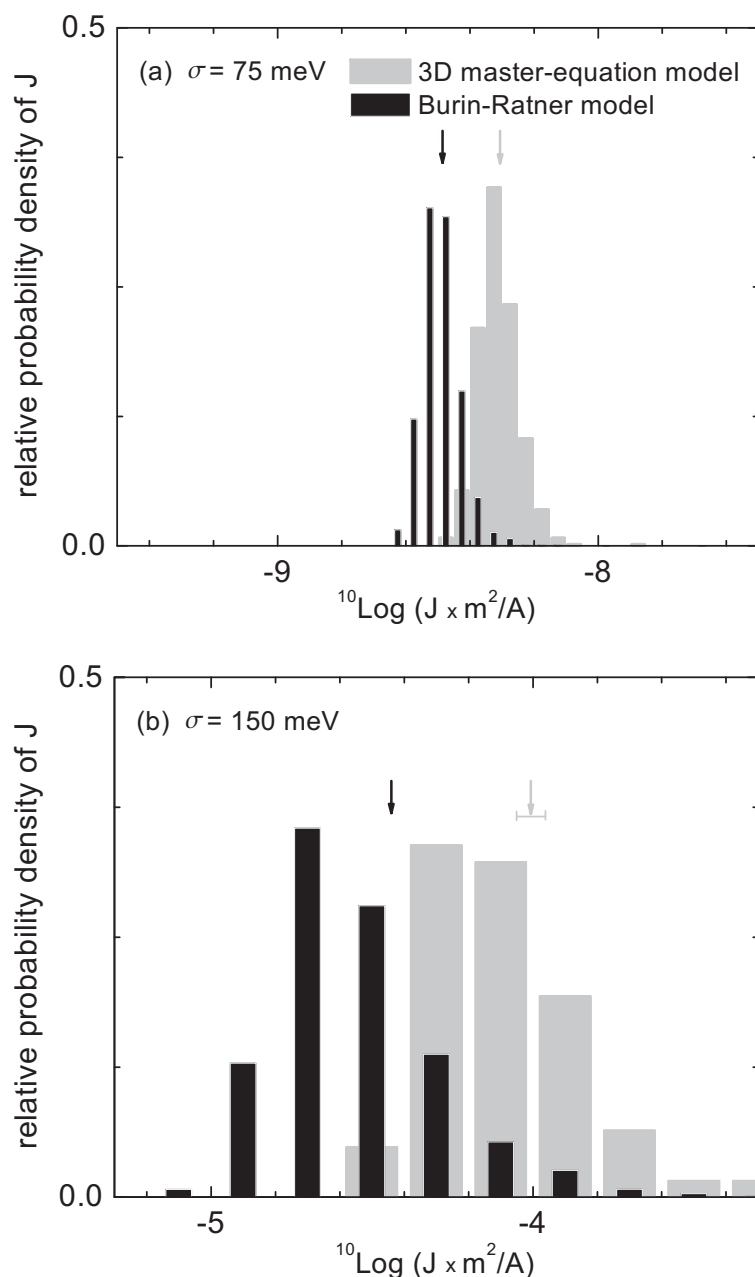


Figure 4.4: Probability distribution of the current density J . The displayed results are for devices with disorder strengths of $\sigma = 75 \text{ meV}$ (a) and $\sigma = 150 \text{ meV}$ (b), device thickness $L = 22 \text{ nm}$, room temperature, lattice constant $a = 1.6 \text{ nm}$, and injection barrier $\Delta = 1 \text{ eV}$. The lateral grid size is 50×50 sites. Equally sized bins on a logarithmic scale have been used and the normalization is such that the sum of the lengths of the bars is equal to one. Light-gray bars: results obtained from the 3D Master-Equation model. Black bars: results obtained from the Burin-Ratner model. For devices with disorder strength of $\sigma = 75$ (150) meV 656 (62) samples were used for the 3D Master-Equation model and 3200 (6400) samples for the Burin-Ratner model. The arrows indicate the corresponding average current densities, which could be very accurately determined, except for the Master-Equation result for $\sigma = 150 \text{ meV}$, where an error bar indicates the uncertainty.

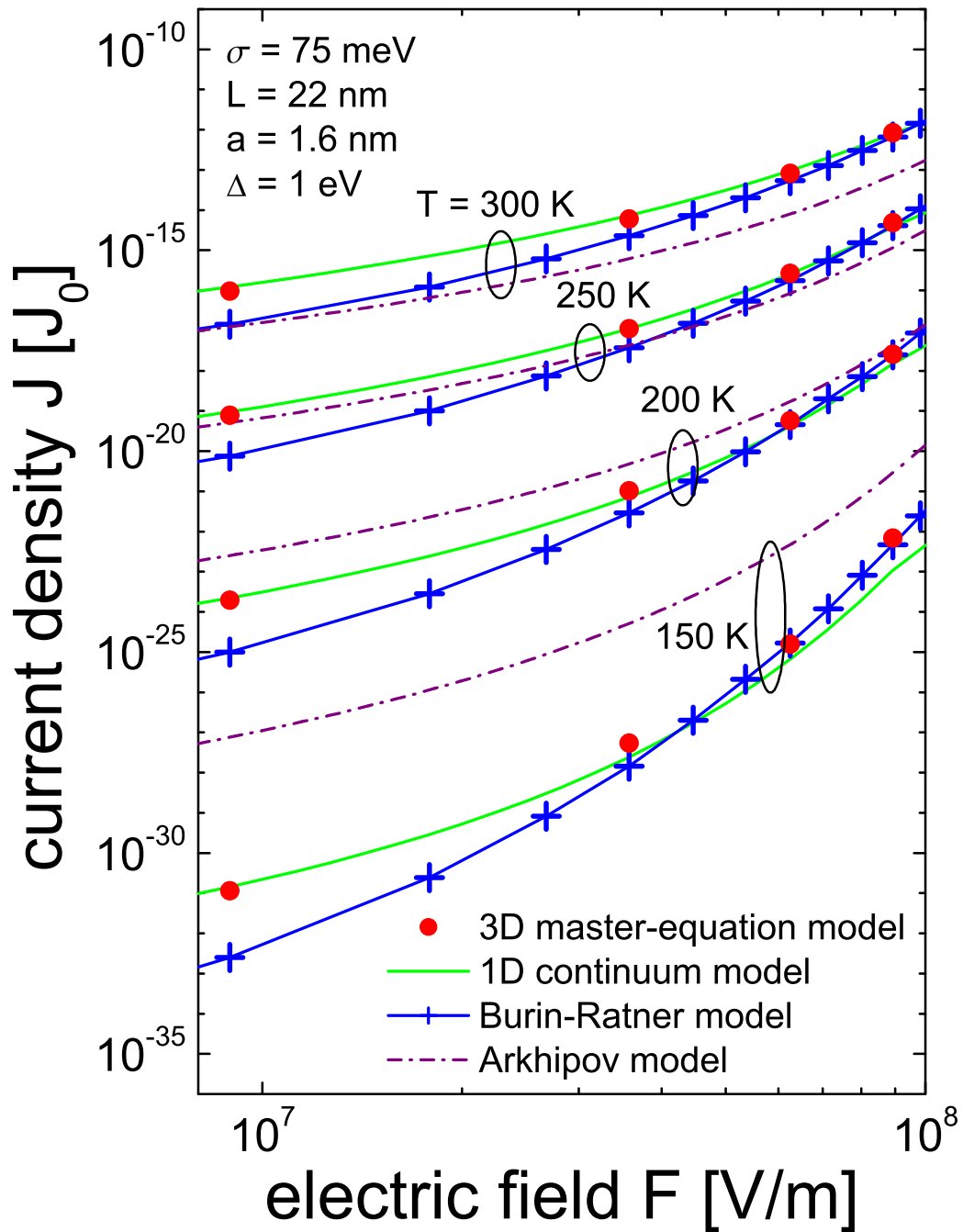


Figure 4.5: The current density (J in units of J_0 as given by Eq.(4.11)) as function of the electric field (F), for different temperatures and four different models.

density as obtained from the 3D Master-Equation model, the 1D-continuum model, the BR model and the Arkhipov model (discussed later in this section). The injection barrier is $\Delta = 1$ eV. The temperature is varied from 300 K to 150 K, corresponding approximately to $\hat{\sigma} = 3$ and $\hat{\sigma} = 6$, respectively. It has already been established from **Fig. 4.1** that the voltage dependence of the current density as obtained from the 1D continuum model is in fair agreement with the results from the 3D Master-Equation model. Therefore, we regard these results (solid curves) as a benchmark. The figure shows that the BR model underestimates the current density at small fields. This indeed suggests that at smaller fields non-linear trajectories, which are neglected within the BR model, contribute significantly to the current density.

The 1D continuum model yields the following expression for the current density in the ILC regime:

$$\begin{aligned}
 J &= en_c \mu(n_c, F) F \\
 &\cong \frac{e}{a^3} \exp \left[-\frac{e\Delta'(F)}{k_B T} + \frac{1}{2} \hat{\sigma}^2 \right] \mu(0, F) F \\
 &= \frac{e}{a^3} \exp \left[-\frac{e\Delta'(F)}{k_B T} + \frac{1}{2} \hat{\sigma}^2 \right] \frac{a^2 \nu_0 e c_1}{\sigma} \exp(-c_2 \hat{\sigma}^2) \frac{\mu(0, F)}{\mu(0, 0)} F \\
 &\cong \exp \left[-\frac{e\Delta'(F)}{k_B T} + \left(\frac{1}{2} - c_2 \right) \hat{\sigma}^2 \right] f(F) \frac{eaF}{\sigma} J_0,
 \end{aligned} \tag{4.13}$$

with $\Delta'(F)$ as given by Eq. (4.9). Use has been made of the fact that the barrier is sufficiently large, so that transport is in the Boltzmann regime; Eq. (A2) in Ref. 24 can therefore be used to relate n_c to Δ' . Also the expressions for the temperature and field dependence of the mobility, given in Ref. 10, have been used, with the approximation $c_1 = 1.8 \times 10^{-9} \approx \exp(-2\alpha a) = \exp(-20)$, with $c_2 = 0.42$ and with $f(F)$ a factor that expresses the field dependence of the mobility:

$$f(F) \cong \exp \left\{ 0.44(\hat{\sigma}^{3/2} - 2.2) \left[\sqrt{1 + 0.8 \left(\frac{eaF}{\sigma} \right)^2} - 1 \right] \right\}. \tag{4.14}$$

For the devices studied, the maximum of the field scale used in **Fig. 4.5** corresponds to $eaF/\sigma \approx 2$. It follows from Eqs. (4.13) and (4.14) that at all temperatures considered approximately 30 % of the increase of the current density (on a log scale) with the field, observed in **Fig. 4.5**, is due to the field dependence of the mobility. The remainder of the effect is due to the energy-barrier lowering with increasing field and to the linear (eaF/σ) -factor in Eq. (4.13).

The dash-dotted curves in **Fig. 4.5** give the current density as obtained from the 1D continuum injection model by Arkhipov *et al.*¹⁶ Within this model, it is assumed that the current density can be written as an integral over contributions due to hops over variable distances from the electrode to sites at distance $x_0 > a$, and with energy E' with respect

to the Fermi level in the electrode. The contribution of each hop is weighed by the escape probability $w_{\text{esc}}(x_0)$ out of the image-potential well in which the charge carrier resides after the first hop, towards the bulk of the device:

$$J = e \int_a^\infty dx_0 \int_{-\infty}^\infty dE' W(x_0, E') w_{\text{esc}}(x_0) g(E' - e\Delta + ex_0 F - e\Phi_{\text{im}}(x_0)), \quad (4.15)$$

with $W(x_0, E)$ the Miller-Abrahams hopping rate given by Eq. (4.1) and with $w_{\text{esc}}(x_0)$ given by

$$w_{\text{esc}}(x_0) = \frac{\int_a^{x_0} dx \exp\left(\frac{-exF + e\Phi_{\text{im}}(x)}{k_B T}\right)}{\int_a^\infty dx \exp\left(\frac{-exF + e\Phi_{\text{im}}(x)}{k_B T}\right)}. \quad (4.16)$$

It may be seen from **Fig. 4.5** that the Arkhipov model yields a field dependence of the current density that is quite close to that obtained from the 1D continuum model (and from the 3D Master-Equation model), but that the temperature dependence of the current density is much smaller. We tentatively attribute this to the fact that in the expression for the escape probability Eq. (4.16) the effect of disorder is neglected. The percolative nature of the escape process is expected to be more strongly temperature dependent than as predicted by Eq. (4.16), just as the mobility of disordered materials is more strongly temperature dependent than that of ordered materials. An earlier test of the validity of the Arkhipov model, using Monte-Carlo calculations, has not been able to reveal this inadequacy of the model, as the analyses have been carried out only for relatively high temperatures.¹⁷

4.5 Summary and conclusions

We have performed a three-dimensional modeling study of the single-carrier transport in devices that consist of a single layer of an organic semiconducting material with a Gaussian distribution of site energies with standard deviation σ , sandwiched in between two metallic electrodes. The voltage-dependent current density was obtained by solving the Pauli master equation corresponding to the related hopping problem, taking the effects of the space charge, the image potential, a finite injection barrier, and the full dependence of the hopping rates on temperature, carrier density, and electric field into account.

The calculations reveal that the current density can be strongly filamentary, and that the current filaments become more pronounced with increasing disorder parameter $\hat{\sigma} = \sigma/(k_B T)$, decreasing layer thickness, and increasing injection barrier. Visualizations of the three-dimensional (3D) current density show that these filaments become straight near the injecting electrode when the injection barrier is large, for high fields and for strong disorder, as assumed in a one-dimensional (1D) master-equation model by Burin and Ratner.¹⁹ In that limit the non-uniformity of the current density is found to give rise to wide distributions of the current density in an ensemble of nanometer-scale devices. The average current

density can be much larger than the peak value in the distribution due to the occurrence of a small fraction of devices with extremely high current densities.

A quantitative analysis of the results has been given by making a comparison with the results from a 1D continuum drift-diffusion model, which extends an earlier developed model⁹ by including the image-charge effect. The voltage-dependent current-density curves as obtained from both models show a remarkably good agreement (**Fig. 4.1**), except for large voltages, disorder parameters, and injection barriers, where the full 3D calculations reveal an enhanced current density. This is attributed to the effects of rare easy pathways for the elementary current density, as confirmed in Section 4.4 from an analysis using the Burin-Ratner model.

We conclude that the 3D Master-Equation model developed has provided valuable insight in the degree of validity of an also newly developed 1D continuum model. The limitations of the 1D model arise under conditions at which the current density becomes highly non-uniform. However, 1D continuum drift-diffusion models will remain important as a computationally efficient tool for evaluating the materials and device properties of OLED-type devices. In our view, future research towards the improvement of such models should focus on the three following subjects: (i) the explicit consideration of the effect of current filaments, (ii) the development of an approach to the image potential contribution in the SCLC regime that more consistently takes the space charge near the electrodes into account, (iii) the possible effects of positional disorder, in particular on the injection-limited current density.

References

- [1] Burroughes, J.; Bradley, D.; Brown, A.; Marks, R.; Mackay, K.; Friend, R.; Burns, P.; Holmes, A. *Nature* **1990**, *347*, 539.
- [2] Drury, C.; Mutsaers, C.; Hart, C.; Matters, M.; de Leeuw, D. *Appl. Phys. Lett.* **1998**, *73*, 108.
- [3] Brabec, C.; Dyakonov, V.; Parisi, J.; Sariciftci, N. *Organic Photovoltaics: Concepts and Realization*; Springer-Verlag: Berlin, 2003.
- [4] Tutiš, E.; Batistić, I.; Berner, D. *Phys. Rev. B* **2004**, *70*, 161202(R).
- [5] Meisel, K.; Pasveer, W.; Cottaar, J.; Tanase, C.; Coehoorn, R.; Bobbert, P.; Blom, P.; de Leeuw, D.; Michels, M. *Phys. Stat. Sol. (c)* **2006**, *3*, 267.
- [6] Rappaport, N.; Preezant, Y.; Tessler, N. *Phys. Rev. B* **2007**, *76*, 235323.
- [7] Kwiatkowski, J. J.; Nelson, J.; Li, H.; Bredas, J. L.; Wenzel, W.; Lennartz, C. *Phys. Chem. Chem. Phys.* **2008**, *10*, 1852.

-
- [8] Yu, Z.; Smith, D.; Saxena, A.; Martin, R.; Bishop, A. *Phys. Rev. B* **2001**, *63*, 085202.
- [9] van Mensfoort, S.; Coehoorn, R. *Phys. Rev. B* **2008**, *78*, 085207.
- [10] Pasveer, W.; Cottaar, J.; Tanase, C.; Coehoorn, R.; Bobbert, P.; Blom, P.; de Leeuw, D.; Michels, M. *Phys. Rev. Lett.* **2005**, *94*, 206601.
- [11] de Levie, R.; Moreira, H. *J. Membrane Biol.* **1972**, *9*, 241.
- [12] Emtage, P.; O'Dwyer, J. *Phys. Rev. Lett.* **1966**, *16*, 356.
- [13] Scott, J.; Malliaras, G. *Chem. Phys. Lett.* **1999**, *299*, 115.
- [14] Masenelli, B.; Berner, D.; Bussac, M.; Nüesch, F.; Zuppiroli, L. *Appl. Phys. Lett.* **2001**, *79*, 4438.
- [15] Gartstein, Y.; Conwell, E. *Chem. Phys. Lett.* **1996**, *255*, 93.
- [16] Arkhipov, V.; Emelianova, E.; Tak, Y.; Bäessler, H. *J. Appl. Phys.* **1998**, *84*, 848.
- [17] Arkhipov, V.; Wolf, U.; Bäessler, H. *Phys. Rev. B* **1999**, *59*, 7514.
- [18] van Woudenberg, T.; Blom, P.; Vissenberg, M.; Huiberts, J. *Appl. Phys. Lett.* **2001**, *79*, 1697.
- [19] Burin, A.; Ratner, M. *J. Chem. Phys.* **2000**, *113*, 3941.
- [20] Ng, T.; Silveira, W.; Marohn, J. *Phys. Rev. Lett.* **2007**, *98*, 066101.
- [21] Miller, A.; Abrahams, E. *Phys. Rev.* **1960**, *120*, 745.
- [22] Simmons, J. *J. Appl. Phys.* **1963**, *34*, 1793.
- [23] Roichman, Y.; Tessler, N. *Appl. Phys. Lett.* **2002**, *80*, 1948.
- [24] Coehoorn, R.; Pasveer, W.; Bobbert, P.; Michels, M. *Phys. Rev. B* **2005**, *72*, 155206.

Chapter 5

Monte-Carlo study of charge transport in organic sandwich-type single-carrier devices: effects of Coulomb interactions

ABSTRACT

We present the results of Monte-Carlo simulations of transport of charge carriers of a single type in devices consisting of a disordered organic semiconductor sandwiched in between two electrodes. The simulations are based on hopping of carriers between sites with a Gaussian energetic distribution, which is either spatially uncorrelated or has a correlation based on interactions with randomly oriented dipoles. Coulomb interactions between the carriers are taken into account explicitly. For not too small injection barriers between the electrodes and the organic semiconductor, we find that the current obtained from the simulations can be described quite well by a one-dimensional drift-diffusion continuum model, which takes into account the long-range contributions of Coulomb interactions through the space-charge potential. For devices with low injection barriers, however, the simulations yield a considerably lower current than the continuum model. The reduction of the current for uncorrelated disorder is larger than for correlated disorder. By performing simulations in which the short-range contributions of the Coulomb interactions between the carriers are omitted we demonstrate that the difference is caused by these short-range contributions. We can rationalize our results by analyzing the three-dimensional current distributions resulting from the simulations for different injection bar-

riers with and without taking into account these short-range contributions.¹

¹The contents of this chapter are based on work that has been published: J.J.M. van der Holst, F.W.A. van Oost, R. Coehoorn, P.A. Bobbert, *Physical Review B: Condensed Matter* **2009**, *80*, 235202

5.1 Introduction

Organic light-emitting diodes (OLEDs) are promising high-efficiency light-sources that are presently used in a variety of lighting and display applications. They consist of one or more layers of organic semiconducting material sandwiched in between electrodes, of which one is usually a low-work function metal and the other a transparent conducting oxide like indium-tin-oxide. Despite the growing commercial success of OLEDs, knowledge of many aspects of their functioning is still fragmental.

One of the most important of these aspects is the charge transport. It has become clear in the last two decades that disorder plays a very important role in charge transport since it leads to the localization of electronic states. The transport is assumed to take place by hopping of carriers between the sites at which the states are localized. The energetic disorder is often modeled by assuming that the on-site energies are random variables, taken from a Gaussian density of states (DOS), resulting in what has been called the Gaussian Disorder Model (GDM). The dependence of the charge-carrier mobility μ on temperature and electric field in the GDM was investigated by Bässler *et al.* using Monte-Carlo (MC) simulations of the hopping transport of a single carrier in a Gaussian DOS.^{1,2}

Gartstein and Conwell suggested that spatial correlation in the disorder should be included to better describe experimental charge-transport data. These data show a mobility μ with a Poole-Frenkel dependence on the electric field, $\mu \propto \exp[\gamma\sqrt{F}]$, in a rather wide range of electric-field strengths F , with γ a factor depending on temperature.³ In particular, it was suggested that the fields of randomly oriented dipoles could be the origin of such correlated disorder.^{4,5} The resulting model is known as the Correlated Disorder Model (CDM).

In addition, the dependence of the mobility on the carrier density has to be accounted for at densities where state-filling effects become important.^{6,7} For such densities, the independent-carrier assumption in the MC simulations of Bässler *et al.*,^{1,2} also called the Boltzmann limit, is invalid. The mobility increases with increasing density, since the occupation of the lowest-energy states by carriers reduces the effect of these states as trapping centers. Pasveer *et al.*⁸ performed a computational study - involving a solution of the Pauli master equation for the occupational probabilities of a cubic array of hopping sites - of the dependence of the mobility on temperature, electric field, and carrier density in the case of a spatially uncorrelated Gaussian DOS. It was shown that the mobility obtained from that study can provide an excellent quantitative explanation of measured current-voltage characteristics of hole-only devices of two derivatives of the semiconducting polymer poly(*p*-phenylenevinylene) (PPV)⁸ as well as a derivative of polyfluorene.⁹ It was found that in these devices at room temperature the density dependence of the hole mobility is more important than the field dependence. We will refer to this extension of the GDM, regarding the inclusion of the density dependence of the mobility, as the Extended Gaussian Disorder Model (EGDM).

For the case of a spatially correlated Gaussian DOS, a similar computational study of

the density dependence of the mobility was performed by Bouhassoune *et al.*¹⁰ We will refer to this extension of the CDM as the Extended Correlated Disorder Model (ECDM). Comparison of EGDM and ECDM modeling of current-voltage characteristics of hole-only devices of conjugated polymers like derivatives of PPV¹⁰ and a polyfluorene-based co-polymer¹¹ has led to the conclusion that for these polymers the inter-site distance as obtained from a fit of the EGDM modeling is more realistic than the one obtained from a fit of the ECDM modeling. On the other hand, a similar comparison of EGDM and ECDM modeling of current-voltage characteristics of hole-only devices of the molecule *N, N'*-bis(1-naphthyl)-*N, N'*-diphenyl-1, 1'-biphenyl-4, 4'-diamine (α -NPD) and of electron-only devices of the molecule bis(2-methyl-8-quinolinolato)(4-phenylphenolato)aluminum (BALq) shows that the inter-site distance as obtained from a fit with the ECDM modeling is more realistic than the one obtained with the EGDM modeling.^{12,13} This work suggests that for the investigated polymers and small-molecule semiconductors the EGDM and the ECDM, respectively, are thus the best models to describe charge transport.

In the above device-modeling studies within the EGDM and ECDM a one-dimensional (1D) continuum drift⁸ or drift-diffusion equation^{9,14} was solved using a mobility with a parametrization of the dependence on temperature, electric field, and carrier density based on a numerical solution for the mobility obtained by solving the Pauli master equation for the site occupational probabilities.^{8,10} In order to investigate the consistency of this approach and to study the injection of carriers in more detail, we performed a computational study of single-carrier devices by solving the Pauli master equation for a collection of sites representing a full three-dimensional (3D) device, including its electrodes.¹⁵ The details concerning this computational study are described in the previous chapter. The density of states was taken to be Gaussian and to be spatially uncorrelated, corresponding to the EGDM. The effects of space charge, the image-charge potential, and an injection barrier were taken into account. The space charge was taken into account in a layer-averaged way, neglecting any explicit short-range Coulomb interactions between charges. The image-charge potential was taken into account by including the Coulomb interaction between a charge and its image charge when it is close to one of the electrodes.

In these 3D device studies,¹⁵ the current density was found to be highly inhomogeneous, in agreement with other studies.¹⁶⁻¹⁹ This inhomogeneous structure involves narrow current filaments that carry almost all the current, characteristic of the percolative nature of charge transport in disordered materials. Despite these 3D inhomogeneities, the current-voltage characteristics were found to be described quite well by the 1D continuum drift-diffusion device model of Ref. 14, with an image-charge-induced lowering of the injection barrier included in a similar way as in the work of Emtage and O'Dwyer.²⁰ For thin devices and high disorder strengths the current obtained from the 3D calculations was found to be somewhat higher than that obtained from the 1D drift-diffusion model. It is in this regime that the current density becomes extremely non-uniform. It was found that in this regime the current-voltage characteristics can be described rather well with a model of Burin and Ratner, which assumes injection of carriers along 1D current pathways.²¹

While the above 3D device studies properly take into account the effects of percolation, the effects of Coulomb interactions between the carriers are only taken into account in an average way by evaluating a layer-averaged space charge. In fact, the short-range effects of Coulomb interactions between carriers cannot be taken into account in a consistent way within the Master-Equation approach, since this approach involves the time-averaged and not the actual occupational probabilities of the sites. On the other hand, in MC simulations it is - in principle - straightforward to take the effects of Coulomb interactions fully into account. For a bulk organic semiconductor, these effects have been investigated using MC simulations. A description of the results of this MC study is given in chapter 3. In general, it was found that the mobility in the case that Coulomb interactions are taken into account agree quite well with the mobility in the case that the Coulomb interactions are not taken into account. However, for low electric fields, the mobility was somewhat lower in the presence of Coulomb interactions. For the highest studied carrier density ($0.1a^{-3}$) the difference was about a factor 1.7. Therefore, it is important to study the effects of Coulomb interactions in devices, where high carrier densities can be reached at the electrodes in the case of low injection barriers and where the carrier density can vary over several orders of magnitude within a distance of only a few nanometers from the electrodes.

Another reason to study the effects of Coulomb interactions explicitly is a double-counting problem that occurs when both the space charge and the image-charge potential are taken into account either in a 3D Master-Equation approach or in a 1D continuum drift-diffusion model. The problem is that in taking into account the space charge and the correct boundary conditions for the electrostatic potential at the electrodes, the image-charge potential related to the space charge has already been taken into account. When considering a particular charge, it is therefore not consistent to take into account the interaction of this charge with its image charge, since the contribution of this charge to the space charge was already accounted for, albeit in an average way. It is not a priori clear what the size is of the error that is made by this double counting. The problem of taking into account the image-charge potential in a consistent way was recently discussed in detail by Genenko *et al.*²² and in Subsection 5.2.2 and Section 5.3 we will discuss this issue further. The problem can obviously be circumvented by performing MC simulations in which Coulomb interactions are taken into account explicitly.

In the present work we will show and discuss the results of MC simulations for single-carrier devices consisting of an organic semiconductor sandwiched in between two equal electrodes. We will take into account Coulomb interactions in the following way. Around every charge in the device a cut-off sphere is defined. Interactions with charges within this sphere are taken into account explicitly, while interactions with charges outside this sphere are taken into account in a layer-averaged way. With an optimal choice of the radius of the cut-off sphere, we take into account the short-range as well as the long-range contributions of the Coulomb interactions in a proper way, while maintaining a sufficient computational efficiency. Moreover, by reducing the radius of the cut-off sphere to zero, we can study the situation where Coulomb interactions are only taken into account in a layer-averaged way,

corresponding to the approximation made in the 3D Master-Equation approach and the 1D continuum drift-diffusion model.

This chapter is built up as follows. Section 5.2 discusses the theory and the methods used. In Subsection 5.2.1 we describe our MC approach and discuss in detail our method to take into account Coulomb interactions, which was briefly sketched in the previous paragraph. Subsection 5.2.2 discusses the 1D drift-diffusion model used for calculating the current density in single-carrier devices. In Section 5.3 we present the current-voltage characteristics of devices with uncorrelated as well as correlated disorder, corresponding to the EGDM and ECDM, respectively. For the case of the EGDM, we compare our results with our previous work based on the Master-Equation approach,¹⁵ (as described in the previous chapter) while for both the EGDM and the ECDM we compare our results with those of 1D drift-diffusion modeling. In Section 5.4 we show plots of the 3D current density in devices with correlated and uncorrelated disorder, with and without taking into account the short-range contributions of the Coulomb interactions. These results allow us to rationalize the effects of short-range Coulomb interactions. Section 5.5 contains a summary and conclusions.

5.2 Theory and methods

5.2.1 Monte-Carlo method

In this section we describe our MC approach for calculating the current density in a single-carrier device consisting of an organic semiconducting material sandwiched in between two electrodes. The organic semiconductor and the electrodes are modeled by a three-dimensional cubic $L_x \times L_y \times L_z$ lattice with lattice constant a . A lattice site is denoted by $\mathbf{i} = \{i_x, i_y, i_z\}$. The sites with $i_x = 1$ and $i_x = L_x$ represent the injecting and collecting electrodes, respectively. The other sites, which we call “organic” sites, represent localized electronic states in the organic semiconductor. Periodic boundary conditions are taken in the y - and z - directions. The applied electric field is in the x -direction.

We assume that the hopping of charge carriers from one site to another is a thermally assisted tunneling process with a coupling to an acoustical phonon bath. The hopping rate $W_{\mathbf{ij}}$ from site \mathbf{i} to \mathbf{j} is then described by the Miller-Abrahams formalism,²³

$$W_{\mathbf{ij}} = \nu_0 \exp \left[-2\alpha |\mathbf{R}_{\mathbf{ij}}| - \frac{\Delta E_{\mathbf{ij}}}{k_B T} \right] \quad \text{for } \Delta E_{\mathbf{ij}} > 0, \quad (5.1a)$$

$$W_{\mathbf{ij}} = \nu_0 \exp [-2\alpha |\mathbf{R}_{\mathbf{ij}}|] \quad \text{for } \Delta E_{\mathbf{ij}} \leq 0, \quad (5.1b)$$

where ν_0 is an intrinsic rate, α is the inverse localization length of the localized wave functions, $|\mathbf{R}_{\mathbf{ij}}| \equiv a|\mathbf{i} - \mathbf{j}|$ is the distance between sites \mathbf{i} and \mathbf{j} , k_B is Boltzmann’s constant, T is the temperature, and $\Delta E_{\mathbf{ij}}$ is the difference $E_{\mathbf{j}} - E_{\mathbf{i}}$ between the on-site energies of

sites \mathbf{j} and \mathbf{i} . The on-site energy $E_{\mathbf{i}}$ of an organic site is equal to the sum of a random on-site energy contribution $E_{\text{rand},\mathbf{i}}$, an electrostatic contribution $e\Phi_{\text{applied},\mathbf{i}}$ due to the applied potential, a contribution $e\Phi_{\text{self},\mathbf{i}}$ due to the Coulomb interactions of a charge with its own (repetitive) image charges, and a contribution $e\Phi_{\text{interact},\mathbf{i}}$ due to Coulomb interactions of a charge with all other charges and their image charges.

We assume that the hopping rate of a charge carrier from an electrode site to an organic site and *vice versa* is described by the same expression (Eq. (5.1)) as the mutual hopping rate between organic sites. It is to be expected that the specific form of this hopping rate has almost no influence on the current-voltage characteristics, as long as there is a thermal equilibrium between the electrode and the adjacent organic sites. We model injection and collection by the electrodes by assuming that there is always a carrier at an electrode site ready to hop to an adjacent empty organic site and that a carrier at an organic site can always hop to an adjacent electrode site. When a charge hops from the injecting or collecting electrode to an organic site, it will experience an injection barrier, Δ_1 or Δ_2 , respectively. To take this into account in Eq. (5.1), we use then $\Delta E_{\mathbf{ij}} = E_{\mathbf{j}} + \Delta_1$ or $\Delta E_{\mathbf{ij}} = E_{\mathbf{j}} + \Delta_2$ when a charge hops from the injecting electrode ($i_x = 1$) or collecting electrode ($i_x = L_x$), respectively, to an organic site. A similar change is made for hopping from an organic site into one of the electrodes.

We consider the situations of spatially uncorrelated as well as spatially correlated disorder. In the case of spatially uncorrelated disorder, the energies $E_{\text{rand},\mathbf{i}}$ are randomly drawn from a Gaussian density of states (DOS):

$$g(E) = \frac{1}{\sqrt{2\pi}\sigma a^3} \exp\left[-\frac{E^2}{2\sigma^2}\right], \quad (5.2)$$

with σ the width of this DOS. For the electrode sites we set these energies equal to 0. In the case of spatially correlated disorder, we take the energy $E_{\text{rand},\mathbf{i}}$ at site \mathbf{i} equal to the electrostatic energy resulting from permanent random dipoles $\mathbf{d}_{\mathbf{j}}$ of equal magnitude d but random orientation on all the other organic sites $\mathbf{j} \neq \mathbf{i}$. The resulting density of states is Gaussian, with a width σ proportional to d .^{5,24,25} The on-site energy $E_{\text{rand},\mathbf{i}}$ is then given by:

$$E_{\text{rand},\mathbf{i}} = - \sum_{\mathbf{j} \neq \mathbf{i}} \frac{e\mathbf{d}_{\mathbf{j}} \cdot \mathbf{R}_{\mathbf{ij}}}{\epsilon_0 \epsilon_r |\mathbf{R}_{\mathbf{ij}}|^3}, \quad (5.3)$$

with the sum over all sites \mathbf{j} in a sufficiently large box around site \mathbf{i} , e the unit charge, ϵ_0 the vacuum permittivity, and ϵ_r the relative dielectric constant of the organic material. The resulting disorder strength is then given by $\sigma \approx 2.35(ed)/(\epsilon_0 \epsilon_r a^2)$. The dimensionless correlation function $C(r)$ between the on-site energies is defined by

$$C(r = |\mathbf{R}_{\mathbf{ij}}|) \equiv \frac{\langle E_{\text{rand},\mathbf{i}} E_{\text{rand},\mathbf{j}} \rangle}{\sigma^2}, \quad (5.4)$$

in which $\langle \dots \rangle$ denotes an ensemble average over different random configurations of the dipole orientations. The correlation function is at an inter-site distance $r = a$ equal to

$C(r = a) \approx 0.7$, at $r = 2a$ equal to $C(r = 2a) \approx 0.35$, and for larger inter-site distances equal to $C(r = |\mathbf{R}_{ij}|) \approx 0.74a/|\mathbf{R}_{ij}|$.²⁶

The Fermi energy in the collecting electrode is taken as the zero-energy reference value, so that the electrostatic contribution due to the applied potential, $e\Phi_{\text{applied},i}$, at the injecting and collecting electrode is given by $e\Phi_{\text{applied},\{i_x=1,i_y,i_z\}} = eV$ and $e\Phi_{\text{applied},\{i_x=L_x,i_y,i_z\}} = 0$, respectively, with V the applied driving voltage. $e\Phi_{\text{applied},i}$ at the organic sites is determined by a linear drop of the potential over the device.

A charge on an organic site will experience an interaction with its repetitive image charges with alternating sign in the two conducting electrodes. Up to order n_{images} the contribution due to the Coulomb interactions of a charge with its image charges, $e\Phi_{\text{self},i}$, is given by

$$e\Phi_{\text{self},i} = -\frac{e^2}{16\pi\epsilon_0\epsilon_r a} \left(\sum_{n=-n_{\text{images}}}^{n_{\text{images}}} \frac{1}{2i_x + 2nL_x} - \sum_{n=-n_{\text{images}}, n \neq 0}^{n_{\text{images}}} \frac{1}{2nL_x} \right), \quad (5.5)$$

at the organic sites. Because of the translational symmetry in the y - and z -direction, $e\Phi_{\text{self},i}$ only depends on the layer index i_x . In our simulations we took $n_{\text{images}} = 100$, which is more than sufficient.

The on-site energy E_i also contains the Coulomb interaction energy $e\Phi_{\text{interact},i}$ with all the other charges and the image charges of these other charges. For practical reasons we split $e\Phi_{\text{interact},i}$ into three contributions. (1) First, we take into account a short-range contribution $e\Phi_{\text{sr},i}$, in which the Coulomb interaction energy with charges within a sphere of radius R_c is taken into account explicitly. (2) Next, we add a layer-averaged contribution $e\Phi_{\text{layer},i}$, in which the Coulomb interaction energy with the other charges is taken into account in a layer-averaged way. Because this contribution also takes into account the layer-averaged Coulomb energy of charges in the disc-shape parts of the layers within the sphere, a double-counting occurs. (3) Therefore, we subtract a contribution $e\Phi_{\text{discs},i}$ to correct for this double-counting. By increasing R_c we can systematically investigate the effect of taking into account the short-range contributions of the Coulomb interactions. For $R_c = 0$, Coulomb interactions of a charge with other charges and their image charges are only taken into account in a layer-averaged way while the interaction of a charge with its own image charges is taken into account explicitly, as in our previous Master-Equation calculations.¹⁵ With increasing R_c , Coulomb interactions are taken into account in an increasingly exact way, with full exactness for $R_c = \infty$. For a well-chosen finite value of R_c we can obtain a good compromise between accuracy and simulation speed. For the device simulations discussed in Sections 5.3 and 5.4 we have taken $R_c = 10a$, which yields sufficient accuracy.

The short-range contribution of the Coulomb potential at site $\mathbf{i} = \{i_x, i_y, i_z\}$ due to a

charge at site $\mathbf{j} = \{j_x, j_y, j_z\}$ and its image charges is given, up to order n_{images} , by

$$f_{c,\mathbf{i},\mathbf{j}} = \begin{cases} \frac{e}{4\pi\epsilon_0\epsilon_r a} \left(\frac{a}{|\mathbf{R}_{\mathbf{i},\mathbf{j}}|} - \sum_{n=-n_{\text{images}}}^{n_{\text{images}}} \frac{1}{\sqrt{(j_x+i_x+2nL_x)^2+(j_y-i_y)^2+(j_z-i_z)^2}} \right. \\ \left. + \sum_{n=-n_{\text{images}}, n \neq 0}^{n_{\text{images}}} \frac{1}{\sqrt{(j_x-i_x+2nL_x)^2+(j_y-i_y)^2+(j_z-i_z)^2}} \right), & |\mathbf{R}_{\mathbf{i},\mathbf{j}}| \leq R_c, \\ 0, & |\mathbf{R}_{\mathbf{i},\mathbf{j}}| > R_c. \end{cases} \quad (5.6)$$

The interaction energy $e\Phi_{\text{sr},\mathbf{i}}$ is then obtained as

$$e\Phi_{\text{sr},\mathbf{i}} = \sum_{\mathbf{j} \neq \mathbf{i}} e_{\mathbf{j}} f_{c,\mathbf{i},\mathbf{j}}, \quad (5.7)$$

with $e_{\mathbf{j}} = e$ when a charge is present at site \mathbf{j} and $e_{\mathbf{j}} = 0$ otherwise. In our simulations we also took $n_{\text{images}} = 100$ in Eq. (5.6).

In order to calculate the layer-averaged electrostatic contribution $e\Phi_{\text{layer},\mathbf{i}}$, the Poisson equation is solved with the layer-averaged charge density ρ_{j_x} in each layer j_x as source term. Consequently, $e\Phi_{\text{layer},\mathbf{i}}$ depends only on the layer index i_x . Due to the image-charge contribution, $e\Phi_{\text{layer},\mathbf{i}}$ is zero at both the injecting and collecting electrode sites.

Finally, we have to calculate the double-counting correction $e\Phi_{\text{discs},\mathbf{i}}$, due to the average charge in the discs in each layer j_x formed by the intersection between the sphere with radius R_c centered around site \mathbf{i} and the layer j_x . These discs have the same layer-averaged charge density ρ_{j_x} as the layer j_x in which they are located. The potential at site \mathbf{i} of the disc in layer j_x , up to order n_{discs} images of the discs, is given by

$$f_{\text{disc},i_x,j_x} = \begin{cases} \frac{\rho_{j_x}}{2\epsilon_0\epsilon_r} \left(\sqrt{R_{j_x-i_x}^2 + a^2(j_x - i_x)^2} - a|j_x - i_x| \right. \\ \left. - \sum_{n=-n_{\text{discs}}}^{n_{\text{discs}}} \left\{ \sqrt{R_{j_x-i_x}^2 + a^2(j_x + i_x + 2nL_x)^2} \right. \right. \\ \left. \left. - a|j_x + i_x + 2nL_x| \right\} \right. \\ \left. + \sum_{n=-n_{\text{discs}}, n \neq 0}^{n_{\text{discs}}} \left\{ \sqrt{R_{j_x-i_x}^2 + a^2(j_x - i_x + 2nL_x)^2} \right. \right. \\ \left. \left. - a|j_x - i_x + 2nL_x| \right\} \right), & 0 < a|j_x - i_x| \leq R_c, \\ 0, & a|j_x - i_x| > R_c, \end{cases} \quad (5.8)$$

with $R_{j_x-i_x} = \sqrt{R_c^2 - a^2(j_x - i_x)^2}$ the radius of the disc in layer j_x . We note that in Eq. (5.8) the Coulomb potential of a continuous disc-shape charge distribution is calculated, while in Eq. (5.6) the Coulomb potential of a discrete set of point charges is calculated. The error as a result of the mismatch of these two potentials becomes smaller when R_c becomes larger. As mentioned before, we have taken $R_c = 10a$, which yields sufficient accuracy. We have taken n_{discs} in our simulations equal to 100,000, which is more than enough for the value $R_c = 10a$ that we have used. We note that n_{discs} should be taken much larger than n_{images} , since the potential of a disc-shape charge distribution decays much slower with increasing distance than the potential of a point-charge. The total contribution $e\Phi_{\text{discs},\mathbf{i}}$ is obtained by:

$$e\Phi_{\text{discs},\mathbf{i}} = \sum_{j_x} e f_{\text{disc},i_x,j_x}. \quad (5.9)$$

Of particular interest is the spatial structure of the current density in the device. To investigate this structure we define at each site \mathbf{i} a local current $J_{\mathbf{i}}$ in the direction of the collecting electrode:

$$J_{\mathbf{i}} = e \frac{(f_{\mathbf{i}} - b_{\mathbf{i}})}{t_{\text{sim}}}, \quad (5.10)$$

with $f_{\mathbf{i}}$ ($b_{\mathbf{i}}$) the total number of forward (backward) hops from site \mathbf{i} in the direction of the collecting (injecting) electrode and t_{sim} the total simulation time. We note that we only allow hops over a maximum distance of $\sqrt{3}a$ (see Section 5.3). Therefore, the forward (backward) hops are over a maximum distance of a in (against) the x -direction. The total current density J_{i_x} in layer i_x is then given by

$$J_{i_x} = \sum_{i_y=1}^{L_y} \sum_{i_z=1}^{L_z} \frac{J_{\mathbf{i}}}{a^2 L_y L_z}, \quad (5.11)$$

where the summation is over all sites in the layer i_x parallel to the electrodes within the device. In a stationary situation, the current density J_{i_x} should be the same in each layer i_x .

Our simulations proceed as follows. We start with an empty device and apply the voltage V . We arbitrarily assume that the hopping carriers are positively charged. Hops of carriers are chosen with weights determined by the hopping rates given by Eq. (5.1). For every hop, a hopping time is chosen from an exponential distribution with an inverse decay time equal to the sum of all possible hopping rates. After every hop the short-range Coulombic energy contribution $e\Phi_{\text{sr},\mathbf{i}}$ is updated for every site in the device to which another hop can occur. For practical reasons, the layer-averaged contributions $e\Phi_{\text{layer},\mathbf{i}}$ and $e\Phi_{\text{discs},\mathbf{i}}$ are only updated after every 100 hops. After a sufficiently long simulation time a stationary situation is obtained, as judged by monitoring the spread and the time dependence of the current densities J_{i_x} in the different layers i_x . After that the data gathering starts. The simulation ends when a sufficiently accurate current density J_{i_x} is obtained for every layer i_x . The final result for the current density is obtained after averaging over a number (typically 10-20) of disorder configurations. The relative accuracy of the resulting averaged current densities J is around 10%.

5.2.2 One-dimensional continuum drift-diffusion model

We will compare the $J(V)$ curves obtained from the MC simulations described in the previous subsection to the $J(V)$ curves obtained from a 1D continuum drift-diffusion model. In this model the current density is given by the drift-diffusion equation:

$$J = n(x)e\mu(x)F(x) - eD(x)\frac{dn(x)}{dx}, \quad (5.12)$$

with $n(x)$, $F(x)$, $\mu(x)$, and $D(x)$ the local charge-carrier density, the local electric field, the local mobility, and the local diffusion coefficient, respectively. $n(x)$ and $F(x)$ are related

to each other via the Poisson equation, $dF/dx = (e/\epsilon_0\epsilon_r)n(x)$. The density, field, and temperature dependence of the local mobility $\mu(x) = \mu(n(x), F(x), T)$ is given by the EGDM- or ECDM-parametrization^{8,10} in the case of uncorrelated or correlated disorder, respectively. The local diffusion coefficient is obtained from the local mobility by using the generalized Einstein equation.²⁷

To solve the 1D drift-diffusion equation, the carrier densities at the electrode planes, n_c , are assumed to be constant and given by the condition of thermal equilibrium between the electrode and the organic layer:

$$n_c = \int_{-\infty}^{\infty} \frac{g(E)}{1 + \exp\left[\frac{E+\Delta}{k_B T}\right]} dE. \quad (5.13)$$

When the local field F_c at the electrode plane, as calculated by the external field V/L and by the Poisson equation, is negative, the local drift contribution of the current is directed towards the electrode. In this case we do not correct for the image potential. However, when the local field at the electrode plane is positive, the local drift contribution of the current is directed away from the injecting electrode. In this case we assume a thermal equilibrium between the electrode and the maximum of the total potential formed by the external potential V/L , the potential as calculated by the Poisson equation, and the image potential. Like in chapter 4 we make use of an image-charge-corrected barrier height, Δ' , in Eq. (5.13), as first suggested by Emtage and O'Dwyer,²⁰

$$\Delta' = \Delta - e\sqrt{\frac{eF_c}{4\pi\epsilon_0\epsilon_r}}, \quad (5.14)$$

where F_c and Δ' are determined self-consistently by using an iterative procedure.

The above approach of taking into account the effect of image charges suffers from a similar double-counting problem as the Master-Equation approach. For the case of Boltzmann statistics and absence of disorder the problem of taking into account the effect of image charges in a consistent way was recently discussed in detail by Genenko *et al.*²² These authors delineate the regions of validity of what they call the ‘‘mean-field’’ (MF) and ‘‘single-particle’’ (SP) approach for varying injection barrier and local field at the electrodes. In the MF approach the effects of image charges are accounted for solely by the boundary conditions for the electrostatic potential at the electrodes, while in the SP approach only the explicit image potential of a single charge close to the electrodes is taken into account. The ‘‘modified mean-field’’ (MMF) approach proposed by these authors corresponds to Eq. (5.14), where the second term in this equation is multiplied by a prefactor that accommodates a smooth switch-on of the image-charge potential when passing the region of validity of the MF approach to the region of validity of the SP approach. The authors argue that the MMF approach more accurately treats injection for intermediate-size injection barriers.

5.3 Results for current-voltage characteristics

In **Fig. 5.1** we display the room-temperature current density J in symmetric single-carrier devices with uncorrelated Gaussian disorder as a function of the applied voltage V , for different values of the injection barrier $\Delta = \Delta_1 = \Delta_2$. The open symbols indicate the results of MC simulations for the case that short-range Coulomb interactions are neglected, which corresponds to setting the cut-off radius R_c of the sphere within which Coulomb interactions are taken into account explicitly equal to zero. The closed symbols correspond to the results of MC simulations for which the short-range contributions of the Coulomb interactions are taken into account ($R_c = 10a$, see Subsection 5.2.1). Results are given for four different values of the injection barrier, $\Delta = 0, 0.33, 0.67,$ and 1 eV. The lattice constant is taken equal to $a = 1.6$ nm, a value found in Ref. 8 from modeling the transport in a hole-only device based on the PPV derivative OC₁C₁₀-PPV (poly[2-methoxy-5-(3',7'-dimethyloctyloxy)-*p*-phenylene vinylene]). We choose $\alpha = 10/a$ in Eq. (5.1) and allow for hops over a maximum distance of $\sqrt{3}a$, as in our calculations with the Master-Equation approach.¹⁵ The four plots in **Fig. 5.1** show results for two different values of the disorder strength, $\sigma = 3k_B T$ (**Figs. 5.1a and c**) and $6k_B T$ (**Figs. 5.1b and d**), which correspond at room temperature to $\sigma = 75$ meV and 150 meV, respectively. Two device thicknesses are taken, $L = 22.4$ (13 layers, **Figs. 5.1c and d**) and 102.4 nm (63 layers, **Figs. 5.1a and b**), which are denoted by “22 nm” (“thin”) and “102 nm” (“thick”), respectively. The lateral grid size is 50×50 sites, which is sufficiently large. The relative dielectric constant ϵ_r is taken equal to 3, like in Ref. 8. The attempt-to-jump frequency, ν_0 , is chosen in such a way that the current density as obtained from the simulations is equal to 1 A/m² for the thick device at $V = 10$ V, for the case that $R_c = 0$. The value of ν_0 is then equal to 3.5×10^{13} s⁻¹ and 1.4×10^{16} s⁻¹ in the case of a device with disorder strength $\sigma = 3k_B T$ and $6k_B T$, respectively. We were not able to obtain sufficiently accurate results for the 102 nm device in the case of a disorder strength $\sigma = 6k_B T$ for the lowest injection barriers and voltages (**Fig. 5.1b**).

We find that the results obtained without taking into account short-range Coulomb interactions are virtually indistinguishable from the results obtained by the Master-Equation calculations of exactly the same devices in chapter 4. Since the Master-Equation is an equation for the time-averaged occupational probabilities of the sites, it is not possible to include Coulomb interactions explicitly in these calculations. Another aspect of the Master-Equation calculations is that correlations between occupational probabilities of sites are not accounted for, whereas such correlations are taken into account in the MC simulations (even if short-range Coulomb interactions are not accounted for). By taking into account correlations between the occupational probabilities of pairs of neighboring sites it was shown that the effect of such correlations on the current is very small.²⁸ This is in agreement with the observed indistinguishability between the Master-Equation results and the MC results without short-range Coulomb interactions. We do not plot the results of the Master-Equation calculations in **Fig. 5.1**, since these essentially coincide with the open symbols.

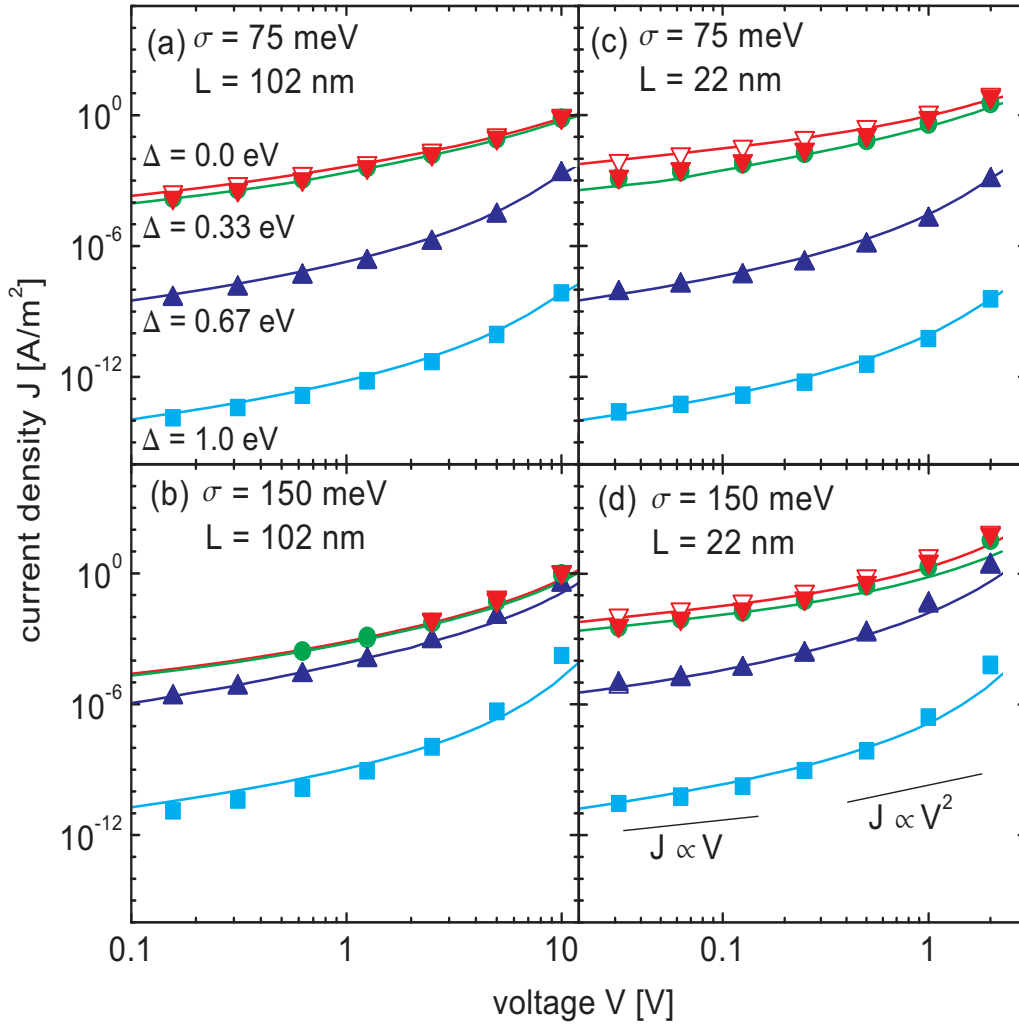


Figure 5.1: Dependence of the current density (J) on the driving voltage (V) for devices with an uncorrelated Gaussian density of states. The devices have thicknesses of $L = 102$ nm and $L = 22$ nm and disorder strengths of $\sigma = 75$ meV and $\sigma = 150$ meV, as indicated in (a)-(d). The results are for room temperature and lattice constant $a = 1.6$ nm. The values used for the attempt-to-jump frequency, ν_0 in Eq. (5.1), are $3.5 \times 10^{13} \text{ s}^{-1}$ for devices with $\sigma = 75$ meV and $1.4 \times 10^{16} \text{ s}^{-1}$ for devices with $\sigma = 150$ meV. These values correspond to a mobility pre-factor μ_0 (as defined in Ref. 8) equal to $4.8 \times 10^{-14} \text{ m}^2/\text{Vs}$ and $1.1 \times 10^{-16} \text{ m}^2/\text{Vs}$, respectively. Closed symbols: results obtained from Monte-Carlo simulations including short-range Coulomb interactions, for different injection barriers Δ : 0 eV (downwards pointing triangles), 0.33 eV (circles), 0.67 eV (upwards pointing triangles), and 1 eV (squares). In (b) no reliable results could be obtained for $\Delta = 0$ and 0.33 eV for the lower voltages. Open symbols: results obtained from Monte-Carlo simulations without short-range Coulomb interactions. Solid lines: results obtained from the 1D continuum drift-diffusion model as explained in the main text. A linear Ohmic dependence $J \propto V$ expected at low voltage is indicated, as well as a quadratic dependence $J \propto V^2$ expected for a space-charge-limited current with a constant mobility.

The drawn lines in **Fig. 5.1** correspond to results obtained from the 1D drift-diffusion model described in Subsection 5.2.2. These results follow the MC results without short-range Coulomb interactions quite accurately, except for the thin device ($L = 22$ nm) with strong disorder ($\sigma = 6k_B T$) at voltages higher than 1 V (**Fig. 5.1d**). These observations are equivalent to those made in chapter 4.

For the lower injection barriers ($\Delta = 0$ and 0.33 eV) the devices are in the space-charge-limited current (SCLC) regime and the current density almost does not depend on the size of the injection barrier. In devices with weak disorder ($\sigma = 3k_B T$) the current density is dependent on the injection barrier for the higher injection barriers ($\Delta = 0.67$ and 1.0 eV). In this case the devices are in the injection-limited current (ILC) regime. For devices with strong disorder ($\sigma = 6k_B T$) the current density is still dominated by space-charge effects at an injection barrier of $\Delta = 0.67$ eV, because the higher disorder leads to a higher carrier density close to the electrodes as compared to the devices with $\sigma = 3k_B T$, due to the larger filling of the states in the tail of the Gaussian DOS. For high injection barriers the current density in the 22 nm and 102 nm devices is almost the same for equal injection barriers if the voltage is scaled with the device thickness.

The most important observation to be made, however, is that for devices without injection barrier ($\Delta = 0$ eV), the current density resulting from the MC simulations with short-range Coulomb interactions is considerably lower than the current density resulting from the simulations without these interactions (and also considerably lower than the 1D drift-diffusion results). For the thin device ($L = 22$ nm) with weak disorder ($\sigma = 3k_B T$) the current density with short-range interactions is at $V = 2$ V about 25% lower than without short-range interactions (**Fig. 5.1c**). This difference increases for lower voltages to a factor of about 6. The difference is less for devices with a higher disorder strength (a factor of about 3 for the thin device with $\sigma = 6k_B T$ at low voltages, see **Fig. 5.1d**) and a larger thickness (a factor of about 2 for the thick device with $\sigma = 3k_B T$ at low voltages, see **Fig. 5.1a**). When short-range Coulomb interactions are taken into account, the current density in devices with no injection barrier is almost the same as the current density in a device with an injection barrier $\Delta = 0.33$ eV. Hence, the effect of taking into account short-range Coulomb interactions is similar to the effect of an increase of the injection barrier. By analyzing the dependence of the current density on the injection barrier we found that at about $\Delta = 0.3$ eV the difference between the MC results with and without short-range Coulomb interactions disappears. This means that for injection barriers higher than about 0.3 eV the density of carriers in the device becomes so low that short-range Coulomb interactions have no influence anymore.

The saturation of the current with decreasing injection barrier at an injection barrier of about 0.3 eV is reminiscent of the pinning of the injection barrier by the transfer of charge from the electrode to the first organic layer under the influence of the image potential, leading to the formation of a dipole layer, as described by Tutiš *et al.*²⁹ In this way these authors try to explain the experimentally observed pinning of the injection barrier for devices of tris(8-hydroxyquinolato)aluminium (Alq₃) at about 0.6 eV with low work-

function metals.³⁰ However, the distance between the electrode and the first organic layer assumed by Tutiš *et al.* is 0.3 nm and hence much smaller than the value of 1.6 nm assumed by us, so that this mechanism of pinning of the injection barrier would occur at much lower injection barriers in our case. We explicitly checked that the difference in charge transfer to the first organic layer for the situation with and without Coulomb interactions is not enough to yield an injection barrier difference of 0.3 eV, so that another mechanism should be responsible for the difference in the current between the situation with and without short-range Coulomb interactions. We will try to identify this mechanism in what follows.

In **Fig. 5.2** we display similar results as in **Fig. 5.1**, but now for the case of dipole-correlated disorder. Correspondingly, the 1D drift-diffusion calculations were performed with the ECDM mobility function.¹⁰ The attempt-to-jump frequency is chosen in a similar way as in Fig. 5.1, leading to $\nu_0 = 9.5 \times 10^{12} \text{ s}^{-1}$ and $4.8 \times 10^{13} \text{ s}^{-1}$ in the case of disorder strengths $\sigma = 3k_B T$ and $6k_B T$, respectively. For the 102 nm device in the case of a disorder strength $\sigma = 6k_B T$ and injection barrier $\Delta = 0$ we could not obtain an accurate result at the lowest voltage (**Fig. 5.2b**).

The agreement between the MC results without short-range Coulomb interactions and the 1D drift-diffusion results is somewhat worse than in the case of uncorrelated disorder, especially for thin devices, high disorder strengths, low applied voltages, and low injection barriers. For low injection barriers ($\Delta = 0$ and 0.33 eV) the current is again space-charge limited. For both disorder strengths $\sigma = 3k_B T$ and $6k_B T$ and at high injection barriers $\Delta = 0.67$ and 1.0 eV the devices are injection-limited.

The difference between the results of the MC simulations with short-range Coulomb interactions and those without short-range Coulomb interactions are now smaller than for the case of uncorrelated disorder. The current density in the thin device with weak disorder (**Fig. 5.2c**) with short-range Coulomb interactions is at $V = 2 \text{ V}$ only about 10% lower than without short-range Coulomb interactions. This difference increases for lower voltages to a factor of about 2. The difference is almost negligible in the thick device (**Figs. 5.2a and b**) and at high disorder strength (**Fig. 5.2d**). We note that the difference between the current-voltage characteristics with and without short range Coulomb interactions occurs at very small injection barriers, as shown in **Fig. 5.1** for the case $\Delta = 0$. The effect occurs thus in the MF regime (within the terminology used by Genenko *et al.*²²), within which the electric field is directed towards the electrode. The MMF approach of Genenko *et al.*, which applies to intermediate energy barriers resulting in a positive field, is then inapplicable. At the non-zero injection barriers that we studied the double-counting error made in the Master-Equation approach and in the 1D drift-diffusion modeling apparently does not lead to any significant error.

An important conclusion is that the current with short-range Coulomb interactions included is in our simulations always *smaller* than without short-range Coulomb interactions. This conclusion appears to be at odds with the conclusion of Zhou *et al.*³¹ that Coulomb interactions decrease the mobility at low disorder strength but increase the mobility at

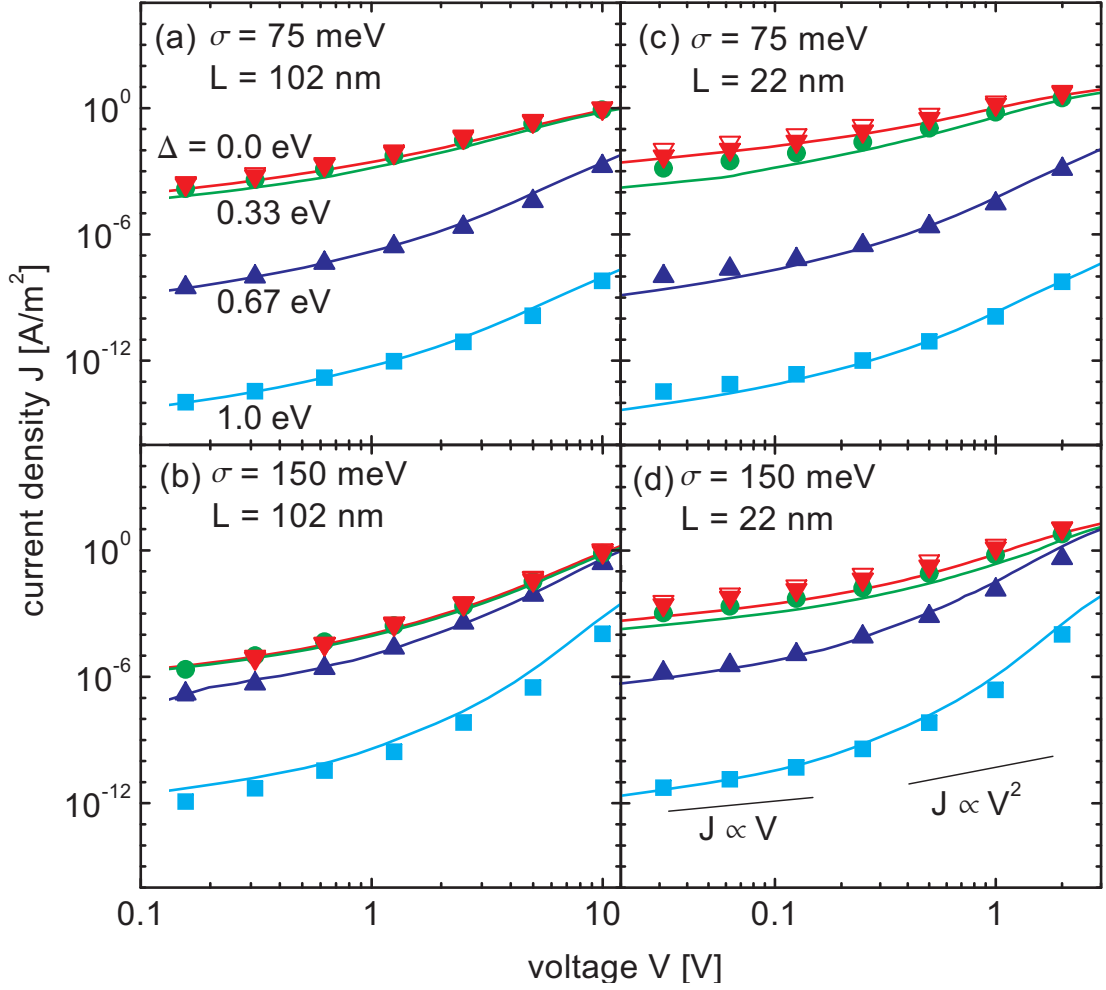


Figure 5.2: The same as in Fig. 5.1, but for correlated disorder. The values used for the attempt-to-jump frequency, ν_0 in Eq. (5.1), are $9.5 \times 10^{12} \text{ s}^{-1}$ for devices with $\sigma = 75$ meV and $4.8 \times 10^{13} \text{ s}^{-1}$ for devices with $\sigma = 150$ meV. These values correspond to a mobility pre-factor μ_0 (as defined in Ref. 10) equal to $2.4 \times 10^{-14} \text{ m}^2/\text{Vs}$ and 2.4×10^{-17} , respectively. In (b) no reliable results could be obtained for $\Delta = 0$ at the lowest voltage.

high disorder strength. However, this conclusion was drawn from results obtained at a rather large electric field of $F = 4kT/ea$, a field strength that is only reached at the highest voltages in **Figs. 1 and 2**. The reduction of the current found by us is compatible with the theoretical prediction of a Coulomb gap opening up around the Fermi energy in the DOS of a system of interacting localized charges,^{32,33} which leads to a reduction of the carrier mobility at low electric field.

5.4 Effects of short-range Coulomb interactions on the three-dimensional current distributions

In this section we show the 3D current distributions in the devices with and without taking into account short-range Coulomb interactions. From the structure of these distributions we will try to rationalize the trends in the effects of short-range interactions on the total current observed in the previous section. **Fig. 5.3** shows the time-averaged 3D current distributions, calculated with Eq. (5.10), at room temperature of a thin device of $L = 22$ nm for uncorrelated disorder with a disorder strength of $\sigma = 3k_B T$ (**Figs. 5.3a and b**) and $\sigma = 6k_B T$ (**Figs. 5.3c-f**) at an applied voltage of $V = 0.5$ V. **Figs. 5.3a-d** show the results without an injection barrier, while **Figs. 5.3e and f** show the results for $\sigma = 6k_B T$ with an injection barrier of $\Delta = 1$ eV. In **Figs. 5.3a, c, and e** short-range Coulomb interactions have been taken into account, while these have been omitted in **Figs. 5.3b, d, and f**. Apart from a factor of two difference in the energies between $\sigma = 3k_B T$ and $\sigma = 6k_B T$, exactly the same disorder configuration of the random energies of the organic sites has been taken in **Figs. 5.3a-f**. **Fig. 5.4** shows the same results for correlated disorder.

In the case of vanishing injection barrier $\Delta = 0$ there is a significant effect of short-range Coulomb interactions on the current distributions (compare **Figs. 5.3a and b**, **Figs. 5.3c and d**, **Figs. 5.4a and b**, and **Figs. 5.4c and d**). As already noted in chapter 4 the energetic disorder leads to a strong filamentary structure of the current distribution, because of the percolative character of the charge transport. We observe that when short-range Coulomb interactions are taken into account, the current distribution is changed and the filamentary character of this distribution is reduced (compare in particular **Fig. 5.3c** with **Fig. 5.3d** and **Fig. 5.4c** with **Fig. 5.4d**). The reason for this is that the short-range Coulomb interactions prevent carriers from always following the most favorable percolating path from one electrode to the other, since a trapped carrier close to a percolating path may temporarily block that path by repelling other carriers. This leads to the reduction of the current as described in the previous section. We remark that with growing disorder strength the contribution of the Coulomb interactions ($e\Phi_{\text{interact},i}$) to the on-site energy of a charge as compared to the random contribution ($E_{\text{rand},i}$) becomes less important. Conversely, this means that, although the filamentary structure for $\sigma = 3k_B T$ is less pronounced than for $\sigma = 6k_B T$, the relative effect of short-range Coulomb interactions as compared to the energetic disorder is larger. This explains the relatively stronger reduction of the current

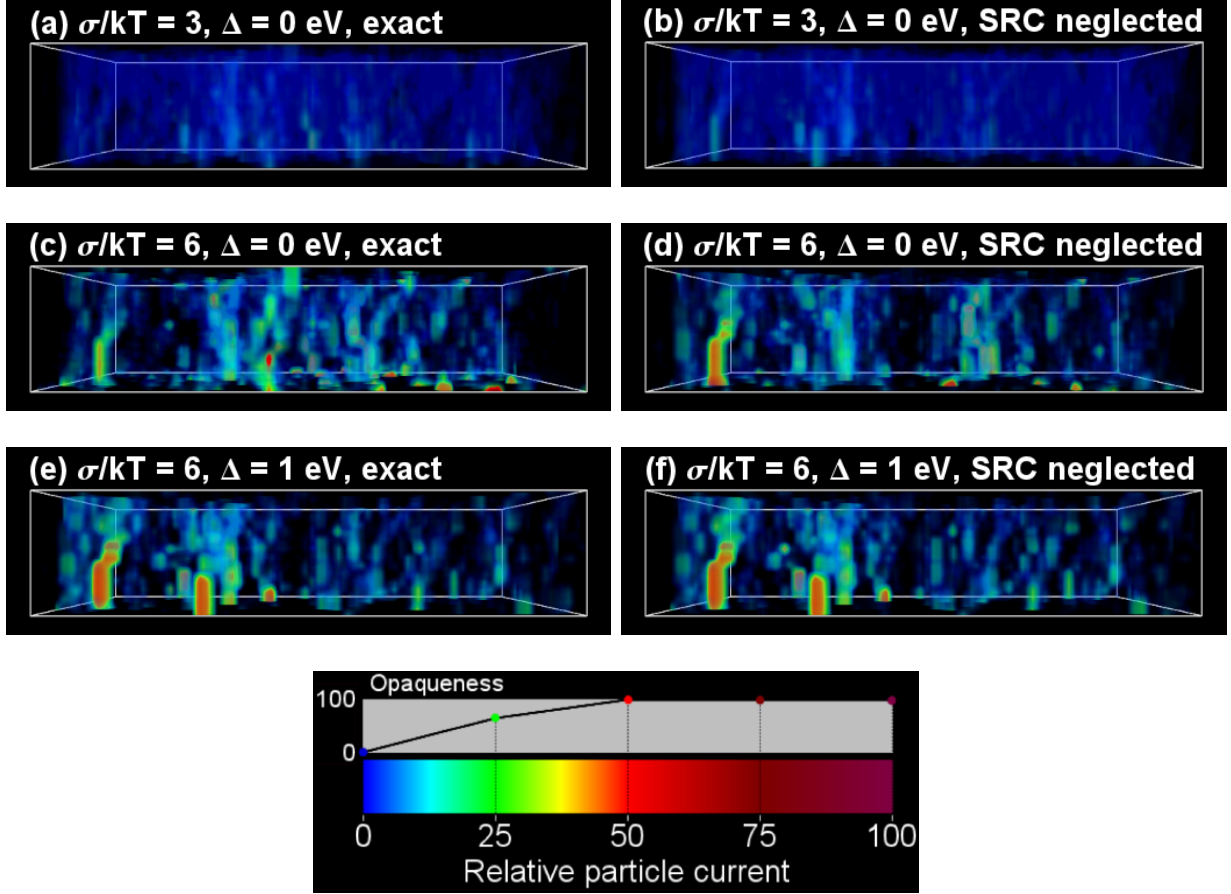


Figure 5.3: Three-dimensional representation of the relative local current density in the direction of the applied field, given by $J_{\text{rel},i} = J_i/J_{\text{av}}$, with J_i the absolute local current density given by Eq. (5.10) and J_{av} the average local current density in the device. The displayed results are for devices with uncorrelated disorder, device thickness $L = 22$ nm, driving voltage $V = 0.5$ V, room temperature, and lattice constant $a = 1.6$ nm. In all representations (a)-(f) the device is viewed from the side with the injecting electrode at the bottom. The energetic disorder configurations of the organic sites are all the same, apart from a factor two difference in energies between $\sigma = 75$ and $\sigma = 150$ meV. In (a), (c), and (e) short-range Coulomb (SRC) interactions have been included, while these are omitted in (b), (d), and (f). The local current density is coded with a color and transparency, with the coding scheme indicated at the bottom. The lateral grid size used is 50×50 sites. The boundaries of the device are depicted by a white bounding box.

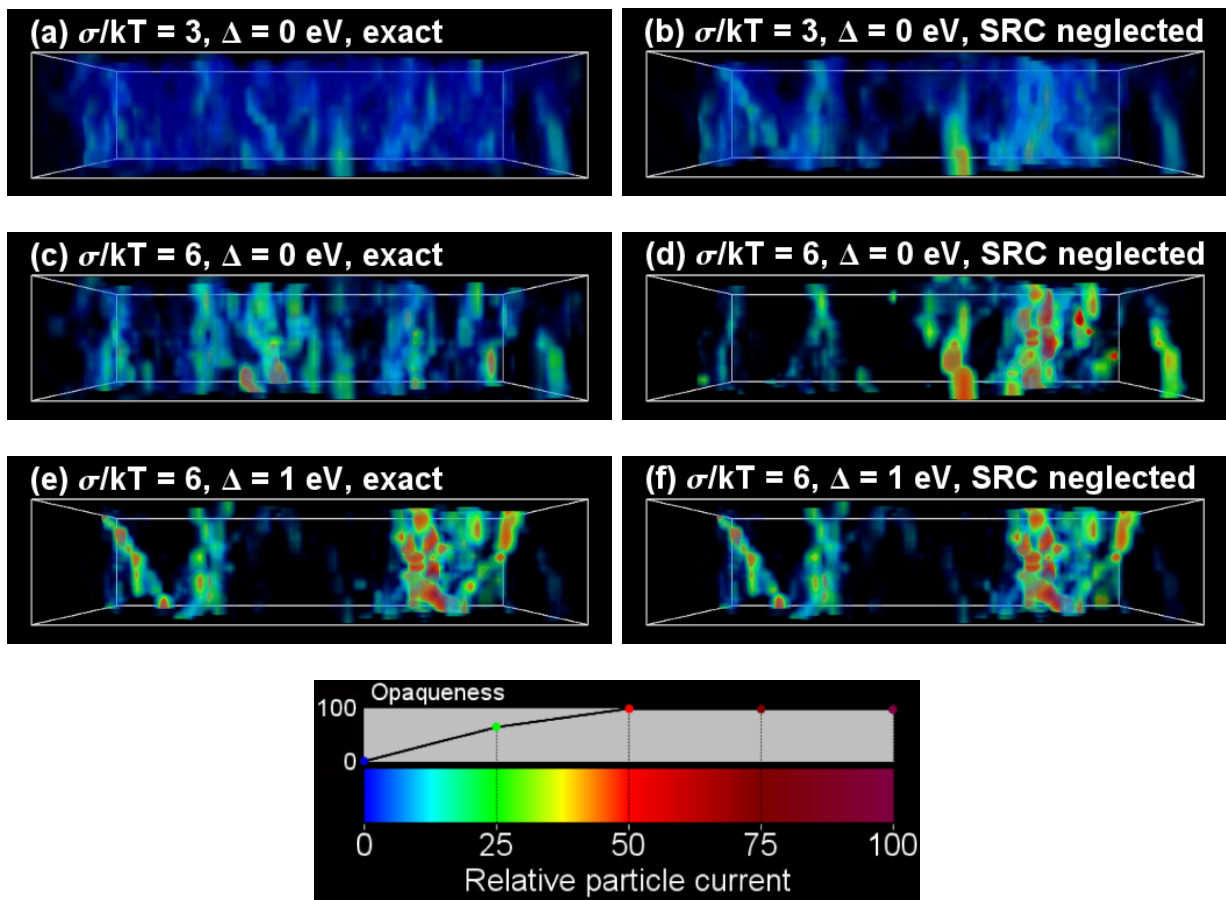


Figure 5.4: The same as in Fig. 5.3, but for correlated disorder.

by short-range Coulomb interactions for weaker disorder found in the previous section.

On the other hand, in the case of an injection barrier of $\Delta = 1.0$ eV there is no observable effect of short-range Coulomb interactions on the current distributions (compare **Figs. 3e and f** and **Figs. 4e and f**), in line with the absence of an effect on the current-voltage characteristics in **Figs. 1 and 2**. The absence of an effect of short-range Coulomb interactions on the current distribution for this relatively high injection barrier is related to the very low carrier density in the device. We note that for an applied voltage of 2 V we could for $\sigma = 6k_B T$ very accurately reproduce the current distribution obtained with the Master-Equation approach shown in figure 4.3c in chapter 4. for the case of uncorrelated disorder, using the same disorder configuration as in that work. This is in line with the observation made in the previous section that the current-voltage characteristics obtained from the MC simulations without short-range Coulomb interactions are indistinguishable from these obtained from the Master-Equation calculations in chapter 4. Although we do not show the current distributions for the case of $\sigma = 3k_B T$ and an injection barrier of $\Delta = 1.0$ eV, these conclusions also hold for that case.

For the case of correlated disorder we observe that the filamentary structure of the current is different than for uncorrelated disorder. The current filaments are now typically broader than for uncorrelated disorder (this is in particular clearly visible in **Figs. 4d-f**). The reason is that due to the spatial energetic correlation the percolating paths acquire a width that is broader than the single lattice spacing typical for the case of uncorrelated disorder. As a consequence, the blocking effect caused by short-range Coulomb interactions is less effective, since carriers have a broad choice of well conducting spatially correlated pathways. This explains the observation in the previous section that the effect of short-range Coulomb interactions on the total current is smaller than in the case of uncorrelated disorder.

5.5 Summary and conclusions

By performing three-dimensional (3D) Monte-Carlo (MC) simulations we have studied single-carrier transport in devices consisting of an organic semiconductor sandwiched in between two metallic electrodes, for the cases of uncorrelated Gaussian energetic disorder in the organic semiconductor as well as correlated Gaussian energetic disorder caused by the electrostatic field of random dipoles. In particular, the effects of Coulomb interactions between the carriers were studied. Up to now, in device modeling studies only the long-range effects of Coulomb interactions have been included through the space-charge potential. We studied the situations with and without inclusion of short-range Coulomb interactions. We also varied the injection barrier between the electrodes and the organic semiconductor. The effects of image charges in the electrodes were fully taken into account.

For the case of uncorrelated disorder we found that with an injection barrier of about 0.3 eV

or higher, for the devices we studied, it is not necessary to include the short-range Coulomb interactions, because of the low carrier density in the devices. Our results for the current-voltage characteristics are then in accurate agreement with the calculations as shown in chapter 4 of the same devices with a Master-Equation approach, in which the Coulomb interactions between the charges were taken into account in a layer-averaged way. This also means that the way we have taken into account image charges in chapter 4, which suffers from a double-counting problem due to the fact that image charges have also been taken into account in a layer-averaged way via the space charge, does not lead to significant errors for these injection barriers. Our results for the current are then also in good agreement with one-dimensional (1D) drift-diffusion calculations with a mobility function based on the Extended Gaussian Disorder Model (EGDM),⁸ in which the dependence of the mobility on temperature, electric field, and carrier density is taken into account.

If the injection barrier in the case of uncorrelated disorder is smaller than 0.3 eV, however, the inclusion of short-range Coulomb interactions leads to a significant reduction of the current. By analyzing the 3D current distribution we attributed this to the fact that the short-range Coulomb interactions change the filamentary structure of this distribution, where favorable percolating pathways for the current are partially blocked. The reduction of the current is larger for smaller disorder strength due to the relatively larger importance of Coulomb interactions in that case. The difference between current-voltage characteristics with and without taking in account short-range Coulomb interactions should not be attributed to the double-counting problem because the image-charge contribution to the potential then does not appear in the 1D drift-diffusion calculations.

For the case of correlated disorder we found similar results, with the important difference that the short-range Coulomb interactions lead to a smaller reduction of the current at vanishing injection barrier than for uncorrelated disorder. Due to the spatial energetic correlation the current filaments are broader and hence the blocking effect of the short-range Coulomb interactions is smaller. For not too small injection barriers we found a fair agreement between our 3D MC results for the current and 1D drift-diffusion calculations with a mobility function based on the Extended Correlated Disorder Model.¹⁰

The relevance of the present work for the modeling of organic light-emitting diodes is that the conventional drift-diffusion modeling approach can be applied in the transport for not too small injection barriers, when the effects of short-range Coulomb interactions can be neglected. In the case of small injection barriers the effects of short-range Coulomb interactions become important, as demonstrated in the present work, but there is presently no systematic and simple theory to include these effects. We note that we have recently shown that in order to properly describe electron-hole recombination in double-carrier devices it is also necessary to take into account the effects of short-range interactions (as described in the next chapter).³⁴ If these interactions are included in the mobilities in a double-carrier situation, an accurate description of the recombination rate is found when these mobilities are used in the conventional Langevin expression for this rate, as shown in the next chapter. It would therefore be highly desirable to develop a systematic theory

for including short-range Coulomb effects on charge-carrier mobilities in disordered organic semiconductors.

References

- [1] Pautmeier, L.; Richert, R.; Bäessler, H. *Synth. Met.* **1990**, *37*, 271.
- [2] Bäessler, H. *Phys. Stat. Sol. (b)* **1993**, *175*, 15.
- [3] Gartstein, Y.; Conwell, E. *Chem. Phys. Lett.* **1995**, *245*, 351.
- [4] Dunlap, D.; Parris, P.; Kenkre, V. *Phys. Rev. Lett.* **1996**, *77*, 542.
- [5] Novikov, S.; Dunlap, D.; Kenkre, V.; Parris, P.; Vannikov, A. *Phys. Rev. Lett.* **1998**, *81*, 4472.
- [6] Yu, Z.; Smith, D.; Saxena, A.; Martin, R.; Bishop, A. *Phys. Rev. Lett.* **2000**, *84*, 721.
- [7] Roichman, Y.; Tessler, N. *Synth. Met.* **2003**, *135*, 443.
- [8] Pasveer, W.; Cottaar, J.; Tanase, C.; Coehoorn, R.; Bobbert, P.; Blom, P.; de Leeuw, D.; Michels, M. *Phys. Rev. Lett.* **2005**, *94*, 206601.
- [9] van Mensfoort, S.; Vulto, S.; Janssen, R.; Coehoorn, R. *Phys. Rev. B* **2008**, *78*, 085208.
- [10] Bouhassoune, M.; van Mensfoort, S.; Bobbert, P.; Coehoorn, R. *Org. Electron.* **2009**, *10*, 437.
- [11] de Vries, R.; van Mensfoort, S.; Shabro, V.; Vulto, S.; Janssen, R.; Coehoorn, R. *Appl. Phys. Lett.* **2009**, *94*, 163307.
- [12] van Mensfoort, S. L. M.; Shabro, V.; de Vries, R. J.; Janssen, R. A. J.; Coehoorn, R. *J. Appl. Phys.* **2010**, *107*, 113710.
- [13] van Mensfoort, S. L. M.; de Vries, R. J.; Shabro, V.; Loebl, H.; Janssen, R.; Coehoorn, R. *Org. Electron.* **2010**, *11*, 1408.
- [14] van Mensfoort, S.; Coehoorn, R. *Phys. Rev. B* **2008**, *78*, 085207.
- [15] van der Holst, J.; Uijtewaal, M.; Ramachandhran, B.; Coehoorn, R.; Bobbert, P.; de Wijs, G.; de Groot, R. *Phys. Rev. B* **2009**, *79*, 085203.
- [16] Yu, Z.; Smith, D.; Saxena, A.; Martin, R.; Bishop, A. *Phys. Rev. B* **2001**, *63*, 085202.
- [17] Tutiš, E.; Batistić, I.; Berner, D. *Phys. Rev. B* **2004**, *70*, 161202(R).

-
- [18] Meisel, K.; Pasveer, W.; Cottaar, J.; Tanase, C.; Coehoorn, R.; Bobbert, P.; Blom, P.; de Leeuw, D.; Michels, M. *Phys. Stat. Sol. (c)* **2006**, *3*, 267.
- [19] Kwiatkowski, J. J.; Nelson, J.; Li, H.; Bredas, J. L.; Wenzel, W.; Lennartz, C. *Phys. Chem. Chem. Phys.* **2008**, *10*, 1852.
- [20] Emtage, P.; O'Dwyer, J. *Phys. Rev. Lett.* **1966**, *16*, 356.
- [21] Burin, A.; Ratner, M. *J. Chem. Phys.* **2000**, *113*, 3941.
- [22] Genenko, Y.; Yampolskii, S.; Melzer, C.; Stegmaier, K.; von Seggern, H. *Phys. Rev. B* **2010**, *81*, 125310.
- [23] Miller, A.; Abrahams, E. *Phys. Rev.* **1960**, *120*, 745.
- [24] Novikov, S.; Vannikov, A. *JETP* **1994**, *79*, 482.
- [25] Young, R. *Philos. Mag. B* **1995**, *72*, 435.
- [26] Novikov, S.; Vannikov, A. *J. Phys. Chem.* **1995**, *99*, 14573.
- [27] Roichman, Y.; Tessler, N. *Appl. Phys. Lett.* **2002**, *80*, 1948.
- [28] Cottaar, J.; Bobbert, P. *Phys. Rev. B* **2006**, *74*, 115204.
- [29] Tutiš, E.; Bussac, M.; Zuppiroli, L. *Appl. Phys. Lett.* **1999**, *75*, 3880.
- [30] Campbell, I.; Smith, D. *Appl. Phys. Lett.* **1999**, *74*, 561.
- [31] Zhou, J.; Zhou, Y.; Zhao, J.; Wu, C.; Ding, X.; Hou, X. *Phys. Rev. B* **2007**, *75*, 153201.
- [32] Pollak, M. *Discuss. Faraday Soc.* **1970**, *50*, 13.
- [33] Efros, A.; Shklovskii, B. *J. Phys. C: Solid State Phys.* **1976**, *9*, 2021.
- [34] van der Holst, J.; van Oost, F.; Coehoorn, R.; Bobbert, P. *Phys. Rev. B* **2009**, *80*, 235202.

Chapter 6

Electron-hole recombination in disordered organic semiconductors: validity of the Langevin formula

ABSTRACT

Accurate modeling of electron-hole recombination in organic light-emitting diodes (OLEDs) is essential for developing a complete description of their functioning. Traditionally, the recombination rate is described by the Langevin formula, with a proportionality factor equal to the sum of the electron and hole mobilities. In the disordered organic semiconductors used in OLEDs these mobilities have been shown to depend strongly on the carrier densities and on the electric field. Moreover, the energetic disorder leads to percolating pathways for the electron and hole current, which may or may not be correlated. To answer the question whether the Langevin formula is still valid under such circumstances we perform Monte-Carlo simulations of the recombination rate for Gaussian energetic disorder. We vary the disorder energy, the temperature, the densities and mobility ratio of electrons and holes, the electric field, and the type of correlation between the electron and hole energies. We find that at zero electric field the Langevin formula is surprisingly well obeyed, provided that a change of the charge-carrier mobilities due to the presence of charge carriers of the opposite type is taken into account. Deviations from the Langevin formula at finite electric field are small at the field scale relevant for OLED modeling.¹

¹The contents of this chapter are based on work that has been published: J.J.M. van der Holst, F.W.A. van Oost, R. Coehoorn, P.A. Bobbert, *Physical Review B: Condensed Matter* **2010**, *Submitted*

6.1 Introduction

Organic light-emitting diodes (OLEDs) are very promising efficient light sources in display and lighting applications. Commercial OLED pixelated displays as well as large-area OLED white-light sources are presently entering the market. An essential process in OLEDs is the recombination of an electron and a hole, leading to the emission of a photon. In the emitting organic semiconductor the electrons and holes move towards each other under the influence of an external electric field and their mutual attractive Coulomb interaction. The rate of recombination, R , is defined as the total number of electron-hole recombination events per second and per unit volume. Already in 1903, Langevin^{1,2} gave an expression for this recombination rate:

$$R_{\text{Lan}} = \frac{e(\mu_e + \mu_h)}{\epsilon_r \epsilon_0} n_e n_h \equiv \gamma_{\text{Lan}} n_e n_h, \quad (6.1)$$

where e is the unit charge, n_e and n_h the electron and hole density, and μ_e and μ_h the electron and hole mobility, respectively; ϵ_0 is the vacuum permeability, ϵ_r the relative dielectric constant of the semiconductor, and γ_{Lan} the Langevin bimolecular recombination rate factor.

One of the underlying assumptions in the derivation of this expression is that the mean free path of the charge carriers λ is much smaller than the thermal capture radius $r_c = e^2/(4\pi\epsilon_r\epsilon_0k_B T)$, where T is the temperature and k_B Boltzmann's constant. For the disordered organic semiconductors used in OLEDs charge transport takes place by hopping between molecules or conjugated segments of a π -conjugated polymer, which we will call "sites", and the mean free path is of the order of the inter-site distance $a \approx 1\text{-}2$ nm. At room temperature and with a relative dielectric constant $\epsilon_r \approx 3$, typical for organic semiconductors, the thermal capture radius is $r_c \approx 18.5$ nm. Hence, the assumption $\lambda \ll r_c$ is valid.

Another assumption made in deriving Eq. (6.1) is that charge-carrier transport occurs homogeneously throughout the semiconductor. This is, however, in general not the case. Due to the percolative nature of charge transport in energetically disordered organic semiconductors, the current distribution has a highly inhomogeneous filamentary structure, with differences in local current densities that can vary over many orders of magnitude.³⁻⁷ This raises the question whether Eq. (6.1) is still valid under such conditions. Another issue that plays a role in this context is the possible correlation between the on-site energies of holes and electrons. In the case of correlation between on-site electron and hole energies, the current filaments of the electrons and holes overlap. One would then intuitively expect a larger recombination rate than in the case of uncorrelated or even anti-correlated energies. Correlation between electron and hole energies occurs when the energetic disorder is caused by fluctuations in the local polarizability of the semiconductor or by differences in the length of conjugated segments. Anti-correlation between electron and hole energies occurs when the disorder is caused by fluctuations in the local electrostatic potential. In

this chapter we will study both extremes of perfect correlation and perfect anti-correlation. In reality, the situation will be intermediate.

A further complication arises when the recombination occurs in the presence of an external electric field, because the electron and hole mobilities have an electric-field dependence. Moreover, it has become clear in recent years that under typical operating conditions of OLEDs the dependence of the mobilities on the charge-carrier densities is even more important than their dependence on the electric field.^{8,9} This raises the question whether it is possible to use the Langevin expression Eq. (6.1) by including these dependencies in the mobilities occurring in the expression.

Giving an analytical description of recombination under such complicating circumstances is impossible and one therefore has to resort to numerical methods. Various aspects of recombination in disordered semiconductors have been studied in the 1990s by using Monte-Carlo (MC) simulations.¹⁰⁻¹² The on-site energies in these simulations are randomly drawn from a Gaussian distribution. Using Miller-Abrahams hopping rates,¹³ Albrecht and Bässler^{10,11} have calculated the MC recombination cross-section and from that the bimolecular recombination rate factor γ . They find that the ratio between γ and γ_{Lan} from Eq. (6.1) is almost independent of temperature, but increases with electric field. Gartstein *et al.*¹² have calculated the ratio between the MC and the Langevin recombination cross-section. At room temperature, they find a slight decrease followed by an increase of this ratio with increasing electric field for Miller-Abrahams hopping rates and a decrease for polaronic hopping rates.^{14,15} These authors find a weak dependence of this ratio on temperature at low electric field, developing into a considerable temperature-dependence at high electric field. Both these MC studies consider the recombination of only two carriers, where one of the carriers is fixed at a particular site in a simulation box and the other carrier is released at a random site located up-field in a plane orthogonal to the electric field. Therefore, these simulations correspond to the case of vanishing electron and hole densities.

More involved MC simulations of recombination were very recently performed by Groves and Greenham.¹⁶ In these simulations both electrons and holes are allowed to hop with polaronic hopping rates, in the presence of an external electric field, and the density of electrons and holes is varied. Like in the previous MC simulations¹⁰⁻¹² the on-site energies are drawn from a Gaussian distribution. Perfect correlation between hole and electron energies at a site is assumed. After recombination of an electron-hole pair, the electron and hole are reintroduced into the simulation box at random sites, guaranteeing constant prescribed charge-carrier densities. The ratio R/R_{Lan} is studied, where the charge-carrier mobilities in the Langevin expression Eq. (6.1) are determined by separate MC simulations of only one type of charge carrier at the same density as in the MC simulations with recombination. Considerable deviations (up to about 40%) from the Langevin expression are found.¹⁶ Effects of anisotropy and blends of electron- and hole-transporting materials are also considered in that work, but these will not be considered in the present work, which will focus on isotropic and homogeneous recombination.

Accurate modeling of electronic processes in OLEDs is of paramount importance for their further development and optimization. Regarding the modeling of the injection and transport in single-carrier devices much progress has been made in recent years. Bässler proposed that transport in disordered organic semiconductors can be described by hopping of charge carriers between sites with a Gaussian energetic disorder.¹⁷ This model became known as the "Gaussian Disorder Model" (GDM). The inclusion of the dependence of the charge-carrier mobility on the charge-carrier density in this model^{9,18} has led to the "Extended Gaussian Disorder Model" (EGDM). It turns out that the EGDM can be used in efficient one-dimensional (1D) device modeling studies that can quite accurately describe the current-voltage characteristics of hole-only devices of derivatives of the well-known conjugated polymers poly(*p*-phenylenevinylene)^{9,19} (PPV) and polyfluorene.²⁰ In the previous two chapters, we showed results of complete three-dimensional (3D) single-carrier device simulations which were done by solving the master equation for the occupational probabilities of the sites in such a device.⁷ The effects of an injection barrier, of image charges, and of space charge were included. We demonstrated that current-voltage characteristics are obtained that are in very good agreement with those obtained with a 1D drift-diffusion model,²¹ with injection included by a relatively simple approach based on work of Emtage and O'Dwyer.²²

We remark that it has been argued by several authors²³⁻²⁵ that the energetic disorder in organic semiconductors should be spatially correlated. One of the situations for which this would occur is when the energetic disorder is caused by random dipolar fields. Such correlation leads to a strongly enhanced electric-field dependence of the mobility.²³⁻²⁵ In combination with the dependency on the charge-carrier density this leads to what we call the "Extended Correlated Disorder Model" (ECDM). Comparison of ECDM and EGDM modeling of current-voltage characteristics of hole-only devices of a derivative of PPV¹⁹ and of a polyfluorene-based co-polymer²⁶ has led to the conclusion that the inter-site distance as found from a fit with the EGDM (with spatially uncorrelated disorder) is more realistic than that found from a fit with the ECDM. Therefore, we will consider in this work spatially uncorrelated disorder.

Accurate modeling of double-carrier devices additionally requires an adequate description of the recombination rate in such devices. Obviously, it would be attractive to have available an efficient, yet sufficiently precise way of including recombination in a 1D device model, instead of needing to calculate the recombination rate for every specific situation with time-consuming 3D MC simulations. One of the objectives of the present work is to make a first step into this direction. We will investigate the recombination process with MC simulations for an isotropic and homogeneous organic semiconductor, varying the disorder energy of the Gaussian disorder, the temperature, the densities of electrons and holes, the mobility ratio of electrons and holes, the electric field, and the type of correlation between electron and hole energies. As in the MC studies discussed above^{10-12,16} we will study the validity of the Langevin expression Eq. (6.1). Since Miller-Abrahams hopping rates have been used in the EGDM modeling,^{9,18} we will also use these hopping rates in our

study. Like Groves and Greenham,¹⁶ we find rather large deviations from the Langevin expression if the electron and hole mobilities in the Langevin expression are taken to be those of the electrons and holes separately at their respective densities. On the other hand, we find that the Langevin expression describes our MC recombination rates surprisingly well if the electron and hole mobilities are taken to be those in exactly the double-carrier situation studied. In the case of an externally applied electric field we find deviations from the Langevin expression that can be attributed to the electric-field dependence of the mobilities. However, these deviations are small for the electric-field strengths relevant for OLEDs. All these findings can open the way to efficient and accurate modeling of double-carrier devices.

This chapter is built up as follows. In the next section we discuss our Monte-Carlo procedure. In Section 6.3 we present various results of our Monte-Carlo studies. In Section 6.4 we discuss our results and present our conclusions.

6.2 Monte-Carlo method

We model the localized electronic states in the organic semiconductor by a three-dimensional cubic lattice with lattice constant a . Periodic boundary conditions are taken in all three Cartesian directions. We assume that the hopping of charge carriers from one localized state to another is a thermally assisted tunneling process with coupling to a bath of acoustical phonons. The hopping rate from site i to site j is then of the Miller-Abrahams form¹³

$$W_{\mathbf{i}\mathbf{j},q} = \nu_{0,q} \exp \left[-2\alpha |\mathbf{R}_{\mathbf{i}\mathbf{j}}| - \frac{E_{\mathbf{j},q} - E_{\mathbf{i},q}}{k_{\text{B}}T} \right], \quad \text{for } E_{\mathbf{j},q} \geq E_{\mathbf{i},q}, \quad (6.2a)$$

$$W_{\mathbf{i}\mathbf{j},q} = \nu_{0,q} \exp [-2\alpha |\mathbf{R}_{\mathbf{i}\mathbf{j}}|], \quad \text{for } E_{\mathbf{j},q} < E_{\mathbf{i},q}, \quad (6.2b)$$

with q the charge of the hopping charge carrier ($q = -e$ for electrons and $q = e$ for holes), $\nu_{0,q}$ the intrinsic attempt-to-jump frequency of carrier q , α the inverse localization length of the localized wave functions, and $|\mathbf{R}_{\mathbf{i}\mathbf{j}}| \equiv a|\mathbf{i} - \mathbf{j}|$ the distance between sites \mathbf{i} and \mathbf{j} . The energy $E_{\mathbf{i},q}$ of charge q at site \mathbf{i} contains a random contribution, a contribution $eFR_{\mathbf{i}\mathbf{j},x}$ due to a field F applied in the x -direction, and a contribution due to the interaction with all the other charges in the system. We take $\alpha = 10/a$ and allow hopping to the 26 nearest neighbors, which is a good approximation for derivatives of PPV at room temperature.⁹

The random contribution to the energy $E_{\mathbf{i},q}$ is drawn from a Gaussian density of states (DOS):

$$g(E) = \frac{1}{\sqrt{2\pi}\sigma a^3} e^{-E^2/2\sigma^2}. \quad (6.3)$$

The disorder energy σ is the width of the Gaussian DOS and is in this work taken equal for electrons and holes. As explained in the Introduction, we distinguish two cases for

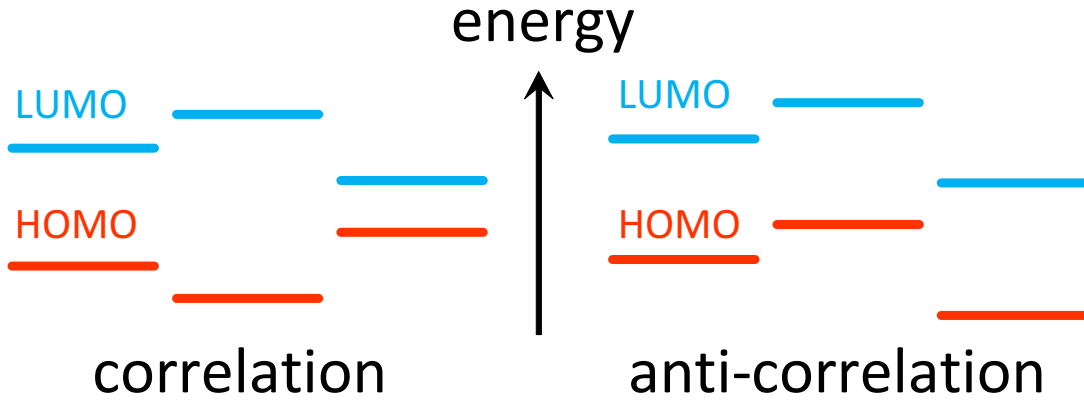


Figure 6.1: The different types of correlation between on-site electron and hole energies considered in this work, reflected in the energies for the LUMO (lowest unoccupied molecular orbital) and HOMO (highest unoccupied molecular orbital). Left/right: correlated/anti-correlated electron and hole energies.

the correlation between on-site electron and hole energies: (1) perfect correlation and (2) perfect anti-correlation; see **Fig. 6.1**. In case (1) the random part of the hole on-site energy is taken equal to that of the electron on-site energy, while in case (2) the random part of the hole on-site energy is taken opposite to that of the electron on-site energy. Therefore, it is energetically advantageous for an electron and a hole to reside on the same site in case (1), while in case (2) this is disadvantageous.

The energy $E_{i,q}$ also contains the Coulomb interaction energy U_i with all other charges. For practical reasons we use a finite-range variant of the Coulomb potential:

$$f_c(|\mathbf{R}_{ij}|) = \begin{cases} \frac{1}{4\pi\epsilon_r\epsilon_0} \left(\frac{1}{|\mathbf{R}_{ij}|} - \frac{1}{R_c} \right), & 0 < |\mathbf{R}_{ij}| \leq R_c, \\ 0, & |\mathbf{R}_{ij}| > R_c, \end{cases} \quad (6.4)$$

with R_c a cut-off radius. We will always use a value of R_c that is large enough to have no influence on the final results. The interaction energy U_i is taken as

$$U_i = \sum_{j \neq i} q_i q_j f_c(|\mathbf{R}_{ij}|), \quad (6.5)$$

where q_i and q_j are the charges of the interacting carriers at sites \mathbf{i} and \mathbf{j} ($q_j = 0$ if there is no charge at site \mathbf{j}). We assume that due to strong on-site Coulomb repulsion the presence of two equal charges at a site is not allowed.

When an electron and a hole are on neighboring sites, the hopping of the hole to the electron or vice versa is always assumed to be downwards in energy, such that the hopping rate will be given by Eq. (6.2b). After such a process, the electron and hole are removed from the

system and reintroduced randomly on empty sites according to an equilibrium distribution determined by the random contribution to the site energies (excluding the contribution from the electric field and the Coulomb interaction with other charges). Reintroduction of the electron and hole guarantees that the electron and hole densities are kept fixed. We note that our method of reintroduction is slightly different from that of Groves and Greenham, who choose random empty sites for reintroducing the electron and hole and then take new random energies of these sites according to the equilibrium density of occupied states.¹⁶ Both methods of reintroduction are of course artificial. In a real OLED, electrons and holes approach each other from opposite electrodes. One can argue what method of reintroduction gives the most accurate description of the real situation. An alternative would be reintroduction of the electron and hole at completely randomly chosen sites. If the electrons and holes are energetically relaxed before they recombine, which should be the case for sufficiently low densities of electrons and holes, the precise way of reintroduction should become irrelevant. We will come back to this issue in the next section and show that our main conclusion is not affected by the choice of the reintroduction procedure.

Our simulations proceed as follows. First, a cubic simulation box is filled with a prescribed number of electrons and an equal number of holes. After that, hops of electrons and holes are chosen with weights determined by the hopping rates Eq. (6.2). A hopping time is chosen from an exponential distribution with an inverse decay time equal to the sum of all possible hopping rates. After a sufficiently long equilibration time, counting of the number of recombination events starts. This proceeds until a sufficiently accurate result for the recombination rate is obtained.

We use two different methods of calculating carrier mobilities. In the first method, which corresponds to that of Groves and Greenham,¹⁶ we fill our simulation box with exactly the same number of charge carriers of one type as we have in the double-carrier simulation. We then apply a small electric field (or apply the same field as in the double-carrier simulation) and obtain the current by counting the number of hops in the field direction. From the current, we straightforwardly obtain the mobilities μ_{uni} of each carrier type in this "unipolar" system. We remark that the results obtained in this way are equivalent to those of Zhou *et al.*²⁷ In the second method, we take our double-carrier simulation, apply a small electric field (or apply the same field as in the double-carrier simulation) and calculate the current contribution of each carrier type separately. Accordingly, we obtain μ_{bi} of each carrier type in this "bipolar" system. We have sketched these two methods of calculating the mobilities in **Fig. 6.2**. Using these differently calculated mobilities in the Langevin expression Eq. (6.1) we obtain recombination rates that we will call $R_{\text{Lan,uni}}$ and $R_{\text{Lan,bi}}$, respectively.

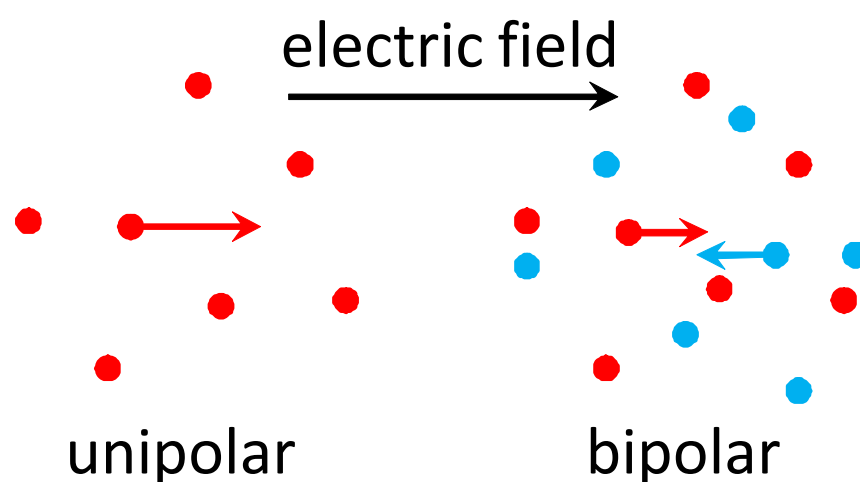


Figure 6.2: The two methods of calculating mobilities in this work. In the "unipolar" method we consider the presence of only one type of carrier and calculate its mobility. In the "bipolar" method we consider the presence of both types of carriers (blue: electrons, red: holes) and calculate both their mobilities. In the "bipolar" method the mobilities of one carrier type are smaller than in the "unipolar" method, because of the additional Coulomb interactions with the other carrier type. The figure indicates the typical situation in which almost all carriers are trapped in energetically deep-lying states in the Gaussian density of states, with only a few carriers that are mobile and contribute to the conduction.

6.3 Results

In our simulations we have used the following parameters: $a = 1.6$ nm, $\nu_{0,h} = 3.5 \times 10^{20}$ s⁻¹, and $\epsilon_r = 3$ (typical for organic semiconductors). The values for a and $\nu_{0,h}$ are those found in Ref. 9 from a fit of the EGDM to measured current-voltage characteristics for a PPV derivative (poly(2-methoxy-5-(3',7'-dimethyloctyloxy)-*p*-phenylene vinylene), OC₁C₁₀-PPV). The simulation box has a size of $100 \times 100 \times 100$ sites. Averages are performed over several (typically 20) different configurations of the Gaussian disorder, from which an error estimate is obtained. The following values for the cut-off radius of the finite-range Coulomb potential of Eq. (6.4) were found to be sufficient: $R_c = 19.2, 32,$ and 64 nm for the electron and hole densities studied in this work: $n_e = n_h = 10^{-3}, 10^{-4},$ and 10^{-5} carriers per site, respectively.

In **Fig. 6.3** we investigate the effect of disorder on the ratio R/R_{Lan} of the zero-field ($F = 0$) MC recombination rate R and the Langevin recombination rate R_{Lan} , given by Eq. (6.1). In Figs. 6.3(a), (c), and (e) we display R/R_{Lan} as a function of disorder energy σ for equal electron and hole hopping frequencies ($\nu_{0,e} = \nu_{0,h}$), at room temperature ($T = 300$ K), using three different electron and hole densities in a range typical for OLEDs: $n_e = n_h = 10^{-3}$ (a), 10^{-4} (c), and 10^{-5} carriers per site (e). In Figs. 6.3(b), (d), and (f) the corresponding unipolar and bipolar mobilities are displayed. Results are shown for correlated as well as anti-correlated disorder. In **Fig. 6.4** we investigate the effect of taking different mobilities of electrons and holes. In **Figs. 6.4(a), (c), and (e)** we display R/R_{Lan} as a function of the ratio $\nu_{0,e}/\nu_{0,h}$ between the electron and hole hopping frequencies in Eq. (6.2), at room temperature, using three different disorder energies: $\sigma = 50$ (a), 100 (c), and 150 meV (e). The density of electrons and holes is $n_e = n_h = 10^{-4}$ carriers per site. In **Figs. 6.4(b), (d), and (f)** the corresponding mobilities are displayed.

With the unipolar mobilities used in the Langevin formula Eq. (6.1) ($R_{\text{Lan,uni}}$) substantial deviations are found from the simulated recombination rates. As expected (see the Introduction), the recombination rate for correlated electron and hole energies is larger than for anti-correlated electron and hole energies. Surprisingly, however, the deviations from the simulated recombination rates almost completely disappear when the bipolar mobilities are used in the Langevin formula ($R_{\text{Lan,bi}}$). Only for the largest density, $n_e = n_h = 10^{-3}$ carriers per site, some deviations are observed. This is not unexpected, since the average distance between electrons and holes is then smaller than the thermal capture radius. Also surprisingly, $R/R_{\text{Lan,bi}} \approx 1$ both for correlated and anti-correlated disorder, when the corresponding bipolar mobilities are inserted in the Langevin formula. We note that the bipolar mobilities $\mu_{\text{bi,corr}}$ and $\mu_{\text{bi,anti-corr}}$ are *different* for the cases of correlated and anti-correlated electron and hole energies, whereas the unipolar mobilities μ_{uni} are the same. A very important conclusion that we draw from these results is that *the Langevin formula is still valid when the appropriate mobilities are used.*

This conclusion is further supported by **Fig. 6.5**, in which we investigate the temperature-

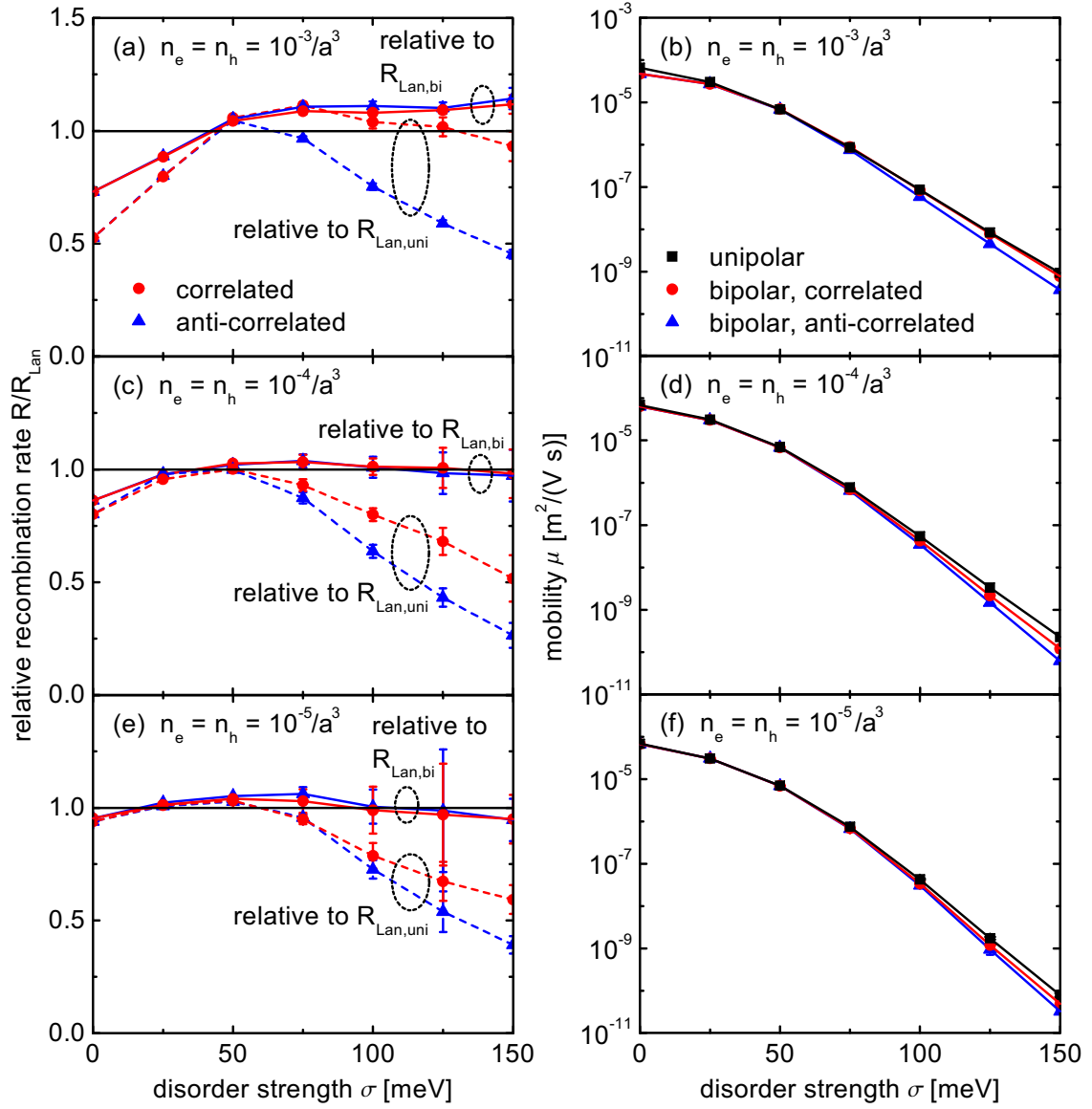


Figure 6.3: (a), (c), (e): Zero-field recombination rate R relative to the Langevin recombination rate R_{Lan} as a function of disorder energy σ , at temperature $T = 300$ K and three different electron and hole densities n_e and n_h . Red circles/blue triangles: correlated/anti-correlated electron and hole energies. Solid/dashed lines: Langevin recombination rate calculated with bipolar/unipolar mobilities. (b), (d), (f): Corresponding unipolar (black squares) and bipolar mobilities.

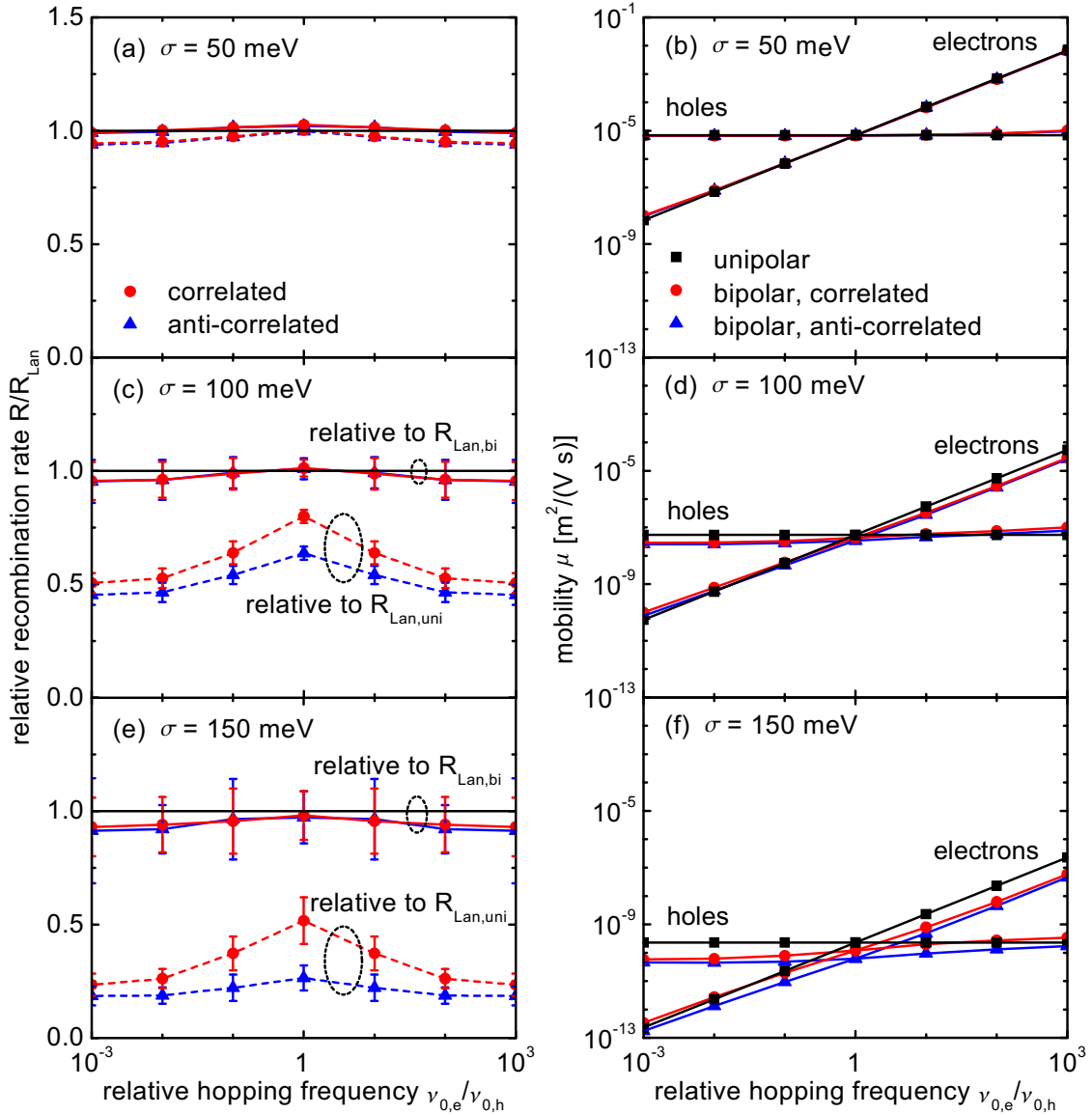


Figure 6.4: (a), (c), (e): Zero-field recombination rate R relative to the Langevin recombination rate R_{Lan} as a function of relative hopping frequency ratio $\nu_{0,e}/\nu_{0,h}$ of electrons and holes, at temperature $T = 300$ K, electron and hole densities $n_e = n_h = 10^{-4}/a^3$, and three different disorder energies. (b), (d), (f): Corresponding electron and hole mobilities. Symbols and lines as in Fig. 6.3.

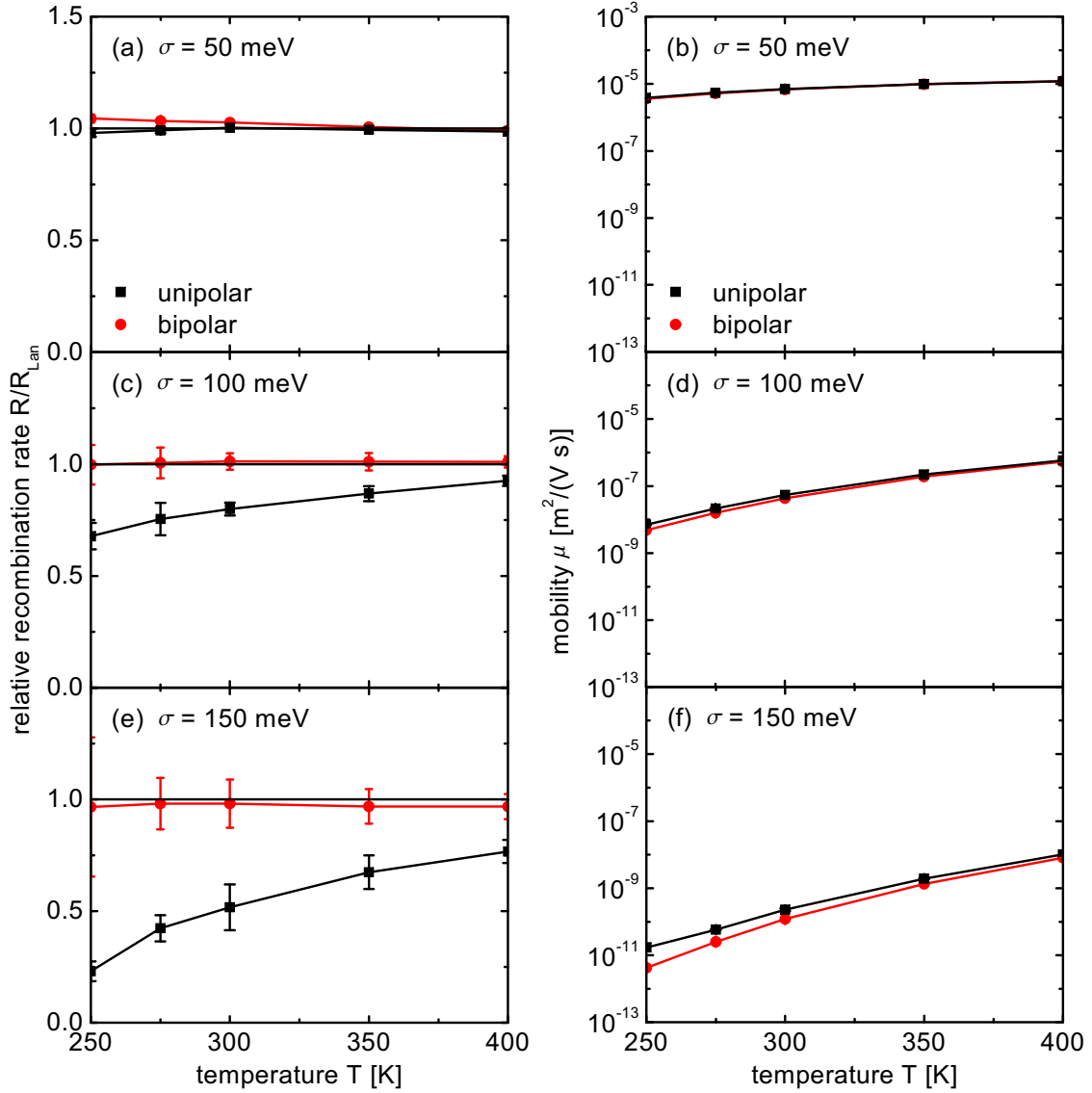


Figure 6.5: (a), (c), (e): Zero-field recombination rate R relative to the Langevin recombination rate R_{Lan} , calculated for correlated electron and hole energies, as a function of temperature T , at electron and hole densities $n_e = n_h = 10^{-4}/a^3$ and three different disorder energies. Red circles/black squares: Langevin recombination rate calculated with bipolar/unipolar mobilities. (b), (d), (f): Corresponding mobilities.

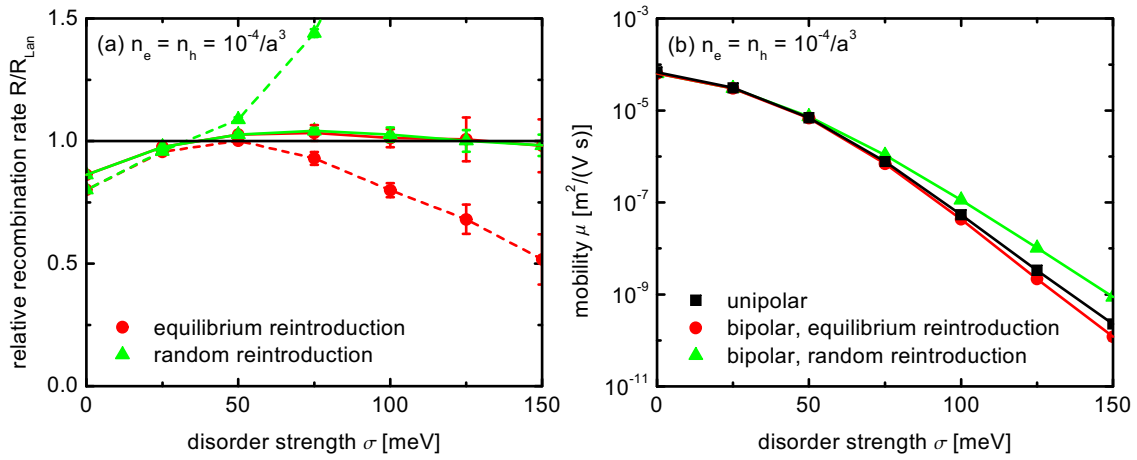


Figure 6.6: (a): Zero-field recombination rate R relative to the Langevin recombination rate R_{Lan} as a function of disorder strength σ , at temperature $T = 300$ K, electron and hole densities $n_e = n_h = 10^{-4}/a^3$, and correlated electron and hole energies, calculated for different reintroduction procedures of electrons and holes. Red circles/green triangles: equilibrium/random reintroduction. Solid/dashed lines: Langevin recombination rate calculated with bipolar/unipolar mobilities. (b): Corresponding unipolar (black squares) and bipolar mobilities.

dependence of R/R_{Lan} and the corresponding mobilities for three different disorder energies: $\sigma = 50$ (a,b), 100 (c,d), and 150 meV (e,f). The density of electrons and holes is $n_e = n_h = 10^{-4}$ carriers per site and correlated electron and hole energies are taken. Again, with unipolar mobilities substantial differences are found between the Langevin and the simulated recombination rates, whereas with bipolar mobilities these differences disappear completely.

To check the influence of the specific way of reintroducing the electron and hole after a recombination event, we performed room-temperature simulations with random reintroduction of electrons and holes, for $n_e = n_h = 10^{-4}$ carriers per site, varying disorder strengths, and correlated electron and hole energies; see **Fig. 6.6**. As expected, we find larger bipolar mobilities (by about a factor eight for $\sigma = 150$ meV) but if we use these mobilities in the Langevin expression Eq. (6.1), R/R_{Lan} becomes indistinguishable from the values found with reintroduction according to an equilibrium distribution (the latter are the same as in **Fig. 6.3** (c)). Hence, the specific reintroduction mechanism does not affect the above conclusion.

Finally, we investigate the electric-field dependence of the recombination rate. **Fig. 6.7** shows the ratio $R/R_{\text{Lan,bi}}$ and the corresponding bipolar mobilities as a function of the electric field F , at room temperature, for three different electron and hole densities and three different disorder energies: $\sigma = 50$ (a,b), 100 (c,d), and 150 meV (e,f). Correlated electron and hole energies are taken. We now observe that some deviations between the Langevin

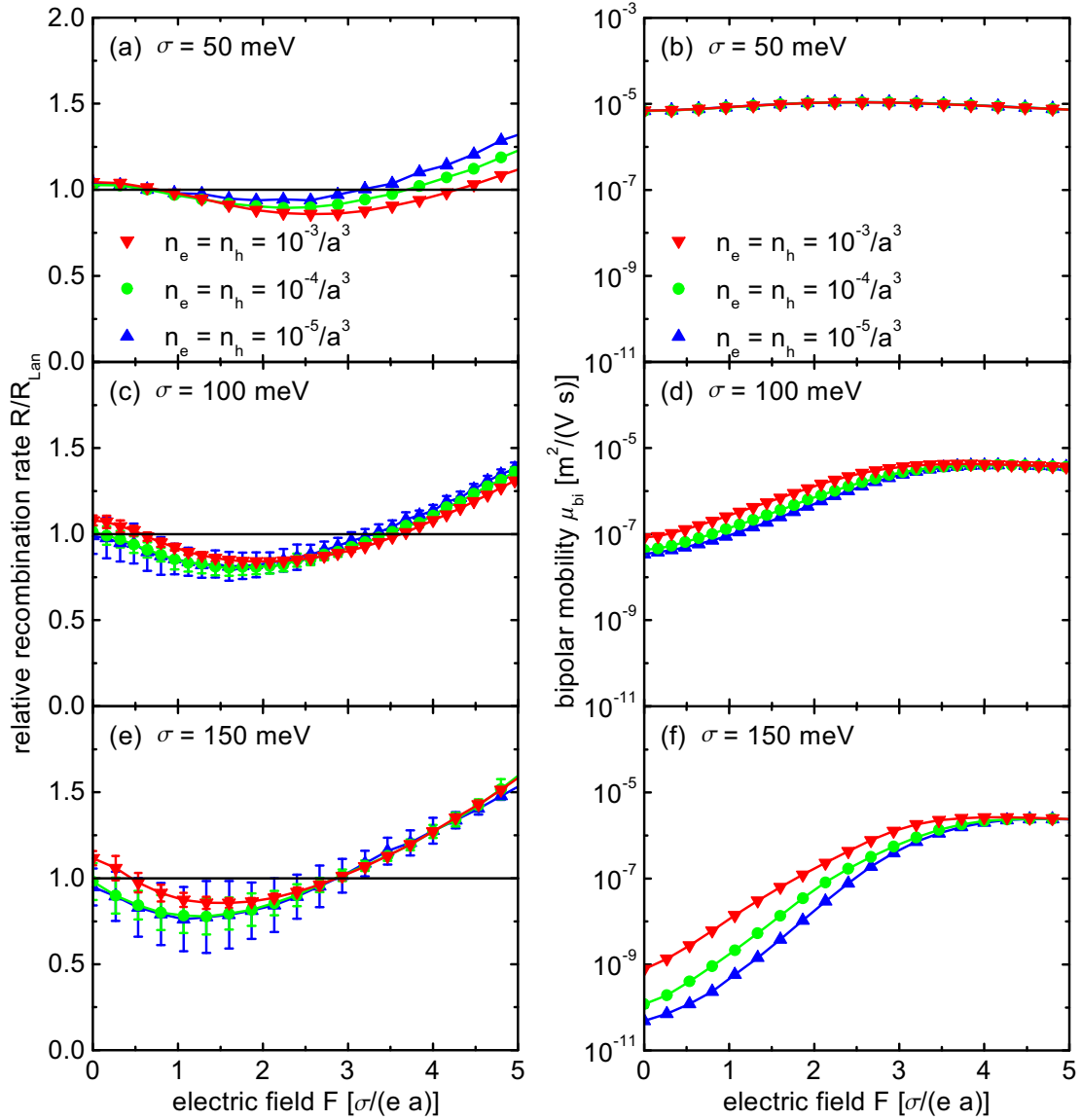


Figure 6.7: (a), (c), (e): Recombination rate R relative to the Langevin recombination rate $R_{\text{Lan,bi}}$, calculated with bipolar mobilities and correlated electron and hole energies, as a function of electric field F , at temperature $T = 300 \text{ K}$, at three different electron and hole densities, and three different disorder energies. (b), (d), (f): Corresponding bipolar mobilities.

and the simulated recombination rates occur. In the limit of vanishing carrier densities such deviations were already observed in the MC simulations of Albrecht and Bässler^{10,11} and Gartstein *et al.*,¹² who suggested that these can be attributed to "field-induced mobility anisotropy".¹² Moreover, the electric-field dependence of the charge-carrier mobility leads in the original Langevin problem to a gradient in the charge-carrier density around a recombination site, leading to a non-zero diffusion contribution that has to be taken into account.²⁸ The deviations from the Langevin recombination rate that we observe increase with increasing disorder energy σ . This is in agreement with the increase of the electric-field dependence of the mobility with increasing σ .⁹ Interestingly, we observe that the electric-field dependence of $R/R_{\text{Lan,bi}}$ has only a weak dependence on the charge-carrier density, which is in agreement with the observation that the electric-field dependence can be included in the mobility by a density-independent prefactor.⁹ We note that in **Fig. 6.7** the electric field was applied along an axis of the cubic lattice (the (100)-direction). We observed that different dependencies at high electric field ($F \gg \sigma/(ea)$) are found when applying the field along the (111)-direction, due to the increasing anisotropy in the mobility tensor with electric field. However, the relevant region for OLED modeling is $F < \sigma/(ea)$. In this region, the deviations from the Langevin prediction remain quite modest.

6.4 Discussion and conclusions

We have performed Monte-Carlo simulations of electron-hole recombination in a homogeneous and isotropic disordered organic semiconductor, including all aspects that are relevant for this process: disorder, finite densities of electrons and holes, Coulomb interactions, an applied electric field, different mobilities of electron and holes, and different types of correlation between on-site electron and hole energies. We come to the important conclusion that at zero applied electric field the Langevin expression for the recombination rate is very accurate if the appropriate charge-carrier mobilities are used, i.e., the charge-carrier mobilities as calculated in exactly the bipolar system studied. These mobilities are different from the corresponding mobilities as calculated in a unipolar system with only one charge-carrier type present. In particular, the "unipolar" mobilities are higher than the "bipolar" mobilities. The reason for this is that in the bipolar system the additional Coulomb interactions with the oppositely charged carriers lead to an enhanced disorder, resulting in a lower mobility; see Fig. 6.2. In the bipolar system, the mobilities for the case of correlated electron and hole energies are larger than for the case of anti-correlated electron and hole energies. We attribute this to the larger effect of state-filling for the correlated case as compared to the anti-correlated case, since electrons and holes compete for low-energy sites. Because state-filling effect increase the mobility, this leads to a higher mobility for the correlated case. This higher mobility then leads to a higher recombination rate. Apparently, this higher recombination rate can be fully accounted for by the Langevin expression. This means that the filamentary structure of the electron and hole current as mentioned in the Introduction does not lead to a breakdown of the Langevin

expression, provided that the appropriate mobilities are used.

In order to better understand this result, we considered the distribution of the frequency of recombination events at each site as a function of the random part of the on-site energy of the site, at a disorder energy $\sigma = 100$ meV, room temperature, electron and hole densities $n_e = n_h = 10^{-4}$ carriers per site, zero electric field, and equal electron and hole mobilities; see Fig. 6.8. It turns out that in the case of correlated electron and hole energies this distribution has two components; see Fig. 6.8(a). The first component peaks at a low energy and is approximately proportional to the density of occupied states (DOOS) of electrons and holes. The second, roughly equally large, component peaks at higher energies. Analysis of our simulations shows that a typical recombination process occurs by a mobile carrier approaching an immobile carrier of opposite charge. The last step involves either the hopping of the mobile carrier to the site of the immobile carrier or the hopping of the immobile carrier to the site of the mobile carrier. Since for both possibilities this last step is downward in energy they have equal weights. The first possibility leads to the first component in the distribution and the second possibility to the second component. As compared to the Gaussian DOS, the second component is shifted downwards in energy, because the mobile charge approaches the immobile charge preferentially via a low-energy site.

In the case of anti-correlated electron and hole energies the distribution has three components; see Fig. 6.8(b). The third component is the mirror image of the first component of the correlated case, and arises because for anti-correlated electron and hole energies a high-energy site for an electron is at the same time a low-energy site for a hole. The sum of the first and third component is now approximately equally large as the second, middle, component. The middle component now becomes symmetric and is closer to the Gaussian DOS than in the correlated case.

The consequence of the above analysis is that the location of sites at which recombination events preferentially take place does not coincide with the location of the current filaments of electrons or holes. Rather, these locations coincide with, or are neighbors of, energetically low-lying sites for electrons or holes. Hence, the conclusion from this analysis is that, whereas current filaments play a primary role in determining the mobility of electrons and holes, they do not play a primary role in determining the location at which recombination events take place.

We remark that in the present work we have taken equal electron and hole densities and equal disorder energies for electrons and holes, and we have only studied the extremes of correlated and anti-correlated on-site electron and hole energies. We expect, however, that our conclusion about the validity of the Langevin expression, with the appropriate mobilities inserted, will also hold in the general case of arbitrary electron and hole densities, different disorder energies for electrons and holes, and an arbitrary correlation between electron and hole energies.

This important conclusion opens the way to simplified and accurate modeling of the re-

combination rate in OLEDs. In order to realize such modeling, the effect of the reduction of the mobility caused by the enhanced disorder due to the random Coulomb field should be quantified. This could possibly be done along the lines set out by Arkhipov *et al.*,²⁹ who calculated the increase of the effective disorder energy due to Coulomb interactions with dopant ions. We already showed in chapter 3 that the usage of an effective disorder strength is ill-defined. Hence, we should look at the distribution of energy differences. One of the additional issues that should be analyzed is the fact that the contribution to the energetic disorder from the random Coulomb field will be spatially correlated, which means that the total effective energetic disorder cannot be treated purely within the EGDM.

In the presence of an applied electric field, our simulations show deviations from the Langevin recombination rate, which can be attributed to field-induced mobility anisotropy¹² and to a non-zero diffusion contribution caused by the electric-field dependence of the mobilities. These deviations show only a weak dependence on the electron and hole density. In the range of electric fields relevant for OLEDs the deviations are quite modest.

Our conclusions are expected to have important consequences for calculations of the width of the recombination zone in OLEDs. The inclusion of the carrier-density dependence in the electron and hole mobilities leads to a narrowing of the calculated recombination zone in OLEDs, since the mobility of charge carriers entering the recombination zone decreases due to the reduced carrier density caused by recombination. Moreover, "behind" the recombination zone the mobility of charge carriers of one type decreases further due to their now very strongly reduced density.³⁰ According to the present work, an additional reduction of the carrier mobilities in and "behind" the recombination zone should occur by the increased enhanced disorder due to the random Coulomb field of the carriers of the opposite sign. This should lead to a further reduction of the calculated width of the recombination zone.

References

- [1] Pope, M.; Swenberg, C. *Electronic Processes in Organic Crystals and Polymers*; Oxford University Press, 1999.
- [2] Langevin, M. *Ann. Chim. Phys* **1903**, *7*, 433.
- [3] Yu, Z.; Smith, D.; Saxena, A.; Martin, R.; Bishop, A. *Phys. Rev. B* **2001**, *63*, 085202.
- [4] Tutiš, E.; Batistić, I.; Berner, D. *Phys. Rev. B* **2004**, *70*, 161202(R).
- [5] Meisel, K.; Pasveer, W.; Cottaar, J.; Tanase, C.; Coehoorn, R.; Bobbert, P.; Blom, P.; de Leeuw, D.; Michels, M. *Phys. Stat. Sol. (c)* **2006**, *3*, 267.
- [6] Kwiatkowski, J. J.; Nelson, J.; Li, H.; Bredas, J. L.; Wenzel, W.; Lennartz, C. *Phys. Chem. Chem. Phys.* **2008**, *10*, 1852.

- [7] van der Holst, J.; Uijtewaal, M.; Ramachandhran, B.; Coehoorn, R.; Bobbert, P.; de Wijs, G.; de Groot, R. *Phys. Rev. B* **2009**, *79*, 085203.
- [8] Tanase, C.; Meijer, E.; Blom, P.; de Leeuw, D. *Phys. Rev. Lett.* **2003**, *91*, 216601.
- [9] Pasveer, W.; Cottaar, J.; Tanase, C.; Coehoorn, R.; Bobbert, P.; Blom, P.; de Leeuw, D.; Michels, M. *Phys. Rev. Lett.* **2005**, *94*, 206601.
- [10] Albrecht, U.; Bäessler, H. *Phys. Stat. Sol. (b)* **1995**, *191*, 455.
- [11] Albrecht, U.; Bäessler, H. *Chem. Phys.* **1995**, *199*, 207.
- [12] Gartstein, Y.; Conwell, E.; Rice, M. *Chem. Phys. Lett.* **1996**, *249*, 451.
- [13] Miller, A.; Abrahams, E. *Phys. Rev.* **1960**, *120*, 745.
- [14] Scher, H.; Rackovsky, S. *J. Chem. Phys.* **1984**, *81*, 1994.
- [15] Böttger, H.; Bryksin, V. *Phys. Stat. Sol. (b)* **1976**, *78*, 9.
- [16] Groves, C.; Greenham, N. *Phys. Rev. B* **2008**, *78*, 155205.
- [17] Bäessler, H. *Phys. Stat. Sol. (b)* **1993**, *175*, 15.
- [18] Coehoorn, R.; Pasveer, W.; Bobbert, P.; Michels, M. *Phys. Rev. B* **2005**, *72*, 155206.
- [19] Bouhassoune, M.; van Mensfoort, S.; Bobbert, P.; Coehoorn, R. *Org. Electron.* **2009**, *10*, 437.
- [20] van Mensfoort, S.; Vulto, S.; Janssen, R.; Coehoorn, R. *Phys. Rev. B* **2008**, *78*, 085208.
- [21] van Mensfoort, S.; Coehoorn, R. *Phys. Rev. B* **2008**, *78*, 085207.
- [22] Emtage, P.; O'Dwyer, J. *Phys. Rev. Lett.* **1966**, *16*, 356.
- [23] Gartstein, Y.; Conwell, E. *Chem. Phys. Lett.* **1995**, *245*, 351.
- [24] Dunlap, D.; Parris, P.; Kenkre, V. *Phys. Rev. Lett.* **1996**, *77*, 542.
- [25] Novikov, S.; Dunlap, D.; Kenkre, V.; Parris, P.; Vannikov, A. *Phys. Rev. Lett.* **1998**, *81*, 4472.
- [26] de Vries, R.; van Mensfoort, S.; Shabro, V.; Vulto, S.; Janssen, R.; Coehoorn, R. *Appl. Phys. Lett.* **2009**, *94*, 163307.
- [27] Zhou, J.; Zhou, Y.; Zhao, J.; Wu, C.; Ding, X.; Hou, X. *Phys. Rev. B* **2007**, *75*, 153201.
- [28] Obarowska, M.; Godlewski, J. *Synth. Met.* **2000**, *109*, 219.

- [29] Arkhipov, V.; Heremans, P.; Emelianova, E.; Bäessler, H. *Phys. Rev. B* **2005**, *71*, 045214.
- [30] Coehoorn, R.; van Mensfoort, S. *Phys. Rev. B* **2009**, *80*, 085302.

Chapter 7

Relaxation of charge carriers in organic semiconductors

ABSTRACT

In the previous chapters we showed results from three-dimensional simulations of devices of organic semiconductors. In these simulations, the electronic properties were obtained in a steady-state situation. However, in many experiments electronic properties are not measured in a steady-state condition. For example, in a device with a time-varying applied voltage, carriers cannot relax immediately to a steady-state situation. In this chapter we study the time-dependent mobility due to relaxation of charges.

Right after the introduction of additional charges in an organic semiconductor, the charges on average have higher energies than in equilibrium. This results in an increase of the current. This current decreases as charges start to relax to energetically lower-lying sites. The decrease of the current continues until the current reaches its new steady-state value. Surprisingly, the time-dependent current is independent of the charge-carrier density for quite a long time, until this current attains a value somewhat higher than the steady-state current. Beyond this point, the time-dependent current branches off and saturates to the steady-state current.¹

¹The contents of this chapter are based on work that has been published: W. Chr. Germs, J.J.M. van der Holst, S.L.M. van Mensfoort, P.A. Bobbert, R. Coehoorn **2010**, *In preparation*

7.1 Introduction

In the device-modeling approaches that we used in the previous chapters of this thesis, the charge-carrier current and mobility were obtained assuming a steady-state (when a net current flows) or equilibrium (when no current flows) condition. However, many experiments probe charge-carrier transport in a non-steady-state condition.

When the charge-carrier density n in a system is increased by a small amount δn , the current I will accordingly instantaneously increase by a small amount, as shown in **Fig. 7.1**. The reason for this is that the additional charge carriers have to be situated on sites with on average a higher site-energy than the already present charge carriers and therefore they will be more mobile, resulting in a higher current. After the introduction, charges move to sites with on average a lower site-energy, leading to a slow relaxation of the current, until it saturates to the steady-state value. As the carrier density is obviously higher after the introduction of the charge carriers, the steady-state current after the introduction will be somewhat higher than the steady-state current before the introduction.

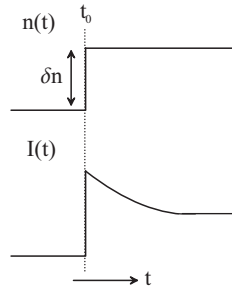


Figure 7.1: An increase of the carrier density n by a small amount δn at time t_0 leads to an increase of the current I . Right after the introduction of the additional charges, the current I will slowly decrease and saturate to its steady-state value.

The relaxation of charge carriers in a Gaussian DOS has been studied earlier by Bässler *et al.*^{1,2} using Monte Carlo (MC) modeling. However, they only studied the Boltzmann limit of vanishing carrier density, with one carrier in the simulation box. With the present computational power, we are able to study the relaxational properties of charge-carrier transport at finite carrier densities, with many carriers in the simulation box.

Another, more phenomenological, approach is the use of the multiple-trapping (MT) model.³ The MT model assumes the transport to take place by the fraction f_c of the charges in a high-energy transport level E_c , while the rest of the charges are immobile in a distribution of lower lying energetic trap levels. The time-dependent occupational probability f_c of the transport level is in this model related to the time-dependent occupational probability of the energetically lower-lying trap levels via a master equation. Charge transport takes place by hopping from the trap levels to the transport level, in which charge transport can

take place. By solving the corresponding master equation, one obtains the time dependence of f_c . The fraction f_c decreases over time and therefore the current I also decreases, until it saturates to the steady-state current. Results of MC simulations of the charge-carrier transport are consistent with the MT model.⁴ From these results a frequency-dependent mobility function can be calculated. We have found that this frequency-dependent mobility function can describe the charge-carrier relaxation contribution to the frequency-dependent electrical response in single-carrier devices of polyfluorene-(7,5 mol-% triarylamine) (PF-TAA) quite well.⁴

In this chapter we present the results of the MC simulations used to carry out the analysis as reported in Ref. 4. We study the time-dependence of the relaxation mobility for different disorder strengths, charge-carrier densities, and electric field strengths. As was shown in chapter 3, the Coulomb interactions between the charges only have a minimal effect on the steady-state mobility for the studied carrier densities. For this reason, we neglect the Coulomb interactions in this study.

This chapter is built up as follows. In the next section we discuss our Monte-Carlo procedure. In Section 7.3 we present the mobility relaxation curves. In Section 7.4 we discuss our results and present our conclusions.

7.2 Monte-Carlo method

In this section the Monte-Carlo method is described for calculating the time-dependent mobility relaxation curves. We take a simple-cubic lattice of $L_x \times L_y \times L_z$ sites, with L_x, L_y , and L_z the size of the lattice in the x -, y - and z -direction. We take periodic boundary conditions. The inter-site distance is given by a . The electric field is directed in the x -direction. We assume that transport of charge carriers takes place by the hopping of charges from one site to an other, as a result of a tunneling process that is thermally assisted due to the coupling to a system of acoustical phonons. The hopping rate from site \mathbf{i} to \mathbf{j} is then of the Miller-Abrahams form:⁵

$$W_{\mathbf{ij}} = \nu_0 \exp \left[-2\alpha |\mathbf{R}_{\mathbf{ij}}| - \frac{E_{\mathbf{j}} - E_{\mathbf{i}} - eFR_{\mathbf{ij},x}}{k_{\text{B}}T} \right] \quad \text{for } E_{\mathbf{j}} \geq E_{\mathbf{i}} + eFR_{\mathbf{ij},x}, \quad (7.1a)$$

$$W_{\mathbf{ij}} = \nu_0 \exp [-2\alpha |\mathbf{R}_{\mathbf{ij}}|] \quad \text{for } E_{\mathbf{j}} < E_{\mathbf{i}} + eFR_{\mathbf{ij},x}, \quad (7.1b)$$

with ν_0 an intrinsic rate, $|\mathbf{R}_{\mathbf{ij}}| \equiv a|\mathbf{i} - \mathbf{j}|$ the distance between sites \mathbf{i} and \mathbf{j} , α the inverse localization length of the localized wave functions, $E_{\mathbf{i}}$ the on-site energy of site \mathbf{i} , e the unit charge, and $eFR_{\mathbf{ij},x} \equiv eFa(j_x - i_x)$ a contribution due to an applied field.

We only consider the situation of uncorrelated Gaussian disorder, as Mensfoort *et al.* had shown that the current density in sandwich-type device consisting of PF-TAA could be

very well described by the EGDM.^{6,7} The energies E_i are then randomly drawn from a Gaussian density of states (DOS):

$$g(E) = \frac{1}{\sqrt{2\pi}\sigma a^3} \exp\left[-\frac{E^2}{2\sigma^2}\right], \quad (7.2)$$

with σ the width of this DOS.

Our simulations proceed as follows. First, charge carriers are placed into the simulation box at random sites. This reflects the injection of charge carriers as shown in **Fig. 7.1**. After that, carriers are allowed to hop to other sites. Hops of carriers are chosen with weights determined by the hopping rates given by Eq. (7.1). For every hop, a hopping time is chosen from an exponential distribution with an inverse decay time equal to the sum of all possible hopping rates. We take an integer number k , which is set to 1. The time-dependent total distance $x(t)$ that all the charges have hopped in the x -direction, which is the direction along the electric field, is stored every time the simulation time t_{sim} is larger than $t_k = 10^{dk}t_c$ with $t_c = \nu_0 \exp[-2a\alpha]$. Here, d a constant with which the frequency that the distance $x(t)$ is sampled can be controlled. This is done up to the largest k for which $t_{\text{sim}} \geq t_k$, after which k is increased by one. The simulation stops once the simulated current is within 5% equal to the steady-state current. This is a condition which is hard to check during the simulation itself, as we will see in the next paragraph. Therefore, a maximum simulation time $t_{k_{\text{max}}}$ is chosen, after which we check whether the current at this maximum simulation time is close to constant as a function of the simulation time. In that case, the current is close to the steady-state current. We compare the obtained steady-state current with the EGDM as an extra check.

To obtain the current $I(t)$, we calculate the derivative of the time-dependent position function $x(t)$. $I(t_k)$ is then obtained by

$$I(t_k) = \frac{e}{2} \left[\frac{x(t_{k+1}) - x(t_k)}{t_{k+1} - t_k} + \frac{x(t_k) - x(t_{k-1})}{t_k - t_{k-1}} \right]. \quad (7.3)$$

If d is too small, the time intervals after which the average position of the charges are sampled are too small. As a result, the relaxation curves are quite noisy and the resulting error bars are quite large, as the derivative is calculated over noisy $x(t)$ curves. By taking a larger value for d , the frequency of the time steps at which the average position is sampled becomes lower and the effect of the noisiness of $x(t)$ is reduced considerably, leading to a smoother $J(t)$ curve with a smaller relative error. The noise can also be reduced by calculating the derivative of the average of several time-dependent position functions, $\langle x(t) \rangle$, from different disorder configurations and different starting sites for the charges, instead of calculating the derivative of a single time-dependent position curve $x(t)$. The final result for the time-dependent current is obtained by averaging over different disorder configurations and initial starting sites for the charges. The relative accuracy of the part of the current relaxation curve in which we are interested is around 20 – 25% in the case of the Boltzmann limit and better for higher carrier densities.

The time-dependent mobility $\mu(t)$ is obtained from the time-dependent current $I(t)$ by the following equation

$$\mu(t) = \frac{I(t)}{enFL_yL_z a^2}. \quad (7.4)$$

7.3 Relaxation of the mobility

In **Fig. 7.2(a)** we display the average total distance $\langle x(t) \rangle$ over which the charges have hopped in the direction along the electric field and in **Fig. 7.2(b)** we display the time-dependent mobility function $\mu(t)$. The calculations are performed for the Boltzmann limit, for uncorrelated Gaussian disorder with three different disorder strengths ($\sigma = 3, 4$ and $5.11 k_B T$). The value of $\sigma = 5.11 k_B T$ is the value obtained by fitting the EGDM to the experimentally measured hole mobility in PF-TAA.^{6,7} The lattice constant is taken equal to $a = 1.19$ nm, which is also the value obtained from this fitting.^{6,7} The wavefunction decay length is chosen equal to $\alpha^{-1} = 0.1$ nm. We allow hops over a maximum distance $\sqrt{3}a$, as in all our previous simulations. The periodic simulation box is chosen to be $250 \times 250 \times 250$ sites, which is sufficiently large to obtain converged results. For the electric field we use the value $F \approx 0.6\sigma/(ea)$, a value for which, as we will show, the time-dependent mobility curve approximates the zero-field time-dependent mobility curve. We express the simulation time in terms of $t_0 = (\nu_0 \exp[-2\alpha a])^{-1}$, which for a typical values of $\nu_0 = 10^{10} s^{-1}$ and $10^{15} s^{-1}$ corresponds to $t_0 = 2s$ and $2 \cdot 10^{-5} s$, respectively.

The mobility right after the charges have been placed into the simulation box is larger than the steady-state value. For $\sigma = 3 k_B T$ the difference between the mobility right after the injection and the steady-state value of the mobility is about a factor 10, for $\sigma = 4 k_B T$ the difference is about a factor 100, and for $\sigma = 5.11 k_B T$ the difference is about a factor 10,000.

As the DOS is Gaussian, the sites at which the charges are initially placed have on average a site-energy equal to zero. After the charges are placed in the simulation box, the charges will hop around to sites which are on average lower in energy. When the time-dependent mobility becomes equal to the steady-state mobility, the average energy of the sites that are visited by the charges becomes equal to $E_{t=\infty} = -\sigma^2/(k_B T)$ in the Boltzmann limit, as shown by Bässler *et al.*² The higher the disorder strength, the longer it takes for the mobility to relax to the steady-state mobility. This can be explained by the fact that the waiting time, the time that a charge is located on a site, is on average larger when the disorder strength is larger. Moreover, during the relaxation, the charge will be trapped on sites with increasingly lower energy, which leads to longer waiting times.

In **Fig. 7.3** we display the time-dependent mobility function $\mu(t)$ for six different charge carrier densities. The disorder strength is taken equal to $\sigma = 5.11 k_B T$. The other

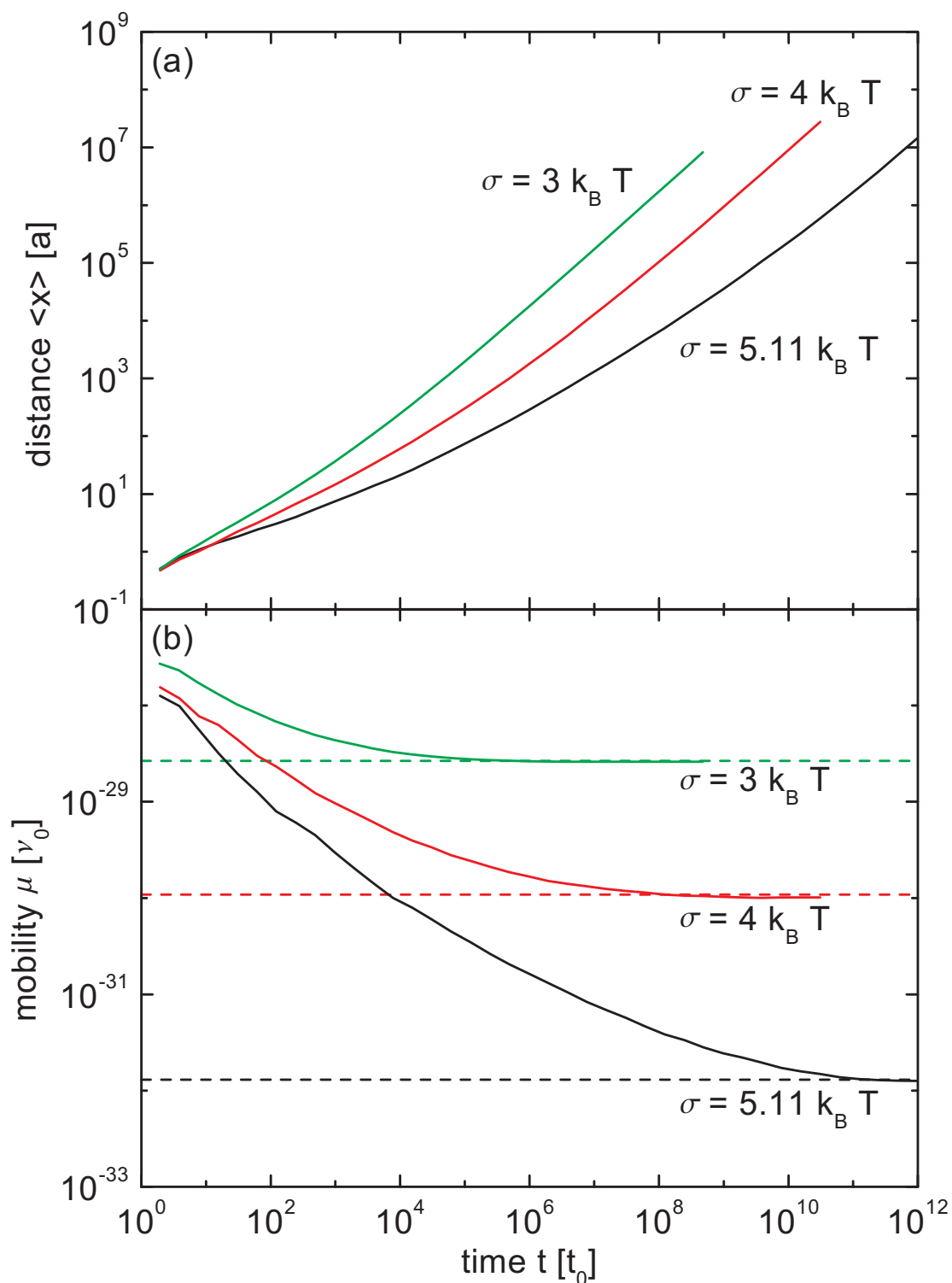


Figure 7.2: (a): Time-dependence of the average total distance $\langle x(t) \rangle$ that all charges in the simulation box have hopped in the direction along the electric field (x -direction) for three different disorder strengths. The results are obtained in the Boltzmann limit. (b): Time-dependent mobility relaxation curves obtained from $\langle x(t) \rangle$. Solid curves: relaxation results. Dashed lines: steady-state values of the mobility.

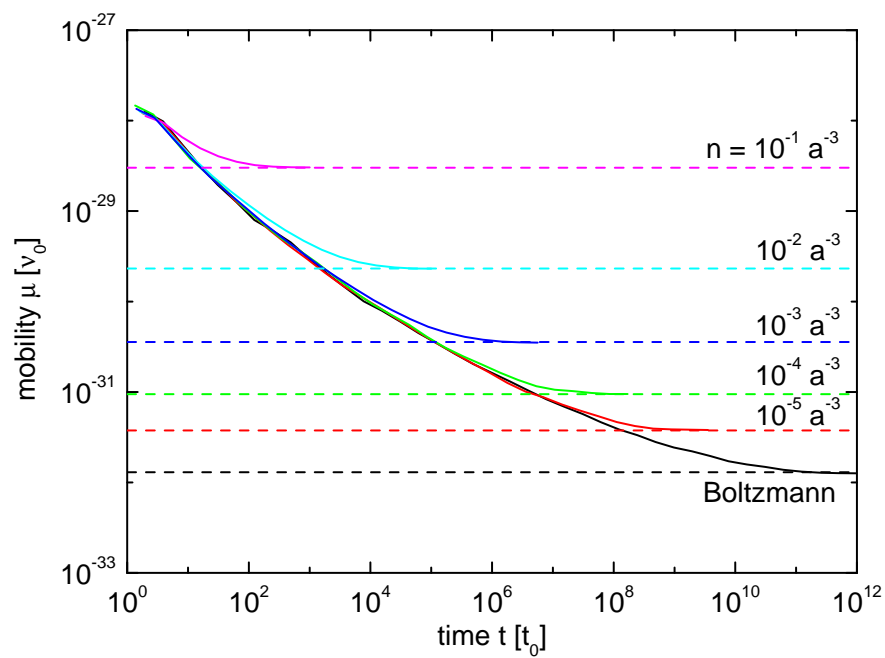


Figure 7.3: Mobility relaxation curves for six different charge-carrier densities. The disorder strength is taken equal to $\sigma = 5.11k_B T$. Solid curves: relaxation results. Dashed lines: steady-state values of the mobility.

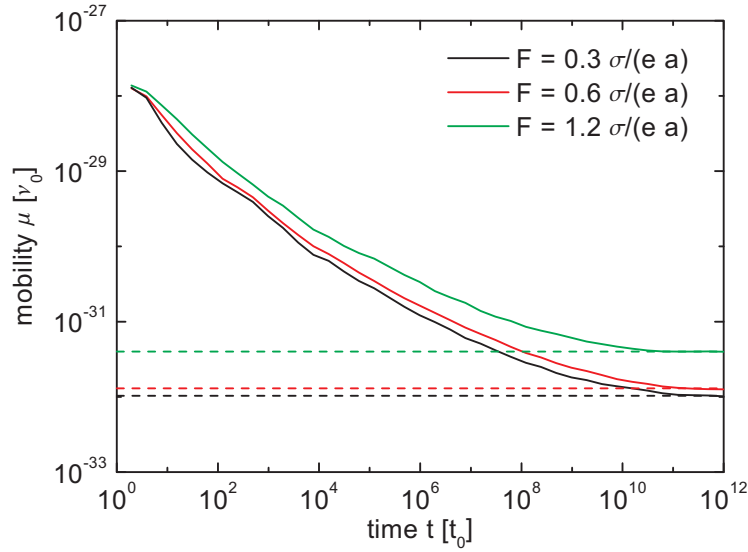


Figure 7.4: Mobility relaxation curves for three different field strengths. The disorder strength is taken equal to $\sigma = 5.11 k_B T$. The calculation is done in the Boltzmann limit. Solid curves: relaxation results. Dashed lines: steady-state values of the mobility.

parameters are the same as in **Fig. 7.2**. The lower the charge-carrier density, the longer it takes for the time-dependent mobility to relax to the steady-state value of the mobility. The initial time dependence of the mobility is approximately independent of the density. When the mobility is somewhat higher than the steady-state values, the curves branch off from a carrier-independent mobility curve to the steady-state values. The higher the charge carrier density, the higher the steady-state mobility, because of the state-filling effect.⁸

To check whether the time-dependent mobility curve as calculated for an electric field of $F = 0.6 \sigma/(ea)$ correctly approximates the mobility curve for zero-electric field, we also studied the relaxation of the mobility for other electric field strengths. In **Fig. 7.4** we display the Boltzmann-limit mobility curve $\mu(t)$ for three different electric field strengths. The disorder strength is again taken equal to $\sigma = 5.11 k_B T$, while the rest of the device parameters are the same as in **Fig. 7.2**.

The transition of the time-dependent mobility to the steady-state value occurs approximately at the same time, independent of the studied electric field strengths. The curves calculated for $F = 0.3 \sigma/(ea)$ and $F = 0.6 \sigma/(ea)$ are equal, up to a constant shift. Because of field-reversal symmetry, the mobility in the regime of very low electric fields should be a quadratic function of the electric field. From this we conclude that the time dependence of the mobility for $F = 0.6 \sigma/(ea)$ is approximately equal to the time dependence of the time dependent mobility curve for a vanishing electric field, up to a constant shift.

7.4 Conclusion and outlook

In this chapter we studied the time-dependent properties of the mobility by means of Monte-Carlo simulations. Right after the injection of additional charges, the mobility will be higher than in steady-state. The mobility decreases with time due to the relaxation of the charges in the disordered landscape or random site energies. The dependence of the time-dependent mobility on the disorder strength, charge carrier density and electric field strength was studied. Coulomb interactions were neglected, as these interactions have a negligible effect on the mobility at the carrier densities of interest.

In all studied cases, the difference between the mobility right after charge injection and the steady-state mobility is very large. The relaxation of the mobility to the steady-state mobility strongly depends on the disorder strength. The higher the disorder strength, the longer it takes for the mobility to relax to its steady-state value. Right after the injection of the charges, the time-dependent mobility is independent of the charge carrier density. Once the time-dependent mobility curve reaches a value that is somewhat higher than the steady-state mobility, the mobility branches off from the carrier-independent curve to this steady-state mobility. The modeling of the time-dependent mobility is important for the correct understanding of (ac)-frequency-dependent properties of organic devices. When the applied voltage over a device contains a (small) oscillating contribution, the charges experience an oscillating field. Therefore, the mobility cannot relax to its steady-state value. The frequency-dependent mobility that describing this situation can be obtained by Fourier transformation of the time-dependent mobility determined in this chapter.⁴

Also in the context of recombination processes the time-dependence of the mobility plays an important role. As we saw in the Monte-Carlo simulations of recombination in Chapter 6, whenever an electron and a hole recombine, another electron and another hole have to be reintroduced at other sites. After the two charges are reintroduced, they are not yet in a steady-state situation. These charges will have a time-dependent mobility, which is right after the reintroduction either larger or smaller than their steady-state mobility, depending on the chosen reintroduction procedure. We came to that conclusion that the Langevin formula is still valid when "bipolar" mobilities are used. In able to parameterize this "bipolar" mobility, the relaxational effect of the mobility should be taken into account.

This is also true in a real double-carrier device setting. In a double-carrier device, electrons are injected from the cathode, while holes are injected from the anode. Right after the injection of a charge, this charge is not yet in a local equilibrium. When the charge hops through the device, it potentially reaches the collecting electrode before it can properly relax. To be able to use the Langevin formula, one should then use mobilities in which the relaxational effect is taken into account.

We conclude that the time-dependence of the mobility due to energetic relaxation of charges is highly important for the modeling of devices. This is not only true for applied voltage that vary with time, but also for a constant applied voltage.

References

- [1] Richert, R.; Pautmeier, L.; Bäessler, H. *Phys. Rev. Lett.* **1989**, *63*, 547.
- [2] Bäessler, H. *Phys. Stat. Sol. (b)* **1993**, *175*, 15.
- [3] Noolandi, J. *Phys. Rev. B* **1977**, *16*, 4474.
- [4] Germs, W.; van der Holst, J.; van Mensfoort, S.; Bobbert, P.; Coehoorn, R. *Submitted*
- [5] Miller, A.; Abrahams, E. *Phys. Rev.* **1960**, *120*, 745.
- [6] van Mensfoort, S.; Vulto, S.; Janssen, R.; Coehoorn, R. *Phys. Rev. B* **2008**, *78*, 085208.
- [7] de Vries, R.; van Mensfoort, S.; Shabro, V.; Vulto, S.; Janssen, R.; Coehoorn, R. *Appl. Phys. Lett.* **2009**, *94*, 163307.
- [8] Coehoorn, R.; Pasveer, W.; Bobbert, P.; Michels, M. *Phys. Rev. B* **2005**, *72*, 155206.

Chapter 8

Conclusions and outlook

In this thesis we have performed a modeling study of devices consisting of disordered organic semiconducting materials. The disorder of the organic material gives rise to the localization of quantum-mechanical states at specific positions, which we call sites. We have assumed that the energies of these states are randomly distributed according to a Gaussian distribution. The transport of charges occurs via the hopping of charges from one site to another. We have assumed that this hopping can be described by a thermally assisted tunneling process with coupling to a bath of acoustic phonons. The energetic disorder gives rise to an important effect, namely the transport of charges through preferential pathways. This effect is caused by percolation. The charge-carrier mobility in organic semiconducting materials can be described by the Extended Gaussian Disorder Model (EGDM) or Extended Correlated Disorder Model (ECDM), for spatially uncorrelated and correlated Gaussian disorder, respectively. These two models have been derived from Master-Equation calculations and take into account the percolating nature of charge-carrier transport and the state-filling effect, leading to a dependence of the mobility on the electric field, charge carrier density and temperature. The precise effect of the three-dimensional nature of charge-carrier transport on device properties was to a large extent unknown at the start of this thesis work. The results reported in this thesis can be used for the development of a predictive one-dimensional (1D) OLED model, yielding reliable predictions of electronic processes occurring in OLEDs. In this chapter, we will summarize our main conclusions and indicate directions for future research.

In (**Chapter 3**) we conclude that the effect of Coulomb interactions between the charges on the EGDM mobility is relatively small, except for high carrier densities and low electric field strengths. In that regime, charges experience a Coulomb potential well formed by the surrounding charges, leading to an extra energy penalty for hopping of a charge. In the EGDM (and ECDM) as developed originally, the effect of Coulomb interactions between the charge carriers was not taken into account. The reason is that it is not possible to take into account those interactions consistently in Master-Equation calculations, since the

corresponding master equation involves the time-averaged and not the actual occupational probabilities of the sites. In a Monte-Carlo approach those interactions can be taken into account explicitly, as the motion of the charges is simulated explicitly.

In **(Chapter 4)** we conclude that results of Master-Equation calculations of single-layer single-carrier devices, including the effect of the space charge, the image-charge potential and an injection barrier, agree surprisingly well with the results of a one-dimensional drift-diffusion continuum model. In this one-dimensional model, the mobility is described by the EGDM and an injection barrier lowering due to the image potential is taken into account. In the regime of high disorder strengths and high injection barriers deviations occur. In this regime, the current distribution becomes highly filamentary, consisting of one-dimensional current pathways. The current then agrees very well with a model developed by Burin and Ratner, which assumes the injection to occur over one-dimensional pathways.

In **(Chapter 5)** we conclude that the explicit inclusion of Coulomb interactions in Monte-Carlo simulations does not significantly influence the current for injection barriers of about 0.3 eV or higher. For these injection barriers, the charge-carrier density in the device is so low that Coulomb interactions do not have a significant effect. For lower injection barriers and low voltages, the Coulomb interactions lead to a decrease of the current. In this regime, the current filaments are shifted by the Coulomb interactions. The decrease in the current becomes less significant for higher disorder strengths and is smaller for correlated disorder than for uncorrelated disorder.

The classical Langevin formula for the recombination rate of charges of opposite sign was originally derived under the assumption that charge-carrier transport is homogeneous, which is obviously not the case in disordered organic materials. Nonetheless, we conclude in **(Chapter 6)** that the Langevin formula describes the recombination rate in disordered organic materials very well, when "bipolar" charge-carrier mobilities are used. In "bipolar" mobilities, the effect of the Coulomb interactions of both charge-carrier types are taken into account. Depending on the mechanism for the reintroduction of charges, this "bipolar" mobility is either larger or smaller than the "unipolar" mobility, in which only the effect of the coulomb interactions of one charge carrier type is taken into account.

In **(Chapter 7)** we conclude that the time-dependent mobility, right after the introduction of charges in a disordered organic semiconductor, is independent of the charge-carrier density up to the time that this mobility has decreased to a value which is only slightly higher than the density-dependent steady-state mobility. Right after the introduction of extra charges in the material, the charge-carrier mobility is temporarily higher than its steady-state value. Before this steady-state situation is reached, charge carriers have to relax in the Gaussian energy distribution. The higher the disorder strength, the longer the relaxation of the charges to the steady-state takes. After Fourier transformation, the resulting frequency-dependent mobility can be used to describe the current in single-carrier devices for which a small ac voltage is added to a dc voltage.

We conclude that taking the three-dimensional nature of charge-carrier transport into ac-

count in the modeling of devices is of paramount importance. In most cases it turned out to be possible to describe the three-dimensional charge-carrier transport properties by one-dimensional modeling approaches. To establish how far the translation from three-dimensional computational modeling to one-dimensional modeling approaches can be extended, we propose research in the following directions:

- From our successful simulation attempts, it seems to be very well feasible to simulate complete OLEDs. In these simulations, complete double-carrier devices would be modeled in three dimensions, including the injection of electrons at the cathode and holes at the anode. It even seems feasible to take multiple organic layers into account, each with their own disorder strengths, lattice constants, etc.. Furthermore, even the spatial correlation can be varied. It will be a challenge to extend the one-dimensional continuum drift-diffusion modeling to these situations.
- In every simulation in this thesis, a cubic lattice of sites is assumed. In reality, the site lattice in organic materials will be disordered. By performing Molecular Dynamics simulations for the organic materials used in OLEDs, the precise disordered lattice can be obtained. Moreover, the nature of the energetic disorder can then be described, including the spatial correlation and the correlation in the electron and hole site energies. Density-Functional Theory calculations can be used to calculate the hopping integrals. The obtained lattice, energetic disorder and hopping integrals can be implemented in the existing Monte-Carlo simulation software, paving the road towards advanced device simulations with realistic and material-specific input.
- In the Monte-Carlo simulations we performed for recombination, we investigated the validity of the classical Langevin formula for disordered organic materials. In those simulations, we assumed equal electron and hole densities. In double-carrier devices the electron and hole densities are in general locally unequal. It is therefore important to also investigate the validity of the Langevin formula for the case of unequal electron and hole densities.
- We have seen that the mobility in devices after the injection of charges is time-dependent. The modeling of the time-dependent mobility is important for the description of the (ac)-electrical response properties in organic materials. However, we think that the time dependence of the mobility also plays an important role in modeling the recombination in double-carrier device simulations. The Monte-Carlo modeling of recombination involves the reintroduction of an electron and a hole after a recombination event. After this reintroduction, the electron and hole will have a time-dependent mobility due to relaxation. In order to evaluate the "bipolar" mobilities to be used in the Langevin formula, this relaxation should be modeled. Only then can the Langevin formula be used in one-dimensional drift-diffusion calculations of double-carrier devices.

Summary

Three-dimensional modeling of charge transport, injection and recombination in organic light-emitting diodes

Organic light-emitting diodes (OLEDs) are ideally suited for lighting and display applications. Commercial OLED displays as well as OLED white-light sources are presently being introduced to the market. Essential electronic processes in OLEDs are the injection of electrons and holes into an organic semiconductor, their transport through the semiconductor, and their radiative recombination. In these processes an important role is played by the energetic disorder present in the organic semiconductor. This disorder leads to the localization of electronic states to specific sites. Charges move via a hopping process from one site to another. This hopping process involves quantum-mechanical tunneling assisted by a coupling to lattice vibrations. The energies of the sites are often taken to be distributed according to a Gaussian density of states (DOS). With these ingredients, the electronic processes taking place in OLEDs have been intensively investigated in the last two decades. However, this has not yet led to a satisfactory and complete OLED model that includes these processes in a consistent way, taking into account three-dimensional effects at the microscopic level. The goal of this thesis was to make an important step into this direction.

In this thesis, the motion of charge carriers is evaluated by means of calculations based on the Pauli master equation and by means of Monte-Carlo simulations, which are both introduced in Chapter 2. The Pauli master equation describes the time-averaged occupational probabilities of a three-dimensional assembly of sites. This equation can be solved by means of an iterative calculation scheme, after which relevant quantities like the current and the charge-carrier mobility can be obtained. In the Monte-Carlo approach, the actual motion of the charges is simulated in time. The advantage of Monte-Carlo simulations over Master-Equation calculations is that Coulomb interactions between the charges can be taken into account in a consistent manner.

In Chapter 3 it is shown that Coulomb interactions only influence the mobility in the case of high carrier densities and low electric field strengths. In this regime, taking into account Coulomb interactions significantly decreases the mobility. This decrease is attributed to

the trapping of charge carriers by the Coulomb potential well formed by the surrounding charges. For high electric field strengths and low charge-carrier densities, the mobility with Coulomb interactions agrees quite well with the mobility obtained without taking into account Coulomb interactions.

In Chapter 4 the charge-carrier transport in single-carrier single-layer devices consisting of a disordered organic semiconductor sandwiched in between two metallic electrodes is studied by means of Master-Equation calculations. The effects of space charge, image-charge potentials close to the electrodes, finite injection barriers, and the complete dependence of the charge-carrier mobility on the temperature, the carrier density and the electric field are taken into account. The obtained three-dimensional current density is very inhomogeneous, showing filamentary regions that carry most of the current. Nevertheless, the total current agrees quite well with that of a one-dimensional continuum drift-diffusion model. For very thin devices with a high injection barrier and a high disorder strength (large width of the Gaussian DOS), the one-dimensional continuum drift-diffusion model underestimates the current. In this regime, the current can be described very well by a model assuming injection and transport over one-dimensional straight filaments.

In the Master-Equation approach followed in Chapter 4, Coulomb interactions between charges were only taken into account in a layer-averaged way, because the approach cannot account explicitly for Coulomb interactions in a consistent way. To study the influence of explicitly taking into account Coulomb interactions between charges, the studies of the single-carrier single-layer devices were repeated with Monte-Carlo in Chapter 5. It was found that in the absence of an injection barrier taking into account Coulomb interactions explicitly leads to a decrease in the current as compared to Master-Equation calculations. This decrease can be rationalized by studying the three-dimensional current density distributions. Taking into account explicit Coulomb interactions leads to a change in the pattern of the filamentary current pathways, which in turn leads to a decrease of the total current. The case of spatial correlations in the energetic disorder was also studied. For this case the filamentary current pathways are broader and the effects of taking into account explicit Coulomb interactions are smaller.

Traditionally, the rate of recombination between electrons and holes is described by the Langevin formula, which contains the sum of the electron and hole mobilities as a factor. In Chapter 6 the question of the validity of this formula for electron-hole recombination in disordered organic semiconductors is addressed. One of the main assumptions made in deriving the Langevin formula is that charge-carrier transport occurs homogeneously throughout the semiconductor. As shown in Chapters 4 and 5, however, this is generally not the case in organic semiconductors. Nonetheless, it is found from double-carrier Monte-Carlo simulations of recombining electrons and holes that the recombination rate can be very well described by the classical Langevin formula, provided that a change in the charge-carrier mobilities due to the presence of carriers of the opposite type is taken into account. Deviations from the Langevin formula at finite electric field are found to be small at the field scale typical for OLEDs.

In Chapter 7, the time-dependent relaxational properties of charge transport are studied. When a charge is injected in a disordered organic semiconductor, its mobility will gradually decrease because of energetic relaxation of the charge into the tail of the DOS. This relaxation process was studied by inserting charges randomly in an assembly of sites with a Gaussian DOS and following the time dependence of their mobility. For short simulation times the mobility was found to be almost independent of the carrier density. However, when the mobility has decreased to a value somewhat higher than the steady-state mobility, the time-dependent mobility branches off and relaxes to the carrier-density dependent steady-state mobility. The obtained results can be used in studying the response of organic devices to a small additional ac voltage.

Finally, in Chapter 8 overall conclusions and outlook for the three-dimensional modeling of OLEDs are presented. The results presented in this thesis should be considered as a significant step towards the development of a predictive model for state-of-the-art OLEDs.

Dankwoord

Op de kaft van dit proefschrift staat dan wel mijn eigen naam, maar zonder de hulp van vele mensen was dit boekwerk nooit tot stand kunnen komen. Bij deze wil ik een aantal mensen bedanken die meegeholpen hebben met de totstandkoming van dit proefschrift.

Ten eerste wil ik mijn copromotor Peter Bobbert bedanken. Ik heb jouw samenwerking en kritische houding altijd als prettig en motiverend ervaren. De manier waarop jij je grote groep promovendi weet te begeleiden is zeker bewonderenswaardig. Daarnaast wil ik mijn eerste promotor Reinder Coehoorn bedanken. Jouw enthousiasme over niet alleen OLEDs, maar ook over een breed gebied van allerlei andere natuurkundige onderwerpen, is zeer aanstekelijk te noemen. Daarnaast wist je publicaties en zelfs dit proefschrift door je opmerkingen tot een hoger niveau te tillen.

Mijn tweede promotor Thijs Michels wilde ik bedanken voor het kritische commentaar over het proefschrift. Door je suggesties is het proefschrift zeker in kwaliteit omhoog gegaan. Daarnaast was je altijd beschikbaar voor vragen over het onderzoek.

De leden van de leescommissie, René Janssen, Rob de Groot en Thom Palstra, wil ik hartelijk bedanken voor het kritisch doorlezen van mijn proefschrift. De tekst is er zeker op vooruit gegaan qua leesbaarheid.

Mijn eerste kamergenoten, Leon van Dijk en Yeneneh Yimer, wilde ik bedanken voor de gezellige sfeer tijdens mijn eerste promotiejaren. Yeneneh, good luck with your new phd-position. I really liked our talks during the thursday afternoon drinks.

Abhinav Sharma, ik vond onze discussies over wetenschap altijd erg geslaagd. Bovendien zorgde je altijd voor een levendige en gezellige sfeer in de groep. Succes met je promotie over een half jaar.

Frank van Oost, Sander Kersten en Jeroen Cottaar wilde ik bedanken voor de nodige discussies omtrent organische elektronica. Frank, zonder jouw programmeerkunsten had de modellering van OLEDs nooit zo een boost kunnen doormaken als nu.

De overige leden van de vakgroep TPS wilde ik bedanken voor de gezelligheid tijdens de koffiepauzes en de lunchpauzes. In het bijzonder wilde ik de secretaresses Helmi en Clazien bedanken voor hun behulpzaamheid.

De ICT-afdeling, bestaande uit Arieh Tal, Tarik Gammoun, Willem-Pieter Sukkel en Erik Smeets, is mijn dank verschuldigd voor het in de lucht houden van de 2 supercomputers zonder welke dit promotieonderzoek nergens zou zijn.

Een aantal collega's aan de High Tech Campus wil ik hartelijk bedanken voor bijdragen aan dit onderzoek, namelijk Siebe van Mensfoort en Rein de Vries. Bedankt voor het aanleveren van het drift-diffusie model. Ook Jürgen Rusch wil ik bedanken voor de spoedcursus visualiseren. Dankzij zijn hulp zijn de plaatjes van driedimensionale stroomdichtheidsdistributies, welke onder andere op de voorkant van dit proefschrift te zien zijn, gemaakt.

Ik wil mijn vriendengroep in Utrecht bedanken. Sinds het afronden van mijn studie was ik steeds minder en minder in Utrecht te vinden. Desondanks kijk ik graag terug op de vele bioscoopbezoeken en pool- en bowlingavonden.

Als laatste maar zeker niet de minste wil ik mijn ouders, mijn zus en mijn twee broers bedanken die ondanks dat ze niet altijd wisten waar mijn onderzoek over ging wel altijd voor me klaar stonden.

List of Publications

Modeling and analysis of the three-dimensional current density in sandwich-type single-carrier devices of disordered organic semiconductors

J.J.M. van der Holst, M.A. Uijtewaal, B. Ramachandhran, R. Coehoorn, P.A. Bobbert, G.A. de Wijs, R.A. de Groot
Phys. Rev. B **79**, 085203 (2009)

Electron-hole recombination in disordered organic semiconductors: Validity of the Langevin formula

J.J.M. van der Holst, F.W.A. van Oost, R. Coehoorn, P.A. Bobbert
Phys. Rev. B **80**, 235202 (2009)

Monte-Carlo study of charge transport in organic sandwich-type single-carrier devices: effects of Coulomb interactions

J.J.M. van der Holst, F.W.A. van Oost, R. Coehoorn, P.A. Bobbert
Submitted (2010)

Modeling of the transient mobility in disordered organic semiconductors

W. Chr. Germs, J.J.M. van der Holst, S.L.M. van Mensfoort, P.A. Bobbert, R. Coehoorn
In preparation (2010)

Curriculum Vitae

Jeroen van der Holst was born on January 3rd of 1983 in Hoorn. After finishing gymnasium at the Marnix College in Ede, he started the parallel studies Physics and Mathematics at the University of Utrecht. He conducted his master thesis at the Institute for Theoretical Physics under the supervision of prof.dr. R. Loll. His research subject concerned the calculation of the spectral properties of simplicial discretizations of space-time. He graduated in Physics in 2006 and in Mathematics in 2007. In december 2006 he started his Ph.D. project at the Eindhoven University of Technology under the supervision of dr. P.A. Bobbert and prof.dr. R. Coehoorn in the group Theory of Polymers and Soft Matter of prof.dr. M.A.J. Michels. The most important results of this research project are described in this thesis.

Jeroen van der Holst is geboren op 3 januari 1983 te Hoorn. Na het afronden van een gymnasium opleiding aan het Marnix College te Ede, begon hij in 2001 aan de twee studies Natuurkunde en Wiskunde aan de Universiteit van Utrecht. Zijn afstudeeronderzoek heeft hij uitgevoerd aan de Instituut voor de Theoretische fysica onder begeleiding van prof.dr. R. Loll. Het afstudeeronderwerp betref de bepaling van de spectrale eigenschappen van simpliciale discretizaties van ruimte-tijd. In 2006 studeerde hij af in Natuurkunde, in 2007 in Wiskunde. In december 2006 begon hij met zijn promotie-onderzoek aan de Technische Universiteit van Eindhoven onder leiding van dr. P.A. Bobbert en prof.dr. R. Coehoorn in de groep Theorie van Polymeren en Zachte Materie van prof.dr. M.A.J. Michels. De belangrijkste resultaten van dit onderzoek staan beschreven in dit proefschrift.

